AD-A267 446

93-17246

RADOME DEPOLARIZATION EFFECTS ON
MONOPULSE RECEIVER TRACKING PERFORMANCE

DISSERTATION

Michael A. Temple, Captain, USAF

AFIT/DS/ENG/93 03

DEPARTMENT OF THE AIR FORCE

AIR UNIVERSITY

AIR FORCE INSTITUTE OF TECHNOLOGY

Wright-Patterson Air Force Base, Ohio

93 7 30 028

AFIT/DS/ENG/93-03

DTIC
ELECTE
AUG 0 4 1993
Ŝ

RADOME DEPOLARIZATION EFFECTS ON
MONOPULSE RECEIVER TRACKING PERFORMANCE

DISSERTATION

Michael A. Temple, Captain, USAF

AFIT/DS/ENG/93-03

Accesion For		
NTIS CRA&I		√
DTIC TAB		☐
Unannounced		☐
Justification		
By		
Distribution /		
Availability Codes		
Dist	Avail and / or Special	
A-1		

DTIC QUALITY INSPECTED 3

AFIT/DS/ENG/93-03

RADOME DEPOLARIZATION EFFECTS ON
MONOPULSE RECEIVER TRACKING PERFORMANCE

DISSERTATION

Presented to the Faculty of the School of Engineering

of the Air Force Institute of Technology

Air University

In Partial Fulfillment of the

Requirements for the Degree of

Doctor of Philosophy

Michael A. Temple, B.S.E., M.S.E.

Captain, USAF

June 1993

AFIT/DS/ENG/93-03

RADOME DEPOLARIZATION EFFECTS ON

MONOPULSE RECEIVER TRACKING PERFORMANCE

Michael A. Temple, B.S.E., M.S.E.
Captain, USAF

Approved:

Uttal P. Pyati   _18 June 1993_

John Paul Shin   _18 Ju 1993_

Mark E. Oxley   _18 Ju 1993_

Byron M Welsh   _18 Jun 1993_

Accepted:

Dean, School of Engineering

Acknowledgements

I received a great deal of help from many people throughout the course of my research and during the writing of this dissertation. I am especially grateful to my research committee chairman Dr. Vittal Pyati who graciously accepted the task of guiding me through the research. I also wish to express my gratitude to Capt Paul Skinner and Dr. Mark Oxley, the other two members of my research committee. The collective efforts of my committee were consistently insightful and helpful, providing me the necessary corporate knowledge and experience to successfully complete the research. I also wish to thank the ECM Advanced Development Branch of Wright Laboratory (WL/AAWD), the technology sponsor for the research, and Mr. Jeff Hughes, the technical point of contact, for providing the administrative and technical support I needed to complete the final analysis and validation phase. Finally, I am most grateful to my loving wife Lois and my children, Charity, Stephen, and Sarah, for the unselfish sacrifices they made which allowed me to complete the research program.

<div align="right">Michael A. Temple</div>

Table of Contents

List of Figures

Abstract

Boresight Error (BSE), defined as the angular deviation between the true position and the apparent position of a target as indicated by a radar, is a very important figure of merit for a tracking radar. Ideally, zero BSE is desired but seldom achieved. Hence, a capability to accurately predict BSE in the design phase of a new radar system or to impact modifications of an existing system becomes imperative. Prior work on the subject matter is somewhat sketchy and limited in scope. Therefore, this dissertation undertakes a thorough and comprehensive investigation of BSE using a systems concept so that the final product is applicable to a variety of situations. A monopulse tracker was chosen for this study because it possesses superior angle tracking capability and it is used in a majority of modern radar systems.

Although there are many factors intrinsic and extrinsic to a radar system that give rise to BSE, the most significant contributor is the protective radome. An incoming plane wave suffers depolarization and phase front distortion as it travels through the radome. The net result of these undesirable changes is BSE, resulting in tracking error and inaccurate target location estimates. Surface integration and Geometric Optics (GO) are two methods commonly used to investigate the effects of a radome on BSE. Building on the "consensus" that the ray-trace receive GO propagation technique offers the "best" compromise between accuracy and computational intensity, this research effort employed a GO technique which greatly expanded previous ray-trace receive techniques to include: 1) a uniquely defined/developed

mathematical description for each surface within arbitrary multi-layer tapered radomes, surface descriptions are generated using a tangent ogive reference surface, 2) an "ideal" taper function concept for obtaining optimum BSE prediction performance, 3) a generalized technique for calculating specular reflection points within the radome, and 4) the total refractive effects along ray propagation paths. Fortran computer model results were compared with limiting case data (BSE = 0°), published experimental data, and production system acceptance test data. Limiting case validation was accomplished using 1) single and multi-layer tapered "air" radomes by setting the relative permittivity and permeability of each layer equal to one, 2) hemispheric radomes with the aperture gimbal point located at the sphere center, and 3) radome boresight axis scanning (through the tip). For these cases, "system" modeling error was less than .06 mRad for all scan angles and polarizations of interest. "Excellent" (BSE within ±1 mRad) results were obtained using a hemispheric half-wave wall radome with a displaced aperture gimbal point; predicted BSE values were within ±1 mRad of published surface integration and measured experimental data. Likewise, modeled BSE predictions for the production system were within ±0.5 mRad of measured data over a 30° scan range. Validated model results were then used to determine overall ray refractive effects on BSE prediction and found to provide only marginal benefit at the expense of computational efficiency. In conclusion, all the initial goals and aims of this research were not only met but exceeded in this dissertation.

RADOME DEPOLARIZATION EFFECTS ON
MONOPULSE RECEIVER TRACKING PERFORMANCE

I. Introduction

The ability to accurately locate and track hostile targets either actively or passively is a key feature in the survival and mission effectiveness of a vast majority of airborne military platforms. Monopulse processing techniques are particularly well suited for angle tracking Extensive research and development efforts over the past several decades has led to the proliferation of monopulse radar tracking systems on both fixed and airborne platforms [1]. Requirements and techniques for integration of a complete monopulse radar system, i.e., aperture, receiver, and processor, onto an airborne platform is not unlike conventional radar systems except for space limitations. Environmental protection of the radar system is essential and is typically in the form of a protective cover called a radome. The radome is generally composed of low-loss dielectric materials and streamlined so as not to interfere with the aerodynamic performance. Although designed to be "transparent" to the operating range of frequencies. an incoming plane wave while passing through the radome is subject to amplitude attenuation, phase from distortion, depolarization, etc. Hence, the monopulse radar system generally processes a distorted electromagnetic (EM) wavefront, which results in tracking errors and degraded performance.

1

1.1 Motivation

This dissertation provides a detailed analysis of such degrading effects on the accuracy and tracking performance of a monopulse radar system. This research effort is also aimed at predicting monopulse tracking performance degradations in the event a particular "system" component has to be modified to meet changing requirements. In this context the term "system" applies to an integrated system consisting of radome, aperture, and monopulse receiver/processor components. Although numerous analyses have been performed on individual system components in the past, modeling capabilities and analysis of the overall system is limited and are typically component specific and seldom flexible enough to accommodate any future modifications. This research effort combines previously developed modeling techniques and analysis procedures to model and analyze the entire "front-to-back" performance of the integrated "system", i.e., incident EM field to boresight tracking error curve. For given changes to key component parameters the synergistic effect of the overall system can be predicted. Results will provide a robust analysis procedure and valuable modeling tool by which system modification effects can be predicted and analyzed.

1.2 Problem Statement

The problem addressed under the research effort involves accurate characterization of radome depolarization and phase front distortion effects on monopulse receiver tracking performance. Degraded tracking performance is best characterized through analysis of system boresight error (BSE) under varying

2

conditions presented by "system" components. Angular "system" BSE is defined as the difference between the angle indicated by the monopulse tracking system (angle for which the monopulse system generates NO tracking/pointing correction signal) and the true target/source location. Source/target location data is typically provided to aircraft/missile guidance and control systems for use in establishing platform responses. Any "system" BSE results in an inappropriate platform response, i.e., incorrect guidance/control decision, potentially limiting mission effectiveness or causing total system failure. "System" BSE must be accurately predicted and minimized to ensure cost effective and reliable systems are developed. Previous research efforts have successfully used BSE prediction as a metric for establishing/validating monopulse tracking performance [2, 3, 4, 5, 6]. Predicted BSE estimates within ± 1 mRAD of measured values are generally regarded as "excellent" [5] and are typically obtained by propagation models using computationally intense surface integration techniques [2, 4]. Ray-tracing propagation techniques were considered as a means to reduce computational intensity. Comparative studies of available propagation techniques, i.e., ray-trace receive, ray-trace transmit, plane-wave spectrum, and surface integration, established a "consensus" that the ray-trace receive (also called fast receiving and backward ray-trace) propagation technique offers the best compromise between accuracy and computational intensity for moderate to large-sized radar/radome systems [3, 5, 6]. Efforts using the ray-trace receive propagation technique have successfully characterized BSE "response" to varying "system" parameters, i.e., radome layer thickness and electrical properties, E-Field frequency and polarization, operating temperature, aperture illumination,

3

etc. [4, 6]. However, these efforts experience limited success in predicting actual BSE values which compare favorably with measured data.

1.3 Approach

The ray-trace receive propagation technique is used for analysis and modeling to achieve the goal of comput   ional efficiency. A survey of previous research efforts which used this propagation technique revealed/identified several areas requiring "improvement" for obtaining accurate analysis and modeling results. The effects of ray refraction (deflection/spreading) upon propagating through the radome were not accounted for in previous efforts. Therefore, refractive effects on BSE prediction had not been established and needed to be accurately accounted for in the current analysis and modeling development [3, 6].

The "simple" radome structure models of previous efforts generally provide limited modeling capability, accurately modeling single layer constant thickness radomes but providing minimal flexibility for multi-layer tapered radome designs These "simple" modeling techniques are unacceptable for BSE refractive effect characterization, requiring improvement for detailed analysis and modeling purposes. To accurately account for refractive effects in arbitrarily shaped single and multi-layer radome designs (consisting of both constant and tapered dielectric layers), closed-form radome surface equations are used in conjunction with Snell's Law of Refraction to establish ray propagation paths through the radome. Multi-layer radome surface equations are developed using a tangent ogive reference surface, allowing virtually all circularly symmetric radome shapes to be accurately analyzed and modeled.

4

Reflected E-Fields within the radome can account for a significant portion of the error between predicted and measured BSE values [5, 6]. Incident E-Field reflection points are typically calculated via some form of "hit-or-miss" technique. Given an established reference plane which is perpendicular to the direction of propagation, rays are traced from uniformly spaced grid points (typically spaced at one-quarter or one-half wavelength intervals) through the radome to inner surface reflection points. Rays are reflected and checked to see "if" they intersect the aperture plane [4]. Rays which intersect the aperture are included in reflected E-Field calculations at the nearest aperture sample point/element location, non-intersecting rays are excluded. The current analysis and modeling technique improves on this "hit-or-miss" technique by calculating ray reflection points. Fermat's principle and variational calculus techniques are applied to multi-layer surface equations resulting in a system of equations which provide reflection point solutions.

1.4 Research Contributions

The following list is a summary of research contributions achieved in addressing the problem of accurately predicting "system" BSE. The contributions are a result of applying the approach stated in *Section 1.4* and provide "improved" BSE prediction capability. Research contributions include:

(1) A uniquely defined analysis and modeling procedure for "systems" including a multi-layer tapered radome, providing closed-form equations for each radome surface relative to a tangent ogive reference surface.

5

(2) Established "Ideal" taper function criteria for use with (1), resulting in a procedure which produces a "near" optimum taper function for BSE prediction.

(3) A generalized analysis procedure and solution technique for calculating radome reflection points on an arbitrarily shaped reflecting surface. The generalized solution is reduced to a system of two non-linear transcendental equations with two unknowns for the case of a tangent ogive reflecting surface.

(4) Propagated E-Field expressions and analysis results using Geometric Optics and surface equations of (1) accounting for total refractive effects along ray propagation paths.

(5) A validated "system" model based on (1) thru (4) which predicts BSE performance using "front-to-back" propagation characteristics. Validation is based on empirical, published experimental, and production "system" acceptance test data.

(6) Refractive effect characterization in principle and diagonal scan planes using the validated model of (5).

II. Background

2.1 Introduction

This chapter outlines and highlights background information existing on the overall analysis and modeling effort for radomes, antennas, and monopulse techniques. Each section presents an overview of the key component parameters relevant to this research. Additionally, applicable assumptions are identified and justified.

2.2 Radomes

A radome is a protective covering which is generally composed of low-loss dielectrics and designed to be transparent to Electromagnetic (EM) waves of interest. The actual shape of the radome is application specific and despite best efforts to the contrary, affects both the aerodynamics of the aircraft and electrical performance of the radar. Generally, highly streamlined shapes have less drag and can better withstand precipitation damage; however, electrical performance usually deteriorates [7]. Generally, the more streamlined a radome shape becomes the greater the incidence angle a propagating EM wave experiences. Higher EM wave incidence angles typically increase reflections on the radome's surface, resulting in less energy being transmitted through the radome wall. Additionally, wavefront "depolarization" occurs as the EM energy propagates through the radome wall.

Depolarization occurs when an EM wave propagates through boundaries exhibiting discontinuous electrical and magnetic properties namely, permittivity ϵ, permeability μ, and conductivity σ. The effects of the discontinuities on the

7

propagating wave can be expressed in terms of a transmission coefficient T and a reflection coefficient Γ, both of which are generally complex quantities. For uniform plane wave illumination (a wave possessing both equiphase and equiamplitude planar surfaces), at an oblique incidence angle on the interface of layered media, both T and Γ are functions of : 1) the constitutive parameters on either side of a boundary, 2) the direction of wave travel (incidence angle), and 3) the orientation of the electric and magnetic field components (wave polarization) [8, 9].

Standard techniques for analyzing plane wave propagation across electrically discontinuous boundaries generally begin by establishing a plane of incidence. The plane of incidence is commonly defined as the plane containing both a unit vector normal to the reflecting interface (boundary) and a vector in the direction of incidence (propagation). To analyze the reflection and transmission properties of a boundary for waves incident at oblique angles with arbitrary polarization, for convenience, the electric or magnetic fields are decomposed into components parallel and perpendicular to the plane of incidence . When the electric field is parallel to the plane of incidence it is commonly referred to as the *Transverse Magnetic* (TM) case. Likewise, when the electric field is perpendicular to the plane of incidence it is commonly referred to as the *Transverse Electric* (TE) case [8].

An EM wave is propagated across the boundary by applying the appropriate parallel or perpendicular transmission/reflection coefficient, i.e., $T_{\parallel}$, $T_{\perp}$, $\Gamma_{\parallel}$, or $\Gamma_{\perp}$, to the corresponding component of the electric or magnetic field. Eqs (1) thru (3) illustrate this process where the superscript i represents the *incident* field components,

8

the superscript r represents the *reflected* field components, and the superscript t represents *transmitted* field components. From Eq (2) it is apparent why an EM wave often experiences depolarization upon propagating through a homogeneous radome layer. Conditions which cause the parallel and perpendicular transmission coefficients to differ, either in amplitude or phase, can result in the total transmitted field exhibiting a polarization which differs from the incident field.

$$\vec{E}_\perp^r = \Gamma_\perp \vec{E}_\perp^i \quad ; \quad \vec{E}_\parallel^r = \Gamma_\parallel \vec{E}_\parallel^i \qquad (1)$$

$$\vec{E}_\perp^t = T_\perp \vec{E}_\perp^i \quad ; \quad \vec{E}_\parallel^t = T_\parallel \vec{E}_\parallel^i \qquad (2)$$

$$\vec{E}_{Total}^r = \vec{E}_\perp^r + \vec{E}_\parallel^r \quad ; \quad \vec{E}_{Total}^t = \vec{E}_\perp^t + \vec{E}_\parallel^t \qquad (3)$$

Figures 1 and 2 illustrate typical variations which occur in perpendicular and parallel transmission/reflection coefficients. Comparison of these figures shows how the magnitude of the coefficients varies as a function of constitutive parameters and incidence angle. Incidence angles which reduce the reflection coefficient to zero are referred to as Brewster angles [8]. The depolarization effect resulting from the parallel and perpendicular transmission coefficients having unequal magnitudes is graphically illustrated in Figure 3. Clearly, a wave "depolarization" between the incident and transmitted electric field has occurred.

9
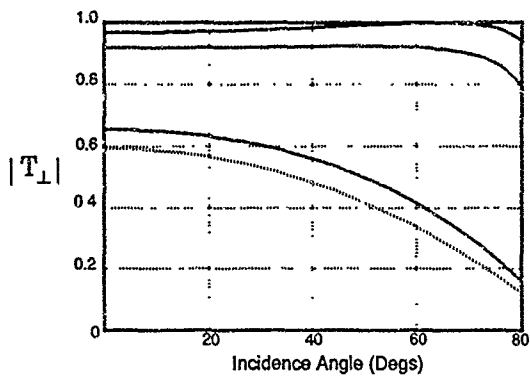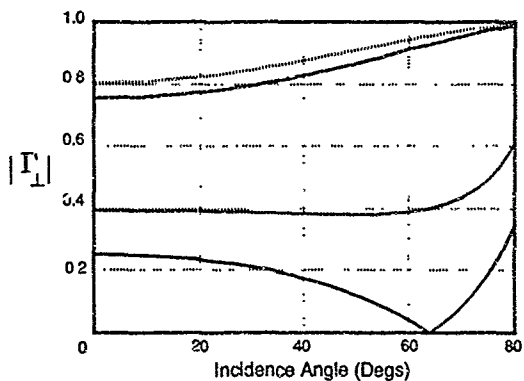
(a) Transmission

(b) Reflection

$\varepsilon_r = 4.8$ $\varepsilon_r = 7.8$

$\varepsilon_r = 5.3$ $\varepsilon_r = 9.3$

Figure 1. TE Transmission and Reflection Coefficients

(a) Transmission

(b) Reflection

$e_r = 4.8$ — — $e_r = 7.8$

$e_r = 5.3$ $e_r = 9.3$

Figure 2. TM Transmission and Reflection Coefficients
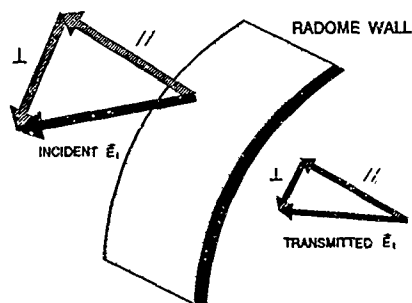
Figure 3. Graphical Representation of Radome Depolarization Effects

Magnitude and phase differences between parallel and perpendicular reflection coefficients will result in depolarization upon reflection. Any depolarization occurring along a direct or reflected propagation path generally introduces a polarization mismatch between the incident EM field and radar aperture, which reduces aperture efficiency and degrades the overall performance. Since the degree of radome depolarization depends upon the incidence angle and polarization of the incident wave, and the electrical properties of the radome itself, *radome transmission and reflection coefficients emerged as important parameters for analysis and modeling purposes in the present research effort.*

Previous efforts have effectively utilized reflection and transmission coefficients to characterize overall radome electrical performance [2, 4]. Equations have emerged and elaborate code has evolved for calculating transmission and reflection coefficients. This research effort capitalized on past efforts by using equations

12

derived by Richmond for calculating the coefficients [10]. Modifications were made to the Richmond derivation to make the calculated output coefficients equivalent to the more elaborate Periodic Moment Method (PMM) code developed by the Ohio State University (OSU). The PMM code is capable of analyzing periodic structures imbedded in an arbitrary number of dielectric slabs of finite thickness [11]. Although compatibility with the more sophisticated code was not necessarily a firm requirement, it was addressed to 1) assure flexibility and wider use of the analysis and modeling technique, and 2) provide an alternate source for comparison and validation of particular components of the model. In both cases, Richmond's development and the OSU PMM code were developed for planar dielectric slabs of finite thickness and infinite extent in both height and width. Their use in approximating T and Γ for "locally planar" analysis and modeling cases has been very effective and widely accepted among the technical community. Generally, "locally planar" conditions exist at any given point on a specified surface where the radii of curvature of the surface at that point are large compared to a wavelength. As explained and justified in detail later, *this research effort concentrated on system component designs and test conditions by which locally planar approximations could be enforced.*

The primary reference surface considered in the research effort was the tangent ogive for several reasons. First, many practical radomes possess at least one surface (boundary between two adjacent layers) which is either truly a tangent ogive surface or some slight variation thereof. Second, a tangent ogive surface can be expressed by a closed-form analytic expression making it a useful reference surface for generating closed-form expressions for non-ogive surfaces. Third, the tangent ogive

13

radome shape has been analyzed extensively. As such, a wealth of empirical and measured data exists for comparison and validation purposes. Lastly, a majority of practical tangent ogive radomes have physical dimensions that are large compared to their design wavelength. Therefore, the radius of curvature at any point on the radome's surface through which the radar aperture must "look" is large in comparison to one wavelength. This condition makes locally planar techniques valid for analyzing overall system performance and at the same time satisfies the locally planar requirement for calculating transmission and reflection coefficients.

There are two widely used methods for analyzing radome transmission and reflection properties. The *surface integration* method calculates the field distribution due to the antenna on the inner radome surface at a number of discrete points and the far-field response as an integration over the outer surface of the radome, accounting for the transmissivity effects [12]. This method is the most accurate but is also much more time consuming to implement (computationally intense). The second method is *ray tracing* (geometrical optics) where transmitted rays are assumed to pass directly through the radome wall and reflected rays are assumed to originate at the point of incidence. The transmitted electric field at a given point is found by considering an incident ray which would pass through the point with the slab removed and then weighting the field of this ray with the appropriate insertion transmission coefficient [4]. Although the *ray tracing* method does not accurately predict sidelobe performance outside those nearest to the main beam, it accurately characterizes the properties of the main beam itself.

14

Figure 4 illustrates an application of the *ray tracing* method to an arbitrarily shaped radome enclosing a phased array antenna. Given a specific reference plane location, a ray normal to the reference plane is traced through the radome to a specified element location on the aperture. At the ray intersection point on the outer surface of the radome, a surface normal vector is calculated and the ray's angle of incidence determined. Invoking the locally planar approximations, transmission and reflections coefficients are calculated and used to weight appropriate field components of the incident EM wave.

MAIN BEAM RAYS
(TRANSMITTED)

RADOME
BORESIGHT AXIS

IMAGE LOBE RAYS
(REFLECTED)
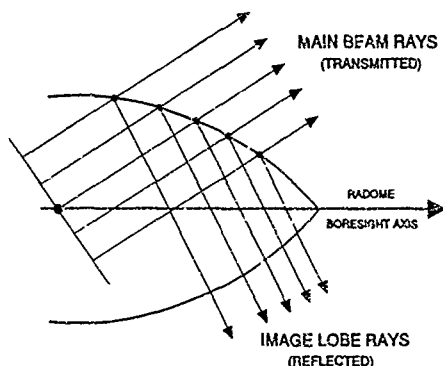
Figure 4. Ray Tracing: Main Beam and Image Lobe Rays

The *main beam* (direct) rays are determined directly by weighting the appropriate parallel and perpendicular field components of the incident wave. The *image lobe*

15

(reflected) rays identified in Figure 4 are quite different. A typical radome creates an image lobe(s) anytime significant reflections exist within the radome. As seen in the figure, an *image lobe* ray actually experiences the effects of both reflection and transmission as it propagates. For *ray tracing* analysis image lobe rays must be weighted by both a transmission and reflection coefficient.

2.3 Antennas

Many characteristics/parameters are used to describe the performance of an antenna, including: radiation pattern (field or power pattern), input impedance, polarization, gain, directivity, half-power beamwidth (HPBW), first-null beamwidth, side lobe level (SLL), etc. Although all these characteristics are considered important for various analysis purposes, not all were considered to be key to the success of this research effort. *Two of these characteristics were considered of primary importance in the overall system analysis for this research effort, namely, the radiation pattern and the polarization.*

The radiation pattern of an antenna is a graphical representation of its radiation properties as a function of spacial coordinates. A radiation pattern typically displays the variation in the "field strength" (field pattern) or the "power density" (power pattern) as a function of angle. Henceforth, any reference in this dissertation to antenna radiation pattern, or simply antenna pattern, is implicitly referring to the antenna "field pattern" and will be designated as $f(\theta, \phi)$. The two variables θ and ϕ allow for the field pattern to vary in two dimensions and $f(\theta, \phi)$ is considered to be the field pattern as observed in the antenna's far-field.

16

The primary antenna type considered was a planar phased array with corporate feed. A corporate feed structure is an equal path-length branching network. The electrical path length from the central terminal to all phase shifters is the same and the feed provides a broadside wavefront for the phase shifters to operate on [14]. This choice was believed reasonable considering that a vast majority of modern airborne platforms utilize this specific technology to meet their aperture needs. Additionally, a relatively "simple" method exists for obtaining monopulse operation from a phased array antenna. Details of this method and the radiation patterns required for accurate monopulse performance are provided in *Section 2.3, Monopulse Processing.*

A phased array aperture is an antenna whose main beam maximum direction or pattern shape is primarily controlled by the relative phase of the element excitation currents on the array [13]. The spacial orientation of the basic radiating elements which form the array structure is somewhat arbitrary, depending on the desired overall array performance. However, the basic planar phased array antenna typically consists of equally spaced elements on a rectangular grid. As with linear arrays, grating lobes are one of the major concerns during array design. Grating lobe, are additional maxima which appear in the field pattern with intensities nearly equal to the intensity of the main beam. The effects of radiative grating lobes are minimized/eliminated by ensuring the distance between any two adjacent elements within the array is less than one wavelength (λ). Generally, the spacing between any two adjacent array elements is maintained at one-half a wavelength $(\lambda/2)$.

In analyzing the field pattern of array antennas the principle of "pattern multiplication" is often used. As shown in Eq (4), pattern multiplication allows the

17

array field pattern $f(\theta,\phi)$ to be factored into the product of the element pattern, $f_e(\theta,\phi)$, and the array factor, $AF(\theta,\phi)$. The element pattern, $f_e(\theta,\phi)$, is the field pattern of a typical element within the array. The complex C_n term in Eq (4) represents mutual coupling effects for the nth array element. Although the value of C_n is dependent on element location, mutual coupling effects are generally assumed to be identical for all elements within the array. This is particularly true for densely populated arrays which use amplitude tapers for pattern control.

$$f(\theta,\phi) = f_e(\theta,\phi) AF(\theta,\phi) = f_e(\theta,\phi) \sum_{n=1}^{N} C_n I_n \, exp(j \beta \hat{r} \cdot \vec{r}_n') \qquad (4)$$

$$I_n = A_n e^{j\alpha_n} \qquad (5)$$

The array factor $AF(\theta,\phi)$ is the field pattern of the array when the elements are replaced by point sources (isotropic radiators) excited by the same current amplitudes and phases as the original elements [13]. The vector $\vec{r}_a'$ is a position vector from the coordinate origin to the element position and $\hat{r}$ is a unit spherical radius vector for the same coordinate system. The I_a term in Eq (4) represents the complex excitation current of the nth array element and may be expressed as given in Eq (5), where A_n and α_n are real quantities representing the amplitude and phase of the excitation current, respectively. Assuming the array of elements and feed network form a passive reciprocal structure, the phased array will exhibit identical field patterns for

both transmission and reception [14]. This assumption may not be valid if the feed network contains any non-linear or directive components such as ferrite phase shifters or amplifiers. *For the research effort a passive reciprocal array structure was assumed allowing for reciprocity to be invoked whenever necessary.*

The polarization of the antenna array is the second characteristic of importance to the research effort. Mutual coupling between array elements, seen earlier to cause the element field patterns to vary from element to element, can cause a depolarization effect, i.e., the phased array may exhibit a polarization unlike the polarization of the individual elements [13]. For maximum coupling of energy between an EM wave and an antenna to occur the polarization of the wave and the antenna must be matched.

In practice a true polarization match between an incident EM wave and receiving antenna is seldom achieved. Design and manufacturing limitations both contribute to degraded antenna performance, resulting in the antenna's polarization state being less than "pure". Also, the medium through which the EM wave must propagate to reach the antenna aperture will likely degrade the purity of the incident wave's polarization. This latter case was discussed in detail in *Section 2.1, Radomes,* where significant polarization variations were seen to occur as a result of radome design and materials. The electric field transmitted by the radome was seen to vary significantly as the angle of incidence of the incident electric field was varied.

To account for the effects of polarization mismatch between antennas and incident waves, the concept of a Polarization Loss Factor (PLF) is introduced. The term loss is used since a polarization mismatch results in a condition where the

19

amount of power extracted from an incoming wave by an antenna will not be maximum [13]. The PLF between an antenna and incident electric field may be defined as given by Eq (6) where $\hat{\rho}_w$ is a complex unit vector defining the polarization of the incident wave, $\hat{\rho}_a$ is a complex unit vector defining the polarization of the antenna, and Ψ_p is the angle between the two unit vectors [15].

$$PLF = |\hat{\rho}_w \cdot \hat{\rho}_a|^2 = |\cos\psi_p|^2 \qquad (6)$$

The PLF can vary between zero and one with a PLF = 1 representing an ideally polarized (perfect match) condition and a PLF = 0 representing an orthogonal (total mismatch) condition. These two extreme cases are referred to as "co-polarized" (PLF = 1) and "cross-polarized" (PLF = 0) conditions [13]. Neither of these two extremes are likely to occur in practice. However, the terms co-polarized and cross-polarized are generally used to describe an antenna's response, as done throughout this dissertation. A polarization reference direction is established to coincide with the polarization direction of the aperture elements. Fields are then resolved into components which are perpendicular (cross-polarized) and parallel (co-polarized) to this reference direction.

This convention was used in *Section 2.1* where the reference polarization direction was established as the antenna's polarization direction. An electric field radiated by the antenna was then propagated through the radome resulting in a transmitted electric field polarization vector which had "rotated". Applying reciprocity, the overall antenna/radome system would now respond to EM waves with polarization states

different from the aperture. The depolarization effect of the radome alters the response of the original system, a system designed by assuming ideal transmission and reflection properties for the radome.

2.4 Monopulse Processing

To actually define/describe what constitutes a monopulse receiver/processor system is difficult and varies from author to author. However, the concept that "monopulse" implies determining the relative bearing of a radiation source by analyzing the received characteristics of a "single pulse" of energy from that source is consistently seen throughout literature. This "single pulse" tracking/locating is typically accomplished by one of three basic monopulse techniques. These three techniques are characterized by the manner in which angle information is extracted from the received signal and include amplitude-comparison, phase-comparison, and amplitude-phase-comparison (a combination of the two previous techniques) [16]. System processing requirements for implementing each technique can vary significantly as will be seen throughout the course of this discussion.

Amplitude Comparison Monopulse (ACMP) processing is perhaps the simplest form of "single pulse" processing. A basic ACMP system typically consists of an antenna system, receiver/processor, and a display. and is generally used as a baseline reference for analysis and discussion purposes. In the baseline system, the antenna system employed typically consists of a pair of radiating elements having identical field patterns, say $f(\theta)$. These radiating elements are physically located in such a manner that their field pattern maximums occur at angles of $\pm \theta_{sq}$ with respect to the

21

antenna system's boresight axis ($\theta = 0°$), θ_{sq} is referred to as the "squint" angle. This same field pattern relation may also be achieved by a phased array antenna via electronic beam steering techniques. Henceforth, these two field patterns will be referred to as $f_1(\theta)$ for the $\theta - \theta_{sq}$ pattern and $f_2(\theta)$ for the $\theta + \theta_{sq}$ pattern. The voltages corresponding to each antenna output will be referred to as v_1 and v_2 for the $f_1(\theta)$ and $f_2(\theta)$ field patterns, respectively. These voltages may be expressed as:

$$v_1 = A_1 e^{j\beta_1} f(\theta - \theta_{sq}) = A_1 e^{j\beta_1} f_1(\theta) \tag{7}$$

$$v_2 = A_2 e^{j\beta_2} f(\theta + \theta_{sq}) = A_2 e^{j\beta_2} f_2(\theta) \tag{8}$$

where A_1, β_1, and A_2, β_2, are proportional to the amplitude and phases associated with an impinging EM wavefront on antenna #1 and antenna #2, respectively. These equations indicate that the antenna voltages developed are in general complex quantities. At this point no consideration has been given to the EM wave polarization match/mismatch conditions. Rather, it has been assumed here that the polarization of the impinging wave identically matches the polarization of the antennas being used, a condition not existent in a practical situation. This matched polarization assumption is carried throughout the remainder of the monopulse discussion. Polarization effects identified earlier in *Section 2.2* as both cross-polarized and co-polarized antenna field pattern effects will be incorporated into the equations later since the study and analysis of these effects was the primary concern of the research effort.

A basic ACMP system typically accomplishes angle tracking by forming a ratio consisting of the "difference" (del or Δ) between the antenna voltages to the "sum" (Σ) of the antenna voltages. Since phased array antenna systems can independently form any desired set of radiation patterns, within practical limits, the "sum" and "difference" patterns are usually formed directly rather than by addition and subtraction of outputs of the individual field patterns $f_1(\theta)$ and $f_2(\theta)$ [1]. As such, outputs of the individual beams may not be available for analysis anywhere in the system. The ACMP ratio formed is as expressed in Eq (9).

$$\frac{\Delta}{\Sigma} = \frac{del}{sum} = \frac{v_1 - v_2}{v_1 + v_2} = \frac{1 - \dfrac{v_2}{v_1}}{1 + \dfrac{v_2}{v_1}} \tag{9}$$

Antenna voltages v_1 and v_2 are generally complex quantities resulting in the monopulse processing ratio of Eq (9) also being complex. However, a couple of simplifying assumptions are often made for analyzing the basic ACMP system. These assumptions include the antennas having collocated phase centers and the source of radiation being located in the far-field (plane wave incidence) These assumptions result in a condition where β_1 equals β_2 causing the monopulse processing ratio to be purely real (in this case the relative phase difference between the sum and difference is zero degrees).

Because of its role in indicating error, i.e., a source located left/right of boresight results in a ratio with relationships indicating both magnitude (how far off boresight)

23

and phase (which direction off boresight), the ratio signal is often referred to as the "error signal", as will be done throughout the remainder of the dissertation. A steep slope on the error signal curve represents a high degree of sensitivity to changes in source location whereas a shallow slope represents a low degree of sensitivity. The error signal generated by the ACMP receiver/processor is generally used for either indicating the location of a radiating source via some form of visual display or to correct the pointing direction of the boresight axis. *The actual use of the error signal was not the focus of the research effort; the error signal itself is analyzed under varying conditions presented by the antenna and radome components.*

Phase Comparison Monopulse (PCMP) is similar to ACMP in that both require the same basic components (antenna system, receiver/processor, display). However, the design and functions of these components, especially the antenna and receiver/processor, may vary significantly. The basic PCMP system utilizes a pair of antenna elements with identical field patterns $f(\theta)$, similar to the ACMP system. A major difference in the two monopulse systems is that the antenna elements in the PCMP system are not squinted but physically displaced by distance d. This separation effectively separates the antenna phase centers. The antenna phase center is a point, located on the antenna or in space, whereby fields radiated by the antenna and referenced to this point are spherical waves with ideal spherical wavefronts or equiphase surfaces [15]. Under far-field conditions parallel ray approximations are used to estimate antenna output voltages. The expressions given by Eqs (10) and (11) represent typical source to observer approximations where R is the distance from the antenna coordinate axis and r_1/r_2 are the distances from the antenna

24

element: to the source. These approximations for the amplitude and phase remain valid provided the condition that $d << R$ is maintained.

$$AMP: \quad r_1 \approx R \approx r_2 \tag{10}$$

$$PHASE: \quad r_1 \approx R + \left(\frac{d}{2}\right)\sin\theta \quad ; \quad r_2 \approx R - \left(\frac{d}{2}\right)\sin\theta \tag{11}$$

Given these approximations and considering only single source illumination, the voltages present at each of the antennas' terminals may be expressed as given by Eq (12) and (13) where A and β represent the amplitude and phase of the source, respectively. The approximate forms of v_1 and v_2 in Eqs (12) and (13) clearly show that while the magnitudes of v_1 and v_2 vary with source location, they are equivalent for all values of θ. Therefore, no angle discriminating information is contained in the voltage magnitudes. However, the equations do indicate a difference between the phase terms in the approximate voltage forms of v_1 and v_2. Each phase term is seen to vary with the antenna separation distance d, the wave number $K = 2\pi/\lambda$, and the source location θ. Because angle discriminating information is contained only in the phase difference between the two antenna voltages, the term phase-comparison is applied. Using Eqs (12) and (13) the phase difference $\Delta\phi$ between voltages v_1 and v_2 may be expressed as given by Eq (14).

$$v_1 = f_1(\theta_1)\frac{A\,e^{-j(Kr_1 + \beta)}}{r_1} \approx f(\theta)A\,e^{-j(K(d/2)\sin\theta + \beta)}\frac{e^{-jKR}}{R} \tag{12}$$

25

$$v_2 = f_2(\theta_2) \frac{A\, e^{-j(Kr_2 + \phi)}}{r_2} \approx f(\theta)\, A\, e^{+j\{K(d/2)\sin\theta - \phi\}} \frac{e^{-jKR}}{R} \qquad (13)$$

$$\Delta\phi = \phi_1 - \phi_2 = Kd\sin\theta = \frac{2\pi d}{\lambda}\sin\theta \qquad (14)$$

The $\Delta\phi$ expression of Eq (14) characteristically represents an interferometric variation of $\Delta\phi$ as θ is varied and exhibit favorable characteristics for processing source tracking/locating data, specifically, a linear response with a positive slope passing through zero at $\theta = 0°$ the source location. This condition is consistent with results shown previously for the ACMP processing system with one major exception. The PCMP system exhibits several positive slope lines passing through zero in the presence of single source illumination (usually referred to as ambiguities). Since the location of these ambiguities is dependent on the antenna separation distance d and wavelength λ of the arriving signal, care must be taken in the PCMP processing to ensure erroneous angle data is not used. Similar processing techniques are often used for both the ACMP and PCMP type systems. In reality even practical ACMP systems exhibit these interferometric effects. It is practically impossible to perfectly align/generate squinted beam patterns with coincident phase centers, a fact neglected in the previous discussion of the ACMP system.

As mentioned in *Section 2.2, Antennas*, the primary antenna configuration considered for analysis and modeling throughout the research is the phased array

aperture with a corporate feed. This choice was deemed reasonable considering that a vast majority of modern airborne platforms use phased array technology to meet their aperture requirements. *The research effort concentrated on a "simple" method for obtaining monopulse operation.* Figure 5 depicts how an array antenna can be divided into symmetrical quadrants/sections. The outputs of all elements within each quadrant/section are summed to produce sum signals/beams, one per quadrant/section, which are then in turn combined to form appropriate antenna system sum and difference voltages [1].
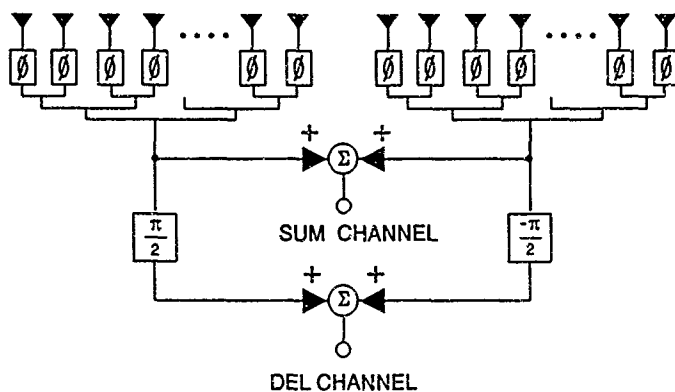
Figure 5. Phased Array Monopulse Processing

The component blocks identified by the large φ label in Figure 5 represent the complex weightings which drive the individual array elements. The "corporate" feed structure feeding the weights is designed such that the path length from the central

27

terminal (one per section) to the weighting functions is the same and thus the feed provides a broadside wavefront for the weighting functions to operate on [14]. Complex weighting functions allow for both amplitude and phase variations to be applied across the array aperture, i.e., from element to element. By providing amplitude variation across the aperture it is possible to obtain optimum radiation patterns. *For the research effort, uniform, cosine (radial), and Taylor amplitude distributions were considered.* Uniform and cosine amplitude tapers were considered primarily for comparison with existing measured data and the Taylor amplitude taper considered since it generally provides the highest antenna gain for a given sidelobe level. It has also been shown that for monopulse processing systems the Taylor weighting provides the greatest monopulse sensitivity slope factor and efficiency for a given sidelobe ratio [17]. Phase control is typically used in a phased array to perform beam steering. However, electronic beam steering via element phase control may introduce some asymmetrical antenna properties. *For completeness and overall analysis and modeling robustness, electronic scanning of the phased array aperture was considered within the scope of the research effort.* Throughout the analysis and modeling validation phase, comparisons between mechanically scanned and electronically scanned results are made when appropriate.

III. Multi-Layer Radome

3.1 Introduction

This section provides the motivation and development of the multi-layer radome equations used in the analysis and modeling of the overall radome, antenna, and monopulse receiver system. The approach taken in regard to the multi-layer radome orientation and structure was driven by several factors. First, a method was required to analyze and model tapered radomes since such structures minimize internal reflections and variation of insertion phase delay as a function of antenna look angle. Second, because Geometric Optics (GO) is employed, a surface normal vector is required for a given point within the radome. The task of determining a surface normal vector is simplified if the surface is mathematically describable by a function which is differentiable with respect to all variables of the specified coordinate system. In this case, the gradient of the function provides the surface normal vector. Lastly, the proliferation of "*tangent ogive*" shaped radomes in missile and aircraft applications make this a realistic shape for analysis and modeling purposes. The quotation marks are added to emphasize that a radome may exhibit a shape whose overall appearance is consistent with a tangent ogive's appearance without actually containing any "true" tangent ogive surfaces. A tangent ogive surface is considered since it will be used as a "*reference*" surface for the remainder of the development. The analysis proceeds by considering a single layer radome consisting of a tangent ogive reference surface separated from a second surface by a specified amount. Expressions derived for the single layer radome are then extended to the multi-layer radome.

29
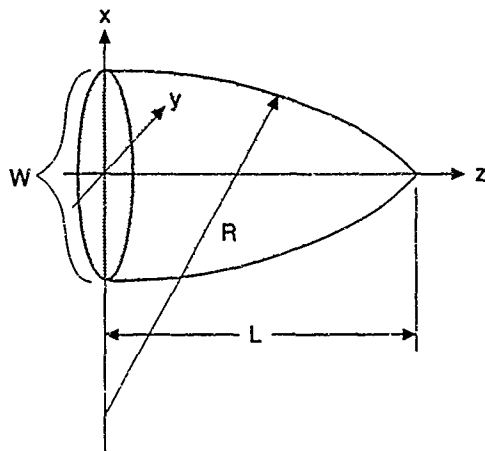
Figure 6   Tangent Ogive Surface

The tangent ogive radome is perhaps the most commonly used and modeled radome shape. It can be thought of as a compromise between the desirable aerodynamic performance of a cone and the desirable electrical performance of a hemisphere [6]. The tangent ogive, illustrated in Figure 6, is a surface of revolution generated by rotating a circular arc about a cord (every plane tangent to its base is perpendicular to the base plane). The surface of a tangent ogive is completely described by its generating radius R and base diameter W. For a tangent ogive which has its base plane in the x-y plane such that its tip lies on the z-axis, as illustrated in Figure 6 for a right-hand coordinate system, any point which lies on the ogive surface satisfies Eq (15) where $0 \leq z \leq L$. The ogive length L along the z-axis is given

30

by Eq (16). The "*fineness ratio*" of a radome is defined as the ratio L/W. For typical radomes the fineness ratio is greater than one and Eq (16) can be used to show that R > W.

$$g(x,y,z) = \sqrt{R^2 - z^2} - \sqrt{x^2 + y^2} + W/2 - R = 0 \qquad (15)$$

$$L = \sqrt{R^2 - (R - W/2)^2} \qquad (16)$$

In its rectangular form, the right-hand side of Eq (15) can be seen to represent the radii of curvature for a family of circles which lie in planes parallel to the x-y plane and which vary in length along the z-axis. Therefore, to generate a second surface located on either the inside or outside of the reference tangent ogive surface an additional radius factor can be subtracted or added to the right-hand side of the equation, subtraction generates an inner surface whereas addition generates an outer surface. It is this additional radius factor which will be established in the development of the single layer radome equations.

3.2 Single Layer Development

For a single layer radome the geometry of Figure 7 is used for developing the surface equations. It is assumed that the desired taper function $t(\theta)$ for the radome layer is known, i.e., $t(\theta)$ can be specified based on the desired radome electrical performance as a function of antenna look angle θ. The *reference* ogive surface is

31

specified by the parameters R_r and W_r with $R_r > W_r$ yielding fineness ratios greater than one and satisfying the spherical coordinate form of the tangent ogive equation as given by Eq (17). Since the surface is symmetric in ϕ the analysis is simplified by considering the $\phi = 0°$ plane (x-z plane) for equation development, the results of which are readily extendable for any arbitrary ϕ-plane.
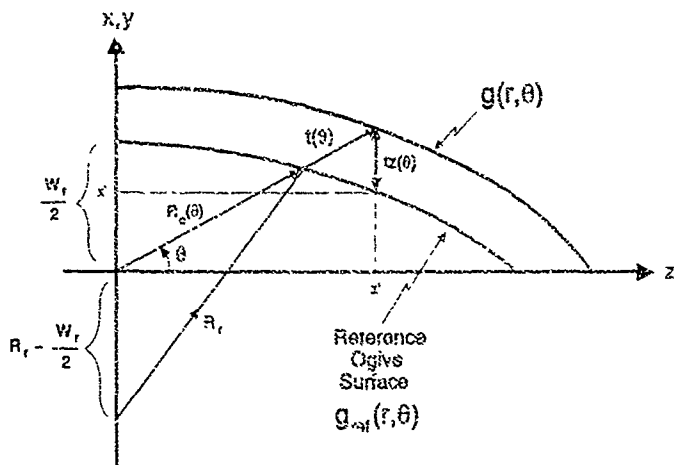
Figure 7. Single Layer Radome Geometry

$$g_{ref}(r,\theta) = \sqrt{R_r^2 - r^2\cos^2(\theta)} - r\sin(\theta) + W_r/2 - R_r = 0$$

$$\text{for } W_r/2 \leq r \leq L_r, \text{ and } 0 \leq \theta \leq \frac{\pi}{2}$$

(17)

32

As shown in Figure 7 tz(θ) represents the radius parameter required to be added/subtracted from the reference surface in order to generate the outer/inner surface, respectively. The goal is to determine the function tz(θ) required to modify $g_{ref}(r,\theta)$ such that the desired second surface is generated. For a specified value of θ the law of cosines may be applied to the geometry of Figure 7 to solve for $R_o(\theta)$. By computing the roots of a quadratic equation while enforcing the conditions $R_r > W_r$, and $0 \le \theta \le \pi/2$, $R_o(\theta)$ can be derived as summarized in Eqs (18) thru (22).

$$Applying \quad Law \quad of \quad Cosines$$

(18)

$$R_r^2 = R_o^2(\theta) + K_r^2 - 2 K_r R_o(\theta) \cos(\pi/2 + \theta)$$

$$R_o^2(\theta) + \left\{2 K_r \sin(\theta)\right\} R_o(\theta) + \left\{K_r^2 - R_r^2\right\} = 0$$

(19)

$$where: \quad K_r = R_r - W_r/2$$

$$Applying \quad Quadratic \quad Equation$$

$$Subject \ to: \ R_r > W_r \ and \ 0 \le \theta \le \pi/2 \rightarrow R_o(\theta) > 0 \rightarrow Take + Sign$$

(20)

$$R_o(\theta) = \frac{-2 K_r \sin(\theta) \pm \sqrt{4 K_r^2 \sin^2(\theta) - 4(K_r^2 - R_r^2)}}{2}$$

$$R_o(\theta) = -K_r \sin(\theta) \pm \sqrt{R_r^2 + K_r^2[\sin^2(\theta) - 1]}$$

(21)

$$R_o(\theta) = \sqrt{R_r^2 - K_r^2 \cos^2(\theta)} - K_r \sin(\theta) \qquad (22)$$

With $R_o(\theta)$ determined the process of determining $tz(\theta)$ continues by calculating the coordinates identified as $x'(\theta)$ and $z'(\theta)$ in Figure 7. Once calculated per Eq (23), these coordinates are substituted into the expression given by Eq (24) to obtain the final form expression for $tz(\theta)$. The final $tz(\theta)$ expression is then added to the reference surface as shown in Eq (25) to obtain $g(r,\theta)$. Eq (25) represents the spherical coordinate expression for the radome's second surface and possesses the characteristic of being differentiable with respect to all coordinate variables over the desired range of θ values. It is evident from Eq (25) that $g(r,\theta)$ identically equals zero when $r = A(\theta)$ for the desired range of r and θ values. Therefore, the equation of the second surface can be simplified as shown in Eqs (26) thru (28).

$$x'(\theta) = \sqrt{R_r^2 - z'(\theta)^2} + W_r/2 - R_r$$
$$z'(\theta) = \Big[R_o(\theta) + t(\theta)\Big]\cos(\theta) \qquad (23)$$

$$tz(\theta) = \sqrt{\Big[R_o(\theta) + t(\theta)\Big]^2 - z'(\theta)^2} - x'(\theta)$$
$$tz(\theta) = A(\theta)\sin(\theta) - \sqrt{R_r^2 - A^2(\theta)\cos^2(\theta)} - W_r/2 + R_r \qquad (24)$$
$$where:\ \ A(\theta) = R_o(\theta) + t(\theta)$$

34

$$g(r,\theta) = g_{ref}(r,\theta) + tz(\theta) = 0$$

$$g(r,\theta) = \left\{ \begin{array}{c} \sqrt{R_r^2 - r^2\cos^2(\theta)} - \sqrt{R_r^2 - A^2(\theta)\cos^2(\theta)} \\ + [A(\theta) - r]\sin(\theta) \end{array} \right\} = 0 \qquad (25)$$

$$g(r,\theta) = A(\theta) - r = R_o(\theta) + t(\theta) - r = 0 \qquad (26)$$

$$g(r,\theta) = \sqrt{R_r^2 - K_r^2\cos^2(\theta)} - K_r\sin(\theta) + t(\theta) - r = 0$$

$$for \ \ K_r = R_r - \frac{W_r}{2} \qquad (27)$$

$$g(r,\theta) = \sqrt{R_r^2 - \left(R_r - W_r/2\right)^2\cos^2(\theta)} - \left(R_r - W_r/2\right)\sin(\theta) + t(\theta) - r = 0 \qquad (28)$$

$$for \ \left\{W_r/2 + t(\pi/2)\right\} \leq r \leq \left\{L_r + t(0)\right\} \ \ and \ \ 0 \leq \theta \leq \pi/2$$

35

3.3 Multi-Layer Development

Extending the single layer derivation process to the multi-layer radome is the next task. The radome geometry and coordinate orientation for an m-layer radome are shown in Figure 8. For the multi-layer development, let:

m = Total number of radome layers, including any resulting from the introduction of an artificial reference surface.

k = Total number of radome layers inside the reference surface, $0 \leq k \leq m$.

i = Surface number under consideration, $1 \leq i \leq m+1$.

$t_i(\theta)$ = Taper of the ith layer relative to the ith surface, specified in the $\hat{r}$ direction.

$ts_i(\theta)$ = Taper "*sum*" (equivalent taper) of the ith layer relative to the reference surface.
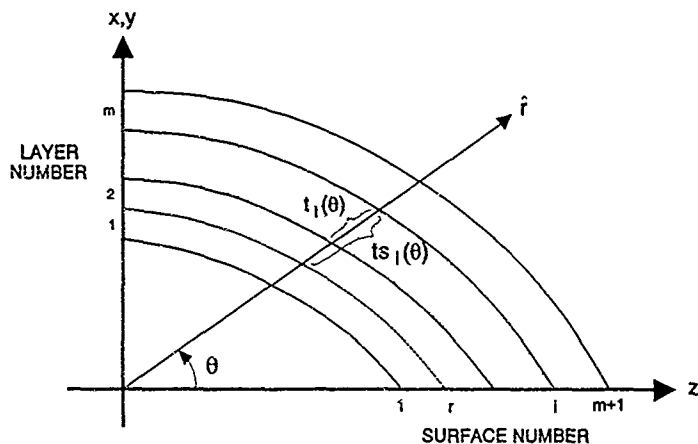
Figure 8. Multi-Layer Radome Geometry

36

For the m-layer radome there are a total of $m+1$ surfaces for which equations must be generated. As with the single layer radome development, the surface labeled r in Figure 8 is a "*true*" tangent ogive surface used as a reference. The *reference* surface r need <u>NOT</u> be an actual surface of a radome layer. An "*artificial*" reference surface may be introduced anywhere between the radome's inner and outer surfaces provided the taper functions $ts_i(\theta)$ and $t_i(\theta)$ can be specified for each radome surface.

The following derivation and analysis process applies to any arbitrarily shaped radome which when oriented as shown in Figure 8, 1) has all layer surfaces independent of ϕ, i.e., symmetric about the z-axis in any given ϕ plane, 2) has at least one surface which satisfies the tangent ogive equation $g_{ref}(r,\theta)$ or at least a cross-sectional area such that a tangent ogive curve lies entirely between the radome's inner and outer surface, thereby allowing for an artificial reference surface to be introduced, and 3) is constructed such that a taper function $t_i(\theta)$ can be determined/described for each layer, including any artificial layers introduced by an artificial reference surface.

Considering the ith surface of the multi-layer radome, the first task is to derive an expression for the total taper sum $ts_i(\theta)$. As previously defined, $ts_i(\theta)$ represents the "*sum*" or equivalent taper of the ith radome surface relative to the reference surface Once calculated $ts_i(\theta)$ can be substituted into the $A(\theta)$ expression of Eq (26) to obtain $g(r,\theta)$. $G_i(r,\theta)$ represents the surface equation describing the shape of the ith surface. For a given θ value the taper function for the inner most radome surface $ts_1(\theta)$ can be expressed as shown in Eq (29).

37

$$ts_1(\theta) = -\sum_{j=1}^{k} t_j(\theta) \tag{29}$$

The taper value of the inner most surface for a specified θ value is simply the negative of the sum of all $t_j(\theta)$ values prior to the reference surface. Therefore, the taper value for the ith surface is obtained by adding the sum of all $t_j(\theta)$ values prior to the ith surface to $ts_1(\theta)$ as shown in Eq (30). Given Eq (30) the final mathematical expression for $ts_i(\theta)$ is obtained by the development process provided in Eqs (31) thru (35), resulting in the final expression as given by Eq (36).

$$ts_i(\theta) = \sum_{\substack{j=1 \\ i\ne1}}^{(i-1)} t_j(\theta) + ts_1(\theta) = \sum_{j=1}^{(i-1)} t_j(\theta) - \sum_{l=1}^{k} t_l(\theta) \tag{30}$$

$$for\ 1 \le i \le m+1$$

Expanding The Finite Sum Expression:

$$ts_i(\theta) = \left\{ \begin{array}{l} + \left[t_1(\theta) + t_2(\theta) + ... + t_{i-1}(\theta) \right] \\ - \left[t_1(\theta) + t_2(\theta) + ... + t_k(\theta) \right] \end{array} \right\} \tag{31}$$

For $k > (i-1)$

$$ts_i(\theta) = -\left\{ t_i(\theta) + t_{i+1}(\theta) + .. + t_k(\theta) \right\} \tag{32}$$

38

$$For \ k < (i-1)$$

$$ts_i(\theta) = +\left\{t_{k+1}(\theta) + t_{k+2}(\theta) + \ldots + t_{i-1}(\theta)\right\} \tag{33}$$

$$For \ k = (i-1)$$

$$ts_i(\theta) = 0 \tag{34}$$

Define Signum$(i-k-1)$ *as Follows·*

$$sgn(i-k-1) \equiv \begin{cases} -1, & i < (k+1) \\ 0, & i = (k+1) \\ +1, & i > (k+1) \end{cases} \tag{35}$$

Letting $q = \max(i-1,k)$ *and* $s = \min(i-1,k) + 1$ *then,*

$$ts_i(\theta) = sgn(i-k-1)\sum_{j=s}^{q} t_j(\theta) \tag{36}$$

$$for \ 1 \leq i \leq m+1$$

The $ts_i(\theta)$ function of Eq (36) represents the total taper value to be added to the reference surface for any given value of θ. It can be substituted directly into the single layer radome $A(\theta)$ expression of Eq (26) to provide the final form expression for $g(r,\theta)$. The final expressions obtained are as given by Eqs (37) and (38). As with $g_{ref}(r,\theta)$ and $g(r,\theta)$, $g(r,\theta)$ is independent of ϕ and is differentiable with respect to both r and θ over the specified variable ranges.

$$g_i(r,\theta) = A_i(\theta) - r = R_o(\theta) + ts_i(\theta) - r = 0 \tag{37}$$

$$g_i(r,\theta) = \sqrt{R_r^2 - \left(R_r - W_r/2\right)^2 \cos^2(\theta)} - \left(R_r - W_r/2\right)\sin(\theta) + ts_i(\theta) - r = 0 \tag{38}$$

$$for \ \ 1 \le i \le m+1 \ \ , \ \ 0 \le \theta \le \pi/2$$

$$and \ \ \left[W_r/2 + ts_i(\pi/2) \right] \le r \le \left[L_r + ts_i(0) \right]$$

Since $ts_i(\theta)$ can be explicitly solved for in Eq (38), this equation proves to be very useful if the introduction of an "*artificial*" reference surface is required. Given the r-θ profile for one of the radome's actual surfaces, i.e., a set of (r,θ) points which lie on the actual radome surface, a corresponding $ts(\theta)$ profile is obtainable via direct substitution of the (r,θ) values into Eq (38). Numerical interpolation and approximation techniques such as Lagrangian, Hermite, cubic splines, etc., may then be employed to develop the required $ts(\theta)$ function [18] The only restriction on the best fit approximation is that the $ts(\theta)$ function derived be at least once differentiable with respect to θ.

The GO ray tracing method employed requires a surface normal to be obtained for any arbitrary point on the ith surface. Since Eq (38) mathematically describes the ith surface and varies only as a function spherical coordinates r and θ, a spherical coordinate gradient may be utilized to calculate surface normal vectors. The spherical gradient vector components $G_r(r,\theta)$ and $G_{th}(r,\theta)$ are next calculated. From

40

the definition for the spherical gradient of a function varying only in r and θ, Eq (39), the normal vector components are obtained.

$$\nabla g_i(r,\theta) = \frac{\partial}{\partial r}\Big[g_i(r,\theta)\Big]\,\hat{r} + \frac{1}{r}\frac{\partial}{\partial \theta}\Big[g_i(r,\theta)\Big]\,\hat{\theta}$$

$$= G_{r_i}(r,\theta)\,\hat{r} + G_{th_i}(r,\theta)\,\hat{\theta} \tag{39}$$

$$G_{r_i}(r,\theta) = \frac{\partial}{\partial r}\Big[g_i(r,\theta)\Big] = -1 \tag{40}$$

$$G_{th_i}(r,\theta) = \frac{1}{r}\frac{\partial}{\partial \theta}\Big[g_i(r,\theta)\Big]$$

$$= \frac{1}{r}\frac{\partial}{\partial \theta}\Big[\sqrt{R_r^2 - K_r^2\cos^2(\theta)} - K_r\sin(\theta) + ts_i(\theta) - r\,\Big] \tag{41}$$

$$G_{th_i}(r,\theta) = \frac{(1/2)(-K_r^2)(2\cos\theta)(-\sin\theta)}{r\sqrt{R_r^2 - K_r^2\cos^2(\theta)}} - \frac{K_r\cos\theta}{r} + \frac{1}{r}\frac{d}{d\theta}\Big[ts_i(\theta)\Big] \tag{42}$$

$$G_{th_i}(r,\theta) = \frac{K_r\cos(\theta)}{r}\left\{\frac{K_r\sin(\theta)}{\sqrt{R_r^2 - K_r^2\cos^2(\theta)}} - 1\right\} + \frac{1}{r}\frac{d}{d\theta}\Big[ts_i(\theta)\Big] \tag{43}$$

$$where \quad K_r = R_r - W_r/2$$

41

The expressions given by Eqs (40) and (43) for $G_r(r,\theta)$ and $G_{th}(r,\theta)$ are the result of taking partial derivatives of $g(r,\theta)$ with respect to r and θ, respectively. These results are substituted into Eq (39) to obtain the surface normal vector.

3.4 Taper Functions

Two specific radome taper functions are considered, namely, 1) a constant taper thickness as measured along the radome surface normal direction and 2) an "*ideal*" taper function based on constant electrical thickness as a function of look angle θ. The constant thickness taper development is included here for completeness and validation purposes. Radomes with constant thickness tapers are perhaps the most extensively analyzed in literature. Therefore, a wealth of empirical and measured range data exists for verification of analysis and modeling results. The concept of an "*ideal*" taper function is introduced as a means by which an optimum radome taper may be developed. Similar to the multi-layer surface equation development, the "*ideal*" taper function development is unique to this research effort.

Under the assumption of locally-planar surfaces at ray-radome intersection points, transmission characteristics of Electromagnetic (EM) waves can be derived using dielectric slab propagation methods. As an EM wave propagates through a dielectric slab it will experience a phase change, i.e., a phase shift as it propagates from the incident surface to the transmit surface. For both the constant and "*ideal*" taper function developments it is necessary to introduce the concept of "electrical thickness". Letting ϕ_e represent the amount of phase shift as measured at points along the surface normal direction, the "electrical thickness" d_e of a lossless dielectric

42

slab can be expressed as shown in Eq (44). In this equation d_n represents the slab thickness as measured along the surface normal direction, λ is the free-space wavelength of the propagating wave, ϵ_r is the relative dielectric constant of the slab, and θ_i is the incidence/design angle between the surface normal vector and wave propagation direction vector. Letting $\phi_s = N\pi$ in Eq (44) results in what is called an "Nth-order wall" satisfying the expression given by Eq (45) [6, 7].

$$d_e = \frac{\phi_s}{2\pi} = \frac{d_n}{\lambda}\sqrt{\epsilon_r - \sin^2\theta_i} \quad (Wavelengths) \tag{44}$$

For an Nth-Order Dielectric Slab :

$$d_n = \frac{N\lambda}{2\sqrt{\epsilon_r - \sin^2\theta_i}} \quad for \quad N = 1,2,3,... \tag{45}$$

Two commonly considered cases are when $N = 1$ and $N = 2$, corresponding to "*half-wave*" wall and "*full-wave*" wall designs at the specified design angle of θ_i. All Nth-order wall designs exhibit characteristics such that reflections from the transmit surface cancel reflections from the incident surface, thereby, resulting in maximum transmission of the incident wave. Also, at the design angle both parallel and perpendicular polarization components experience zero reflection, maximum and equal transmittance, and equal insertion phase delays. These characteristics and Eq (45) strictly hold for lossless materials but are good approximations for the low-loss materials normally used in radome structures [7].

43
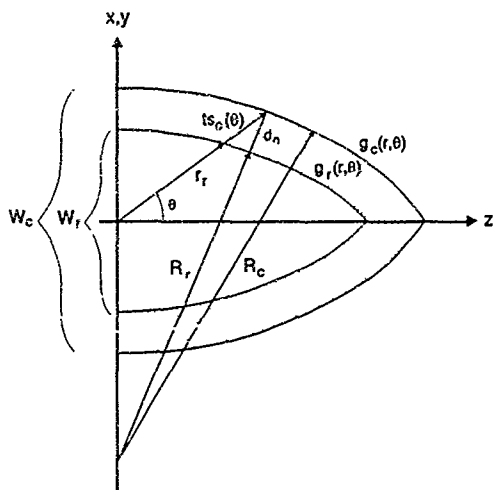
Figure 9. Geometry For Constant Taper Function

3.4.1 Constant Taper Function. For constant thickness radomes an "*optimum*" combination of dielectric constant and design angle θ_i is selected by theoretical or empirical methods. With N, ϵ_r, and θ_i specified, Eq (45) is used to calculate the appropriate normal thickness d_n. Relative to a tangent ogive reference surface, a constant taper generates an additional ogive surface located either inside or outside of the reference surface. The new surface generated must satisfy Eq (46) where the subscript "c" is used to denote "*constant*" surface quantities as identified in Figure 9.

$$g_c(r_c, \theta) = \sqrt{R_c^2 - r_c^2 \cos^2\theta} - r_c \sin\theta + W_c/2 - R_c = 0$$

$$\rightarrow \quad r_c = \bar{K}_c \sin\theta + \sqrt{R_c^2 - \bar{K}_c^2 \cos^2\theta} \quad for \quad \bar{K}_c = W_c/2 - R_c$$

(46)

44

$$g_r(r_r,\theta) = \sqrt{P_r^2 - r_r^2 \cos^2\theta} - r_r \sin\theta + W_r/2 - R_r = 0 \tag{47}$$

$$\rightarrow \quad r_r = \bar{K}_r \sin\theta + \sqrt{R_r^2 - \bar{K}_r^2 \cos^2\theta} \quad for \quad \bar{K}_r = W_r/2 - R_r$$

Given the tangent ogive reference surface parameters R_r and W_r, spherical coordinate r_r may be expressed as given by Eq (47). From Figure 9 it is apparent that $ts_c(\theta) = r_c - r_r$ for all $0 \leq \theta \leq \pi/2$. Using this relationship and Eqs (46) and (47) the taper sum function of Eq (48) is obtained where the additional relationship that $\bar{K}_c = \bar{K}_r$ has been utilized. This taper sum expression is substituted into the $g_r(r,\theta)$ expression of Eq (38) to obtain the final surface equation for a constant thickness taper. The derivation process is completed by differentiating $ts_c(\theta)$ with respect to θ. Results are shown in Eq (49) which is the required derivative term for calculating surface gradient components of Eq (43). It can be shown that Eq (49) is valid over the required θ range.

$$ts_c(\theta) = r_c - r_r$$

$$= \sqrt{R_c^2 - \bar{K}_r^2 \cos^2\theta} - \sqrt{R_r^2 - \bar{K}_r^2 \cos^2\theta} \tag{48}$$

$$= \sqrt{\left(R_r + d_n\right)^2 - \bar{K}_r^2 \cos^2\theta} - \sqrt{R_r^2 - \bar{K}_r^2 \cos^2\theta}$$

$$\frac{d}{d\theta}\left\{ts_c(\theta)\right\} = \bar{K}_r^2 \cos\theta \sin\theta \left\{ \frac{1}{\sqrt{\left(R_r + d_n\right)^2 - \bar{K}_r^2 \cos^2\theta}} - \frac{1}{\sqrt{R_r^2 - \bar{K}_r^2 \cos^2\theta}} \right\} \tag{49}$$

3.4.2 "Ideal" Taper Function. If for every possible combination of antenna element location and propagation direction the radome normal thickness d_n can be modified, i.e., varied in accordance with Eq (45) such that each propagating ray experiences equivalent amplitude attenuation and phase delay, the radome would possess *"ideal"* propagation characteristics. The term *"ideal"* implies the radome is *"transparent"* to an incident uniform plane wave, i.e., introduces minimal or no variation on either the amplitude or phase; this *"ideal"* situation is impossible to achieve under realistic conditions. However, given a specific element location within the array and a desired scan plane, in conjunction with specified radome geometry, it is possible to utilize Eq (45) to develop/establish what will be referred to as an *"ideal"* taper function.

Considering the geometry established in Figure 10 where $g_i(r,\theta)$ is a given surface equation for the i-th radome surface, the goal is to determine taper function $t_i(\theta)$ such that $g_{i+1}(r,\theta)$ can be represented as the sum of $g_i(r,\theta)$ and $t_i(\theta)$ for $0 \leq r \leq r_{max}$ and $0 \leq \theta \leq \pi/2$. Given θ' is varied in the arbitrary $\phi' = 0$ plane, $0 \leq \theta' \leq \pi/2$, it is possible to calculate an *"ideal"* $t_i(\theta)$ utilizing Eq (45). The taper function developed is *ideal* only for the element location under consideration, i.e., an element located at the aperture center. This is a reasonable choice considering how amplitude weights are typically maximum at this point. Given any other element location, the radome thickness d_n or $t_i(\theta)$ value seen by an emanating ray will be less than optimum, i.e., will generally not satisfy Eq (45) for the given θ scan direction and calculated incidence angle θ_i. Eqs (50) thru (55) summarize the process for calculating an *"ideal"* taper function $t_i(\theta)$.

46
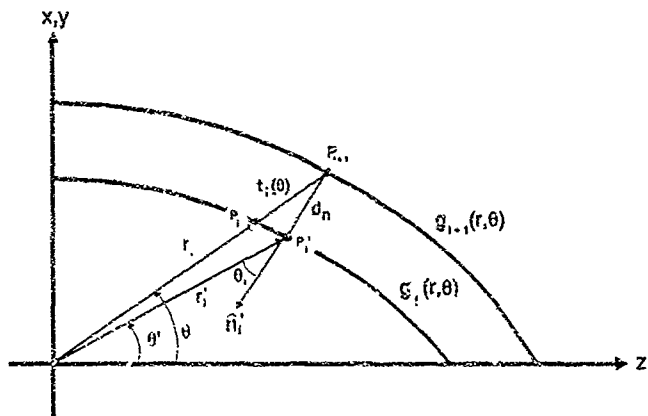
Figure 10. Geometry For Establishing "Ideal" Taper Functions

Given θ', $g_i(r,\theta) = 0$, and $\phi' = 0$:

$$r_i' < r \ni g_i(r,\theta) = 0$$

$$\vec{r}_i' = r_i' \sin\theta' \, \hat{x} + r_i' \cos\theta' \, \hat{z} \tag{50}$$

$$\hat{r}_i' = \frac{\vec{r}_i'}{|\vec{r}_i'|} = \sin\theta' \, \hat{x} + \cos\theta' \, \hat{z}$$

For $\hat{n}_i'$ at P_i': $\quad \hat{n}_i' = \frac{\nabla g_i(r_i',\theta')}{|\nabla g_i(r_i',\theta')|}$, $\quad \theta_i = \cos^{-1}\left\{ -\hat{r}_i' \cdot \hat{n}_i' \right\} \tag{51}$

47

$$\text{Given} \quad \theta_i \quad \text{and} \quad \sin^2\theta_i = 1 - \cos^2\theta_i = 1 - \left(\hat{r}_i' \cdot \hat{n}_i'\right)^2$$

$$\text{then} \quad d_n = \frac{N\lambda}{2\sqrt{e_r + \left(\hat{r}_i' \cdot \hat{n}_i'\right)^2 - 1}} \tag{52}$$

$$\text{On The } \iota+1 \text{ Surface}, \quad g_{i+1}(r,\theta) = 0,$$

$$\vec{P}_{i+1} = \vec{r}_i' - d_n \hat{n}_i' \quad , \quad \hat{P}_{i+1} = \frac{\vec{r}_i' - d_n \hat{n}_i'}{|\vec{r}_i' - d_n \hat{n}_i'|} \tag{53}$$

$$\theta = \cos^{-1}\left(\hat{P}_{i+1} \cdot \hat{z}\right) = \cos^{-1}\left\{\frac{\vec{r}_i' \cdot \hat{z} - d_n\left(\hat{n}_i' \cdot \hat{z}\right)}{|\vec{r}_i' - d_n \hat{n}_i'|}\right\} \tag{54}$$

$$\text{Given} \quad \theta \quad , \quad g_i(r,\theta) = 0 \quad \text{and} \quad r_i = r \ni g_i(r,\theta) = 0 \,,$$

$$\tilde{q}(\theta) = |\vec{P}_{i+1}| - r_i = |\vec{r}_i' - d_n \hat{n}_i'| - r_i \tag{55}$$

For typical radome geometries including a tangent ogive the above process seldom leads to a closed-form solution for $t_i(\theta)$. Numerical techniques are employed to calculate θ and $t_i(\theta)$ by varying θ' over its full range of values. Curve fitting techniques to are used to arrive at a functional form approximation for $t_i(\theta)$. It is evident from Figure 10 that the surface normal vector fails to exist at the radome tip. Numerical solution techniques must account for this in approximating $t_i(\theta)$ values for

48

small values of θ'. For radomes with high fineness ratios (greater than two) this presents little difficulty since in the radome tip region the value of θ rapidly approaches the value of θ'.

The numerical solution procedure is applied to the tangent ogive radome case previously considered by letting $g_t(r,\theta)$ represent a tangent ogive surface. A Fortran computer program was written to accept arbitrary ogive surface parameters, Radius (R) and Width (W), and arbitrary dielectric constants. The program varies the value of θ' over its range and generates a corresponding table of θ and $t_i(\theta)$ values. For a test case the program was run with ogive surface parameters of $R = 234.472\ \lambda$, $W = 36.1358\ \lambda$, and with a dielectric constant given by $\epsilon_r = 4.8$. The values of θ and corresponding $t_i(\theta)$ values generated are plotted in Figure 11 as indicated by the "$*$" symbols. These data points were input into a computer with curve-fitting capability which in turn provided a "best fit" equation; Eq (56) is the Gaussian equation returned from the curve-fitting routine. The dashed line in Figure 11 is a plot of Eq (56) showing a "near" perfect fit to the original input data points.

Gaussian Function For "IDEAL" Taper:

$$t_i(\theta) = 0.2267 + 0.6071 \exp\left\{ -.5\left[\frac{\theta + 0.3936}{0.5551} \right]^2 \right\} \tag{56}$$

49
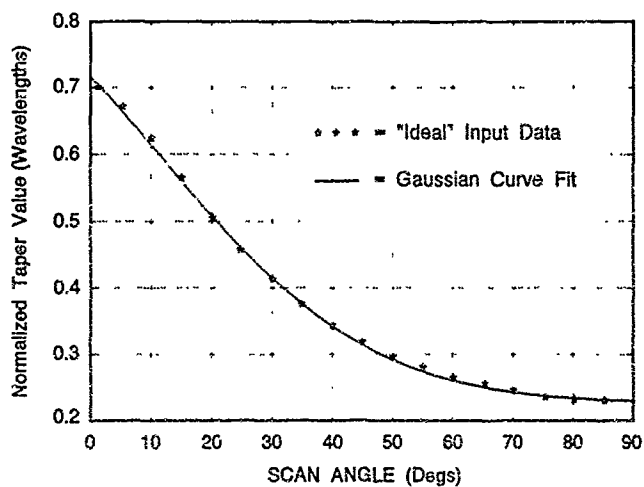
Figure 11. "Ideal" Taper Function For Tangent Ogive Reference

IV. Radome Reflection Points

4.1 Introduction

This chapter provides the motivation and methodology for calculating wavefront reflection points on a radome's inner surface. A Geometric Optics (GO) approach is used to analyze and predict overall reflection performance. As noted previously, a significant portion of the discrepancy between measured and numerically predicted boresight errors is caused by reflections within the radome interior [6]. Hence, to obtain accurate and reliable boresight error estimates such internal reflections must be taken into account in the development of sound radome models. Primary reflection points within a radome account for a major portion of the total reflected energy received/transmitted by the aperture. The following development concentrates on calculating primary reflected rays only as a first order approximation to overall reflection effects. A primary reflected ray is considered to be any ray which encounters at most a single transmission point and single reflection point while propagating from outside the radome to a point within the radome on the aperture plane.

The geometry and conventions established in Figure 12 are used throughout the discussion. The point identified as (x_r, y_r, z_r) represents the "*rotated*" antenna element position for a particular element in the aperture plane with its associated "*critical*" or reflection point(s) given by (x_c, y_c, z_c). All critical points lie on an arbitrary radome surface specified by $g(x,y,z) = 0$ as indicated in Figure 12. The vector $\hat{k}$ represents the desired direction of propagation with components $<k_x, k_y, k_z>$. For this

51

geometrical representation, the problem/objective can be stated as follows: "Given the point (x_r, y_r, z_r) and the desired propagation direction $\hat{k}$, determine the coordinate(s) of the point(s) (x_c, y_c, z_c) satisfying $g(x,y,z) = 0$ such that a ray emanating from (x_r, y_r, z_r) intersects the radome surface at (x_c, y_c, z_c) and reflects in the $\hat{k}$ direction.
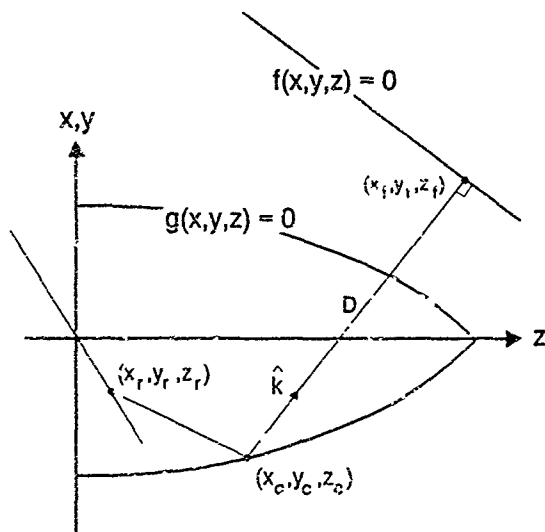
Figure 12. Reflection Point Geometry

4.2 Generalized Variational Solution

The method of approach to solve the problem is to invoke Fermat's principle and then apply variational calculus to obtain the critical points. First, a planar reference surface $f(x,y,z) = 0$ is established as in Figure 12 with normal vector $\hat{k}$ and located at a distance D from the aperture plane. As shown, the point (x_f, y_f, z_f) is the *"final"* intersection point of a ray which emanates from (x_c, y_c, z_c), propagates in the $\hat{k}$ direction, and strikes the $f(x,y,z) = 0$ normally. The problem statement may now be modified by application of Fermat's principle: "Given the points (x_i, y_i, z_i) and (x_f, y_f, z_f), subject to the constraints that (x_i, y_i, z_i) be in the aperture plane and (x_f, y_f, z_f) lie on the reference plane, find the path which requires minimum propagation time from (x_i, y_i, z_i) to (x_f, y_f, z_f) such that the point (x_c, y_c, z_c) is on the path and $g(x_c, y_c, z_c) = 0$." As now stated, the problem is a classical variational calculus problem.

The following development is based on classical variational calculus techniques. Conventions and notations used here closely parallel those used by Gelfand and Fomin and were adopted primarily for convenience and consistency purposes. As given by Gelfand and Fomin [19], the functional $J[x,y,z]$ for a variational calculus problem involving Fermat's principle in three dimensional space is as given by Eq (57).

$$J[x,y,z] = \int_{t_i}^{t_f} \frac{\sqrt{x^2(t) + y^2(t) + z^2(t)}}{v[x(t), y(t), z(t)]} \, dt = \int_{t_i}^{t_f} F[x,y,z,\dot{x},\dot{y},\dot{z}] \, dt \qquad (57)$$

In Eq (57) t_i represents the fixed *"initial"* time at starting point (x_i, y_i, z_i) and variable t_f is the *"final"* time at the ending point (x_f, y_f, z_f). The functions $x(t)$, $y(t)$ and $z(t)$ are parametric representations of corresponding rectangular coordinates x, y, and z. The function $v(x,y,z)$ represents the positional velocity of the medium through which the wave/particle must traverse in going from the initial to final points. Since the problem at hand requires that the ray intersect the radome wall at (x_c, y_c, z_c) along the path, the functional of Eq (57) is rewritten as the sum of two functionals as given by Eq (58), with variable time t_c being introduced as the *"critical"* time at which the wave/particle reaches the critical point. The subscripts "1" and "2" are used to distinguish between the two different regions of integration and an additional constraint/boundary condition is added as a result. Since the overall solution which minimizes $J[x,y,z]$ must be continuous, i.e., a continuous path from the initial to final points, boundary conditions must be enforced at (x_c, y_c, z_c) such that $x_1(t_c) = x_2(t_c)$, $y_1(t_c) = y_2(t_c)$, and $z_1(t_c) = z_2(t_c)$.

$$J[x,y,z] = J_1[x_1,y_1,z_1] + J_2[x_2,y_2,z_2]$$

$$= \int_{t_i}^{t_c} F_1\left[x_1,y_1,z_1,\dot{x}_1,\dot{y}_1,\dot{z}_1\right]dt + \int_{t_c}^{t_f} F_2\left[x_2,y_2,z_2,\dot{x}_2,\dot{y}_2,\dot{z}_2\right]dt \tag{58}$$

For a functional of the form given by Eq (58), the variation may be expressed as given by Eqs (59) thru (61) [19]. A necessary condition for the functions $x_1(t)$, $y_1(t)$, and $z_1(t)$ to minimize $J_1[x,y,z]$, and $x_2(t)$, $y_2(t)$, and $z_2(t)$ to minimize $J_2[x,y,z]$ is that the variation expressions given by Eqs (60) and (61) vanish for all admissible

54

functions, i.e., $\delta J_1[x,y,z] = \delta J_2[x,y,z] = 0$. A necessary condition for each variation to vanish is that the system of Euler's Equations given by Eqs (62) and (63) be satisfied for each variation $\delta J_1[x,y,z]$ and $\delta J_2[x,y,z]$.

$$\delta J[x,y,z] = \delta J_1[x_1,y_1,z_1] + \delta J_2[x_2,y_2,z_2] \tag{59}$$

$$\delta J_1[x_1,y_1,z_1] = \int_{t_i}^{t_c} \left\{ \left(\frac{-d}{dt} F_{1x_1} \right) h_1(t) + \left(\frac{-d}{dt} F_{1y_1} \right) h_2(t) + \left(\frac{-d}{dt} F_{1z_1} \right) h_3(t) \right\} dt \tag{60}$$

$$+ \left(F_{1x_1} \delta x_1 + F_{1y_1} \delta y_1 + F_{1z_1} \delta z_1 \right) \Big|_{t_i}^{t_c} + \left(F_1 - \dot{x}_1 F_{1x_1} - \dot{y}_1 F_{1y_1} - \dot{z}_1 F_{1z_1} \right) \Big|_{t_i}^{t_c}$$

$$\delta J_2[x_2,y_2,z_2] = \int_{t_c}^{t_f} \left\{ \left(\frac{-d}{dt} F_{2x_2} \right) h_4(t) + \left(\frac{-d}{dt} F_{2y_2} \right) h_5(t) + \left(\frac{-d}{dt} F_{2z_2} \right) h_6(t) \right\} dt \tag{61}$$

$$+ \left(F_{2x_2} \delta x_2 + F_{2y_2} \delta y_2 + F_{2z_2} \delta z_2 \right) \Big|_{t_c}^{t_f} + \left(F_2 - \dot{x}_2 F_{2x_2} - \dot{y}_2 F_{2y_2} - \dot{z}_2 F_{2z_2} \right) \Big|_{t_c}^{t_f}$$

$$F_{1x_1} - \frac{d}{dt}\left(F_{1x_1} \right) = 0 \quad ; \quad F_{1y_1} - \frac{d}{dt}\left(F_{1y_1} \right) = 0 \quad ; \quad F_{1z_1} - \frac{d}{dt}\left(F_{1z_1} \right) = 0 \tag{62}$$

$$F_{2x_2} - \frac{d}{dt}\left(F_{2x_2} \right) = 0 \quad ; \quad F_{2y_2} - \frac{d}{dt}\left(F_{2y_2} \right) = 0 \quad ; \quad F_{2z_2} - \frac{d}{dt}\left(F_{2z_2} \right) = 0 \tag{63}$$

55

Assuming a homogenous medium exists over both regions of integration, the velocity of propagation within the medium is independent of position, resulting in $v_1(x_1,y_1,z_1) = v_1 = $ constant and $v_2(x_2,y_2,z_2) = v_2 = $ constant. For this case, the Euler's Equations given by Eqs (62) and (63) reduce to expressions given in Eqs (64) and (65) after the appropriate partial derivatives of $F_1[x_1,y_1,z_1,\dot{x}_1,\dot{y}_1,\dot{z}_1]$ and $F_2[x_2,y_2,z_2,\dot{x}_2,\dot{y}_2,\dot{z}_2]$ are taken. Each of these equations represents a system of first-order differential equations. As expected for a homogeneous medium, the general solution to these two systems of equations, and hence the general solution to the Euler's Equations, is a set of linear equations of the form given by Eq (66). Therefore, any set of $x(t)$, $y(t)$, and $z(t)$ functions satisfying Eq (66) cause the integral terms of both $\delta J_1[x_1,y_1,z_1]$ and $\delta J_2[x_2,y_2,z_2]$ to vanish and are candidate solutions for minimizing the functional of Eq (58).

$$\frac{-d}{dt}\left(F_{1\dot{x}_1}\right) = 0 \quad \rightarrow \quad F_{1\dot{x}_1} = K_1 \quad \rightarrow \quad \frac{\dot{x}_1(t)}{F_1[x_1,y_1,z_1,\dot{x}_1,\dot{y}_1,\dot{z}_1]} = K_1$$

$$\frac{-d}{dt}\left(F_{1\dot{y}_1}\right) = 0 \quad \rightarrow \quad F_{1\dot{y}_1} = K_2 \quad \rightarrow \quad \frac{\dot{y}_1(t)}{F_1[x_1,y_1,z_1,\dot{x}_1,\dot{y}_1,\dot{z}_1]} = K_2 \qquad (64)$$

$$\frac{-d}{dt}\left(F_{1\dot{z}_1}\right) = 0 \quad \rightarrow \quad F_{1\dot{z}_1} = K_3 \quad \rightarrow \quad \frac{\dot{z}_1(t)}{F_1[x_1,y_1,z_1,\dot{x}_1,\dot{y}_1,\dot{z}_1]} = K_3$$

$$\frac{-d}{dt}\left(F_{2\dot{x}_2}\right) = 0 \quad \rightarrow \quad F_{2\dot{x}_2} = K_4 \quad \rightarrow \quad \frac{\dot{x}_2(t)}{F_2[x_2,y_2,z_2,\dot{x}_2,\dot{y}_2,\dot{z}_2]} = K_4$$

$$\frac{-d}{dt}\left(F_{2\dot{y}_2}\right) = 0 \quad \rightarrow \quad F_{2y_2} = K_5 \quad \rightarrow \quad \frac{\dot{y}_2(t)}{F_2[x_2,y_2,z_2,\dot{x}_2,\dot{y}_2,\dot{z}_2]} = K_5 \qquad (65)$$

$$\frac{-d}{dt}\left(F_{2\dot{z}_2}\right) = 0 \quad \rightarrow \quad F_{2\dot{z}_2} = K_6 \quad \rightarrow \quad \frac{\dot{z}_2(t)}{F_2[x_2,y_2,z_2,\dot{x}_2,\dot{y}_2,\dot{z}_2]} = K_6$$

$$
\begin{aligned}
x_1(t) &= a_1 t + a_o & x_2(t) &= A_1 t + A_o \\
y_1(t) &= b_1 t + b_o & y_2(t) &= B_2 t + B_o \\
z_1(t) &= c_1 t + c_o & z_2(t) &= C_2 t + C_o \\
t &\in \left[t_i, t_c\right] & t &\in \left[t_c, t_f\right]
\end{aligned}
\qquad (66)
$$

Given that candidate functions are chosen which satisfy the system of Euler's Equations, the variation expressions given by Eqs (60) and (61) can be recast in the form given by Eq (61) for each of the regions being considered. These expressions are further simplified by noting that the second term of each equation identically equals zero for all admissible functions $x(t)$, $y(t)$, and $z(t)$, when the required partial derivatives are taken as illustrated in Eq (68). By applying the results of Eq (68) to Eq (67), the variation expression given by Eq (69) is obtained where the evaluation process has been applied at the upper and lower limits and the terms combined into a single variation expression.

57

$$\delta J_1[x_1, y_1, z_1] = \left\{ \begin{array}{l} \left(F_{1x_1}\delta x_1 + F_{1y_1}\delta y_1 + F_{1z_1}\delta z_1 \right)\bigg|_{t=t_i}^{t=t_c} \\ \\ + \left(F_1 - \dot{x}_1 F_{1x_1} - \dot{y}_1 F_{1y_1} - \dot{z}_1 F_{1t_1} \right)\bigg|_{t=t_i}^{t=t_c} \end{array} \right\} \tag{67}$$

$$\delta J_2[x_2, y_2, z_2] = \left\{ \begin{array}{l} \left(F_{2x_2}\delta x_2 + F_{2y_2}\delta y_2 + F_{2z_2}\delta z_2 \right)\bigg|_{t=t_c}^{t=t_f} \\ \\ + \left(F_2 - \dot{x}_2 F_{2x_2} - \dot{y}_2 F_{2y_2} - \dot{z}_2 F_{2z_2} \right)\bigg|_{t=t_c}^{t=t_f} \end{array} \right\}$$

$$\left(F_n - x_n F_{nx_n} - \dot{y}_r F_{ny_n} - \dot{z}_n F_{nz_n} \right) = \left\{ \begin{array}{cc} \sqrt{\dot{x}_n^2 + \dot{y}_n^2 + \dot{z}_n^2} & - \dfrac{\dot{x}_n^2}{\sqrt{\dot{x}_n^2 + \dot{y}_n^2 + \dot{z}_n^2}} \\ \\ - \dfrac{\dot{y}_n^2}{\sqrt{\dot{x}_n^2 + \dot{y}_n^2 + \dot{z}_n^2}} & - \dfrac{\dot{z}_n^2}{\sqrt{\dot{x}_n^2 + \dot{y}_n^2 + \dot{z}_n^2}} \end{array} \right\} = 0 \tag{68}$$

$$For \quad n = 1,2$$

$$\delta J[x,y,z] = \left(F_{1x_1}\delta x_1 + F_{1y_1}\delta y_1 + F_{1t_1}\delta z_1 \right)\bigg|_{t_c} - \left(\tilde{F}_{1x_1}\delta x_1 + F_{1y_1}\delta y_1 + F_{1z_1}\delta z_1 \right)\bigg|_{t_c} \tag{69}$$
$$+ \left(F_{2x_2}\delta x_2 + F_{2y_2}\delta y_2 + F_{2z_2}\delta z_2 \right)\bigg|_{t_f} - \left(F_{2x_2}\delta x_2 + F_{2y_2}\delta y_2 + F_{2z_2}\delta z_2 \right)\bigg|_{t_c}$$

Considering the initial point is specified at $t = t_i$, i.e., (x_i, y_i, z_i) is known, and that continuity conditions at $t = t_c$ must be enforced as expressed in Eq (70), a final

58

simplified variation expression is obtained as presented in Eq (71). The expression of Eq (71) must vanish for all admissible variations about critical point (x_o, y_o, z_c) and final point (x_f, y_f, z_f). As such, two separate cases are next considered, Case I is for no variation about the critical point and Case II is for no variation about the final point.

$$For \; (x_f, y_f, z_f) \; Given \cdot \quad \delta x_f = \delta y_f = \delta z_f = 0$$

$$By \; Continuity \; at \; t = t_c: \quad \left(\delta x_1 = \delta x_2\right)\Big|_{t_c} ; \left(\delta y_1 = \delta y_2\right)\Big|_{t_c} ; \left(\delta z_1 = \delta z_2\right)\Big|_{t_c} \tag{70}$$

$$\delta J[x,y,z] = \left(F_{1x_1} - F_{2x_2}\right)\delta x_c + \left(F_{1y_1} - F_{2y_2}\right)\delta y_c + \left(F_{1z_1} - F_{2z_2}\right)\delta z_c$$
$$+ \left(F_{2x_2}\delta x_f + F_{2y_2}\delta y_f + F_{2z_2}\delta z_f\right) \tag{71}$$

For Case I all variation about (x_f, y_f, z_f) is assumed to be zero such that $\delta x_f = \delta y_f = \delta z_f = 0$. This assumption leads to the expression given by Eq (72) which when rewritten using the vector convention established in Eq (73), results in the final dot product expression given by Eq (74). Since the dot product of the two vectors identically equals zero, the velocity and incremental vectors must be orthogonal to each other at the critical point.

$$For \; \delta x_f = \delta y_f = \delta z_f = 0$$

$$\delta J[x,y,z] = \left(F_{1x_1} - F_{2x_2}\right)\delta x_c + \left(F_{1y_1} - F_{2y_2}\right)\delta y_c + \left(F_{1z_1} - F_{2z_2}\right)\delta z_c \tag{72}$$

59

$$\text{Using}: F_{\dot{x}} = \frac{\dot{x}(t)}{F(*)} \quad ; \quad F_{\dot{y}} = \frac{\dot{y}(t)}{F(*)} \quad ; \quad F_{\dot{z}} = \frac{\dot{z}(t)}{F(*)}$$

$$\text{where } F(*) = F[x,y,z,\dot{x},\dot{y},\dot{z}] = \sqrt{\dot{x}^2(t) + \dot{y}^2(t) + \dot{z}^2(t)}$$

$$\text{Letting}: \vec{r}(t) = [x(t),y(t),z(t)]$$

$$\dot{\vec{r}}(t) = [\dot{x}(t),\dot{y}(t),\dot{z}(t)]$$

$$|\dot{\vec{r}}(t)| = \sqrt{\dot{x}^2(t) + \dot{y}^2(t) + \dot{z}^2(t)}$$

$$\text{Then}: \left(F_{\dot{x}}, F_{\dot{y}}, F_{\dot{z}}\right) = \frac{\dot{\vec{r}}(t)}{|\dot{\vec{r}}(t)|} = \hat{\dot{r}}(t)$$

(73)

$$\left\{ \left(\frac{\dot{x}_1(t_c)}{F_1(*)} - \frac{\dot{x}_2(t_c)}{F_2(*)} \right) \delta x_c + \left(\frac{\dot{y}_1(t_c)}{F_1(*)} - \frac{\dot{y}_2(t_c)}{F_2(*)} \right) \delta y_c + \left(\frac{\dot{z}_1(t_c)}{F_1(*)} - \frac{\dot{z}_2(t_c)}{F_2(*)} \right) \delta z_c \right\} = 0 \quad (74)$$

$$= \left[\hat{\dot{r}}_1(t_c) - \hat{\dot{r}}_2(t_c) \right] \cdot \left(\delta x_c, \delta y_c, \delta z_c \right) = 0$$

In a graphical sense incremental vector $(\delta x_c, \delta y_c, \delta z_c)$ represents the change in position of the critical point on the inner radome surface. Therefore, allowing for variation of the critical point requires that conditions of the original problem statement be enforced, i.e., $(x_c + \delta x_c, y_c + \delta y_c, z_c + \delta z_c)$ must satisfy $g(x,y,z) = 0$. The results of applying this constraint are summarized in Eqs (75) thru (78). In arriving at the final expression given by Eq (78) an incremental form of a Taylor series expansion is employed. Enforcing the conditions that 1) the point (x_c, y_c, z_c) satisfy

60

$g(x,y,z) = 0$ and 2) the incremental variations δx_c, δy_c, and δz_c are very small, results in the simplified expression for the dot product of $\nabla g(x_c, y_c, z_c)$ and incremental vector $(\delta x_c, \delta y_c, \delta z_c)$ as given by Eq (78)

$$g\left(x_c + \delta x_c, y_c - \delta y_c, z_c + \delta z_c\right) = 0 \tag{75}$$

Using The Incremental Form of Taylor Series

$$f(x+h, y+k, z+m) - f(x,y,z) + \left(hf_x + kf_y + mf_z\right) \tag{76}$$
$$- \text{Higher Order Terms (H.O.T)}$$

$$g\left(x_c + \delta x_c, y_c + \delta y_c, z_c + \delta z_c\right) = g\left(x_c, y_c, z_c\right) - \left(g_x \delta x_c + g_y \delta y_c + g_z \delta z_c\right)\Big|_{x_c} \tag{77}$$
$$+ H.O.T = 0$$

For $g\left(x_c, y_c, z_c\right) = 0$ and $\delta x_c \ll 1$, $\delta y_c \ll 1$, $\delta z_c \ll 1 \rightarrow H.O.T \approx 0$

$$\tag{78}$$

then $\left(g_x \delta x_c + g_y \delta y_c + g_z \delta z_c\right)\Big|_{x_c} = 0 \rightarrow \nabla g\left(x_c, y_c, z_c\right) \cdot \left(\delta x_c, \delta y_c, \delta z_c\right) = 0$

The dot product of the gradient and incremental vectors identically equals zero, indicating the two vectors are orthogonal to each other. Comparison of the velocity

61

expression given by Eq (74) with the final gradient expression of Eq (78), clearly shows two different vectors orthogonal to a common incremental vector, indicating the gradient and velocity vectors are coplanar to each other. This condition is true for all admissible incremental vectors. If the incremental variations δx_c, δy_c, and δz_c are once again assumed to be very small and the reflecting surface is assumed to have a large radius of curvature in relation to the variations, a locally planar approximation of the surface at the critical point may be made. As such, all admissible incremental vectors satisfying Eqs (74) and (78) lie on a locally planar surface. This assumption further restricts the orientation of the velocity and gradient vectors dictating that they be collinear, the condition expressed by Eqs (79) and (80) where λ and λ_c are non-zero real numbers. As defined, vector $\hat{n}_c$ represents the unit normal vector at the critical point.

$$\left[\dot{r}_1(t_c) - \dot{r}_2(t_c)\right] = \lambda \nabla g\left(x_c, y_c, z_c\right) \tag{79}$$

$$Letting \cdot \quad \hat{n}_c = \frac{\nabla g\left(x_c, y_c, z_c\right)}{\left|\nabla g\left(x_c, y_c, z_c\right)\right|} \quad and \quad \lambda_c = \lambda \left|\nabla g\left(x_c, y_c, z_c\right)\right| \tag{80}$$

$$\dot{r}_1(t_c) - \dot{r}_2(t_c) = \lambda_c \hat{n}_c$$

The geometry illustrated in Figure 13 is next considered to establish the significance of this relationship. Using the conventions indicated, Eqs (81) thru (84)

were derived to show that the condition specified by Eq (79) is equivalent to satisfying Snell's Law of Reflection at the critical point, a necessary and expected condition when applying GO assumptions. Relationships established in Eq (81) are obtained by taking the dot product and cross product Eq (80) with $\hat{n}_c$ as indicated.
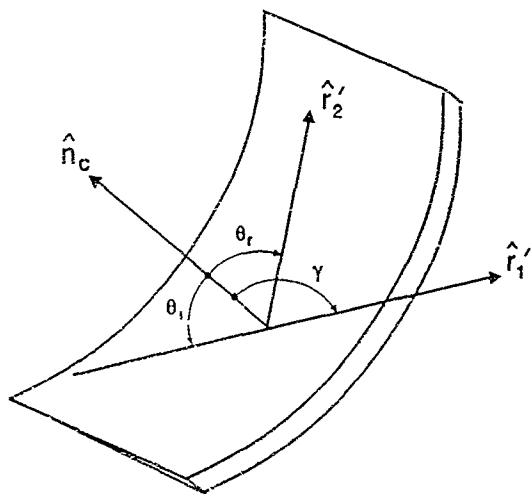
Figure 13. Geometry for Verifying Snell's Law

$$\left[\dot{r}_1(t_c) - \dot{r}_2(t_c)\right] \cdot \hat{n}_c = \dot{r}_1(t_c) \cdot \hat{n}_c - \dot{r}_2(t_c) \cdot \hat{n}_c = \lambda_c$$

$$\rightarrow \cos\gamma - \cos\theta_r = \lambda_c$$

$$\left[\dot{r}_1(t_c) - \dot{r}_2(t_c)\right] \times \hat{n}_c = \lambda_c\left(\hat{n}_c \times \hat{n}_c\right) = 0 \tag{81}$$

$$\rightarrow \sin\gamma - \sin\theta_r = 0$$

$$so \quad \gamma = \theta_r + 2k_1\pi \quad for \quad k_1 = 0, \pm1, \pm2, \ldots$$

$$or \quad \gamma = k_2\pi - \theta_r \quad for \quad k_2 = \pm1, \pm3, \pm5, \ldots$$

$$For \quad \gamma = \theta_r + 2k_1\pi \cdot \cos\gamma - \cos\theta_r = \cos(\theta_r + 2k_1\pi) - \cos\theta_r = \lambda_c$$

$$\rightarrow \lambda_c = 0 \quad \text{"Trivial Solution"} \tag{82}$$

$$For \quad \gamma = k_2\pi - \theta_r : \cos\gamma - \cos\theta_r = \cos(k_2\pi - \theta_r) - \cos\theta_r = \lambda_c$$

$$\rightarrow -2\cos\theta_r = \lambda_c \quad \rightarrow \quad \lambda = \frac{-2\cos\theta_r}{\left|\nabla g\left(x_c, y_c, z_c\right)\right|} \tag{83}$$

$$\text{"Non-Trivial Solutions Exist!"}$$

$$From \quad Figure \; 13 : \quad \theta_i = \pi - \gamma = \pi - \left(k_2\pi - \theta_r\right)$$

$$\rightarrow \theta_i = \theta_r \quad \text{"Snell's Law of Reflection"} \tag{84}$$

64

For Case II all variation about the critical point is assumed to be zero, i.e., $\delta x_c = \delta y_c = \delta z_c = 0$, and a derivation procedure similar to the one applied to the first case is carried out. A simplified variation expression for Case II is obtained from Eq (71) and may be expressed as given by Eq (85). As before, the vector notation/convention established in Eq (73) is applied to obtain the final dot product expression shown in Eq (86).

$$For \quad \delta x_c = \delta y_c = \delta z_c = 0$$

$$\delta J[x,y,z] = \left(F_{2x_2}\delta x_f + F_{2y_2}\delta y_f + F_{2z_2}\delta z_f \right)\Big|_{t_f} = 0 \tag{85}$$

$$\left(F_{2x_2}, F_{2y_2}, F_{2z_2} \right)\Big|_{t_f} \cdot \left(\delta x_f, \delta y_f, \delta z_f \right) = 0 \quad \rightarrow \quad \dot{r}_2(t_f) \cdot \left(\delta x_f, \delta y_f, \delta z_f \right) = 0 \tag{86}$$

Similar to the incremental vector about the critical point, the incremental vector $(\delta x_f, \delta y_f, \delta z_f)$ graphically represents the change in position of the final point on the reference surface. Any variation of the final point must conform to the original problem statement which requires that the end point lie on the plane specified by $f(x,y,z) = 0$. Therefore, for all admissible incremental vectors about the final point, the point $(x_f + \delta x_f, y_f + \delta y_f, z_f + \delta z_f)$ must satisfy $f(x,y,z) = 0$. Eqs (87) and (88) summarize the results of enforcing this endpoint boundary condition.

65

$$\text{For} \quad f\left(x_f + \delta x_f, y_f + \delta y_f, z_f + \delta z_f\right) = 0$$

$$f\left(x_f + \delta x_f, y_f + \delta y_f, z_f + \delta z_f\right) = f\left(x_f, y_f, z_f\right) + \left(f_x \delta x_f + f_y \delta y_f + f_z \delta z_f\right)\Big|_{t_f} \tag{87}$$

$$+ \; H.O.T = 0$$

$$\text{For} \; f\left(x_f, y_f, z_f\right) = 0 \; , \; \delta x_f << 1 \; , \; \delta y_f << 1 \; , \; \delta z_f << 1 \quad \rightarrow \quad H.O.T. \approx 0 \tag{88}$$

$$\text{then} \; \left(f_x \delta x_f + f_y \delta y_f + f_z \delta z_f\right)\Big|_{t_f} = 0 \quad \rightarrow \quad \nabla^c\left(x_f, y_f, z_f\right) \cdot \left(\delta x_f, \delta y_f, \delta z_f\right) = 0$$

Evaluation of f(x,y,z) at a variable end point is accomplished by once again using an incremental form of Taylor's series expansion, resulting in the final simplified dct product expression given in Eq (88). This expression clearly shows an orthogonal relationship between the incremental vector and gradient vector $\nabla f(x,y,z)$ at the final time. Since the incremental vector $(\delta x_f, \delta y_f, \delta z_f)$ is orthogonal to both the velocity and gradient vectors at the final time, evident by comparing Eq (86) with Eq (88), and all admissible incremental vectors must be on the pianar reference surface, the incremental and gradient vectors themselves must be collinear. This relationship is expressed in Eq (89) where two additional factors have been taken into consideration. First, the form of candidate solutions is a set of linear functions given by Eq (66) which result from considering a homogeneous medium. As such, the velocity vector remains constant over time. Second the reference plane $f(x,y,z) = 0$ is characterized by the problem statement as having a surface normal of $\hat{k}$, i.e.,

$\nabla f(x,y,z) = \hat{k}$ for all (x,y,z) on the surface. Applying these conditions, the relationship established in Eq (89) is significant in that it clearly satisfies the requirements of the original problem statement.

$$\text{For } \dot{r}_2(t) = \text{constant } \forall t \in [t_c, t_f] \quad \text{and} \quad \nabla f(x_f, y_f, z_f) = \hat{k} \qquad (89)$$

$$\text{then } \dot{r}_2(t_f) = \lambda \nabla f(x_f, y_f, z_f) \quad \rightarrow \quad \dot{r}_2(t_c) = \hat{k} = (k_x, k_y, k_z)$$

At this point the necessary conditions and relationships have been established for minimizing $J(x,y,z)$ and are summarized as follows. 1) the assumption of a homogeneous medium in both regions of integration establishes that only functions of the form expressed by Eq (66) are admissible, 2) requiring continuous solutions at $t = t_c$ for all admissible variation about the critical point, while satisfying the surface constraint that $g(x_c, y_c, z_c) = 0$, results in a relationship satisfying Snell's Law of Reflection and is expressed as given by Eq (79), 3) a homogeneous medium over the second region of integration and a constraint that the final point lie on a planar reference surface specified by $f(x,y,z) = 0$ with surface normal vector $\hat{k}$, results in the constant velocity relationship shown in Eq (89), satisfying the velocity condition/reflection direction requirement at $t = t_c$, and 4) specifying the initial point (x_i, y_i, z_i) results in a fixed end point condition at $t = t_i$, eliminating three unknowns from candidate function solutions. Beginning with candidate solutions of the form given by Eq (66), each of the above mentioned conditions and relationships are applied to obtain a specific solution for the problem. Using candidate functions of

67

the form given by Eq (66) the fixed end point boundary condition at $t = t_i$ is first applied to readily eliminate three unknowns. Eq (90) summarizes the results of applying the fixed end point boundary condition where the initial time t_i is arbitrarily set equal to zero for convenience purposes.

$$
\begin{aligned}
x_1(t_i) &= at_i + a_o \\
y_1(t_i) &= bt_i + b_c \\
z_1(t_i) &= ct_i + c_o
\end{aligned}\bigg|_{t_i = 0}
\rightarrow
\begin{aligned}
x_1(0) &= x_r = a_o \\
y_1(0) &= y_r = b_o \\
z_1(0) &= z_r = c_o
\end{aligned}
\rightarrow
\begin{aligned}
x_1(t) &= at + x_r \\
y_1(t) &= bt + y_r \\
z_1(t) &= ct + z_r
\end{aligned}
\qquad (90)
$$

The vector notation established in Eq (73) is next applied to the candidate functions, resulting the unit vector velocity equations of Eq (91). The quantity v_m is introduced as the positional velocity in the "*medium*" and is a result of assuming that $v_1 = v_2$, i.e., the positional velocity over both regions of integration are identical. These results are applied to Eqs (79) and (89) where three unknowns are determined from Eq (89) and substituted into Eq (79), resulting in the system of equations given in Eq (93).

$$
\dot{\vec{r}}_1(t) = \frac{(a,b,c)}{\sqrt{a^2 + b^2 + c^2}} = \frac{(a,b,c)}{v_m} \quad for \quad t \in \left[t_i, t_c\right]
$$

$$
\dot{\vec{r}}_2(t) = \frac{(A,B,C)}{\sqrt{A^2 + B^2 + C^2}} = \frac{(A,B,C)}{v_m} \quad for \quad t \in \left[t_c, t_f\right]
\qquad (91)
$$

$$
where: \quad v_m = \sqrt{a^2 + b^2 + c^2} = \sqrt{A^2 + B^2 + C^2}
$$

$$For \quad \dot{r}_2(t_c) = \hat{k}$$

$$\dot{r}_2(t_c) = \frac{(A,B,C)}{v_m} = \left(k_x, k_y, k_z\right) \quad \rightarrow \quad A = v_m k_x \,,\, B = v_m k_y \,,\, C = v_m k_z \tag{92}$$

$$For \quad \dot{r}_1(t_c) - \dot{r}_2(t_c) = \lambda \nabla g\left(x_c, y_c, z_c\right)$$

$$\frac{a}{v_m} - k_x = \lambda g_x\left(x_c, y_c, z_c\right)$$

$$\frac{b}{v_m} - k_y = \lambda g_y\left(x_c, y_c, z_c\right) \tag{93}$$

$$\frac{c}{v_m} - k_z = \lambda g_z\left(x_c, y_c, z_c\right)$$

When combined with an arbitrary reflection surface equation, the v_m expression of Eq (91) and velocity equations of Eq (93) represent a system of five equations and five unknowns, namely, a, b, c, λ, and t_c. They are valid under the two previously stated assumptions, homogeneous and identical mediums over both regions of integration, and apply to any arbitrary reflecting surface satisfying $g(x,y,z) = 0$ which is differentiable with respect to all variables.

4.3 Tangent Ogive Solution

A tangent ogive surface satisfies the stated requirements and is introduced as the reflecting surface of the radome. The expression given in Eq (94) represents a tangent ogive which has its base plane in the x-y plane and its tip on the positive

69

z-axis. The surface is completely described by its generating radius R and base diameter W. The equation is valid for $0 \leq z \leq L$ where L is the radome length as measured along the z-axis.

$$\textit{For a Tangent Ogive Surface,}$$

$$g(x,y,z) = \sqrt{R^2 - z^2} - \sqrt{x^2 + y^2} + \frac{W}{2} - R = 0$$

$$\textit{where} \quad 0 \leq z \leq L \quad \textit{for} \quad L = \sqrt{R^2 - (R - W/2)^2} \tag{94}$$

$$\rightarrow \quad g_x\Big|_{t_c} = \frac{-x_c}{\sqrt{x_c^2 + y_c^2}} \quad , \quad g_y\Big|_{t_c} = \frac{-y_c}{\sqrt{x_c^2 + y_c^2}} \quad , \quad g_z\Big|_{t_c} = \frac{-z_c}{\sqrt{R^2 - z_c^2}}$$

The first step in solving the system of equations for the tangent ogive is to scale/nondimensionalize all quantities involved. All lengths are scaled/divided by generating radius R, velocities are scaled by v_m, and time is scaled by R/v_m. As indicated in Eqs (95) thru (99) a tilde (~) is used to represent dimensionless quantities.

$$\textit{Letting:} \quad \tilde{x}(\tilde{t}) = \frac{x\left(\dfrac{v_m t}{R}\right)}{R} \quad , \quad \tilde{y}(\tilde{t}) = \frac{y\left(\dfrac{v_m t}{R}\right)}{R} \quad , \quad \tilde{z}(\tilde{t}) = \frac{z\left(\dfrac{v_m t}{R}\right)}{R} \tag{95}$$

$$\textit{and} \quad \tilde{a} = \frac{a}{v_m} \quad , \quad \tilde{b} = \frac{b}{v_m} \quad , \quad \tilde{c} = \frac{c}{v_m} \quad , \quad \tilde{t} = \frac{v_m t}{R}$$

70

$$\tilde{x}_1(\tilde{t}) = \left(\frac{a}{v_m}\right)\left(\frac{v_m t}{R}\right) + \frac{x_r}{R} = \tilde{a}\tilde{t} + \tilde{x}_r$$

$$\tilde{y}_1(\tilde{t}) = \left(\frac{b}{v_m}\right)\left(\frac{v_m t}{R}\right) - \frac{y_r}{R} = \tilde{b}\tilde{t} + \tilde{y}_r \tag{96}$$

$$\tilde{z}_1(\tilde{t}) = \left(\frac{c}{v_m}\right)\left(\frac{v_m t}{R}\right) + \frac{z_r}{R} = \tilde{c}\tilde{t} + \tilde{z}_r$$

$\quad v_m = \sqrt{a^2 + b^2 + c^2} \quad \rightarrow \quad \tilde{a}^2 + \tilde{b}^2 + \tilde{c}^2 = 1 \tag{97}$

Normalizing the Surface Equation:

$$\frac{g(x,y,z)}{R} = 0 \quad \rightarrow \quad \sqrt{1 - \tilde{z}^2} - \sqrt{\tilde{x}^2 + \tilde{y}^2} + \tilde{K} = 0 \quad where \quad \tilde{K} = \frac{W}{2R} - 1 \tag{98}$$

$$\rightarrow \quad \tilde{g}_{\tilde{x}}\Big|_{\tilde{c}} = \frac{-\tilde{x}_c}{\sqrt{\tilde{x}_c^2 + \tilde{y}_c^2}} \quad , \quad \tilde{g}_{\tilde{y}}\Big|_{\tilde{c}} = \frac{-\tilde{y}_c}{\sqrt{\tilde{x}_c^2 + \tilde{y}_c^2}} \quad , \quad \tilde{g}_{\tilde{z}}\Big|_{\tilde{c}} = \frac{-\tilde{z}_c}{\sqrt{1 - \tilde{z}_c^2}}$$

$$\left(\tilde{a} - \tilde{k}_x\right) = \lambda\, \tilde{g}_{\tilde{x}}\left(\tilde{x}_c, \tilde{y}_c, \tilde{z}_c\right)$$

$$\left(\tilde{b} - \tilde{k}_y\right) = \lambda\, \tilde{g}_{\tilde{y}}\left(\tilde{x}_c, \tilde{y}_c, \tilde{z}_c\right) \tag{99}$$

$$\left(\tilde{c} - \tilde{k}_z\right) = \lambda\, \tilde{g}_{\tilde{z}}\left(\tilde{x}_c, \tilde{y}_c, \tilde{z}_c\right)$$

The observation is now made the by introducing a spherical coordinate change of variables as given by Eq (100), Eq (97) is satisfied for all α and β over the specified ranges. The original system of equations is now reduced to four equations, shown in Eqs (98) and (99), and four unknowns, namely, α, β, λ, and $\bar{\tau}_c$.

$$\bar{a} = \sin\alpha \cos\beta \quad , \quad \bar{b} = \sin\alpha \sin\beta \quad , \quad \bar{c} = \cos\alpha$$
$$where \quad 0 < \beta < 2\pi \quad and \quad 0 < \alpha < \frac{\pi}{2} \tag{100}$$

Further simplifications are possible by considering a couple of additional constraints on the reflected rays. First, only reflected rays with positive k_z components are of interest. This results from restricting the antenna scan/observation region to angles which look "through" the radome. Second, only reflected rays with reflection angles greater than zero or less than $\pi/2$ Rads, as measured from the surface normal at the critical point, are considered. As a result of this restriction Eq (83) can be used to verify that λ must be less than zero. Third, as z_c approaches L, both x_c and y_c approach zero. As a result, the partial derivatives of $g(x,y,z)$ with respect to x and y fail to exist at $(0,0,L)$ and two expressions of Eq (99) become invalid and an insufficient number of equations remain to solve the problem. Therefore, z_c cannot equal L and care must be taken as z_c approaches L. Given $k_z > 0$, $\lambda < 0$, and $0 \le z_c < L$, the last expression of Eq (99) can be used to verify that $\bar{c}$ must be greater than zero, resulting in the restricted range of α values shown in Eq (100).

72

Since the scaled surface expression of Eq (98) is independent of λ, λ may be eliminated using Eq (99) provided care is taken to ensure that the partial derivatives exist and are non-zero. In eliminating λ three special cases are considered. Each case is distinguishable from the others by the relationship between the values of $\tilde{x}_c$ and $\tilde{y}_c$. For each case considered the goal is to begin with Eqs (98) and (99) and eliminate as many unknowns as possible, preferably obtaining closed-form solutions for all variables. Each of the three special cases is further divided in to subcases based on radome geometry and aperture scan angle restrictions. A total of eleven special cases and/or subcases exist. The following development is provided for the case which yields a majority of critical point solutions. Complete solution details for additional cases and subcases thereof are provided in *Appendix A*.

For the first case, Case I, both $\tilde{x}_c$ and $\tilde{y}_c$ are assumed to be non-zero. As a result, the partial derivative expressions of Eq (98) are substituted into Eq (99) to eliminate λ as shown in Eq (101). By equating the first two expressions of Eq (101) and applying the change of variables presented in Eq (100), the process of deriving an expression for $\tilde{\tau}_c$ is accomplished as shown in Eq (102). At this point two subcases are required. Case I.A is considered here and Case I.B derivation procedures are provided in *Appendix A*. Case I.A assumes that $\tilde{\tau}_c$ can be explicitly solved for from Eq (102) resulting in the expression as shown in Eq (103). This $\tilde{\tau}_c$ expression and the change of variables given by Eq (100) are substituted into Eq (96) to obtain the critical point coordinate expressions given by Eqs (104) thru (106). With both λ and $\tilde{\tau}_c$ eliminated, a system of two equations with two unknowns remains, namely α and β

73

For Case I, $\tilde{x}_c \neq 0$ *and* $\tilde{y}_c \neq 0$

$$\lambda = \frac{\left(\tilde{a} - k_x\right)\sqrt{\tilde{x}_c^2 + \tilde{y}_c^2}}{\tilde{x}_c} = \frac{\left(\tilde{b} - k_y\right)\sqrt{\tilde{x}_c^2 + \tilde{y}_c^2}}{\tilde{y}_c} = \frac{\left(\tilde{c} - k_z\right)\sqrt{1 - \tilde{z}_c^2}}{z_c} \tag{101}$$

$$\frac{\tilde{a} - k_x}{\tilde{x}_c} = \frac{\tilde{b} - k_y}{\tilde{y}_c} \quad \rightarrow \quad \left(\tilde{a} - k_x\right)\tilde{y}_c = \left(\tilde{b} - k_y\right)\tilde{x}_c$$

where $\quad \tilde{x}\left(\tilde{t}_c\right) = \tilde{a}\tilde{t}_c + \tilde{x}_r \quad and \quad \tilde{y}\left(\tilde{t}_c\right) = \tilde{b}\tilde{t}_c + \tilde{y}_r$ $\tag{102}$

$$\rightarrow \tilde{t}_c \sin\alpha\left(k_y\cos\beta - k_x\sin\beta\right) = \tilde{x}_r\left(\sin\alpha\cos\beta - k_y\right) - \tilde{y}_r\left(\sin\alpha\cos\beta - k_x\right)$$

For Case I.A : $\sin\alpha\left(k_y\cos\beta - k_x\sin\beta\right) \neq 0$

$$\tilde{t}_c = \frac{\tilde{x}_r\left(\sin\alpha\sin\beta - k_y\right) - \tilde{y}_r\left(\sin\alpha\cos\beta - k_x\right)}{\sin\alpha\left(k_y\cos\beta - k_x\sin\beta\right)} \tag{103}$$

$$\tilde{x}_c = \frac{\cos\beta\left[\tilde{x}_r\left(\sin\alpha\sin\beta - k_y\right) - \tilde{y}_r\left(\sin\alpha\cos\beta - k_x\right)\right]}{\left(k_y\cos\beta - k_x\sin\beta\right)} + \tilde{x}_r \tag{104}$$

$$\tilde{y}_c = \frac{\sin\beta\left[\tilde{x}_r\left(\sin\alpha\sin\beta - k_y\right) - \tilde{y}_r\left(\sin\alpha\cos\beta - k_x\right)\right]}{\left(k_y\cos\beta - k_x\sin\beta\right)} + \tilde{y}_r \tag{105}$$

$$\tilde{z}_c = \frac{\cot\alpha\left[\tilde{x}_r\left(\sin\alpha\sin\beta - k_y\right) - \tilde{y}_r\left(\sin\alpha\cos\beta - k_x\right)\right]}{\left(k_y\cos\beta - k_x\sin\beta\right)} + \tilde{z}_r \tag{106}$$

74

One equation used to solve for α and β is formed by substituting the coordinate expressions of Eqs (104) thru (106) into the scaled surface expression of Eq (98). The second equation is formed by equating the right-hand expression of Eq (101) with either of the other two expressions, as shown in Eqs (107) and (108), with $\tilde{x}_c$, $\tilde{y}_c$, and $\tilde{z}_c$ replaced by Eqs (104) thru (106), respectively. In choosing which of the two expressions to use consideration should be given to the limiting cases as either $\tilde{x}_c$ or $\tilde{y}_c$ approach zero. Note that the final expressions to be solved are non-linear transcendental type equations with no explicit solution possible. Therefore, numerical solution techniques must be implemented to solve for remaining unknowns.

$$\frac{\left(\tilde{a} - k_x\right)\sqrt{\tilde{x}_c^2 + \tilde{y}_c^2}}{\tilde{x}_c} = \frac{\left(\tilde{c} - k_z\right)\sqrt{1 - \tilde{z}_c^2}}{\tilde{z}_c} \qquad (107)$$

$$\frac{\left(\tilde{b} - k_y\right)\sqrt{\tilde{x}_c^2 + \tilde{y}_c^2}}{\tilde{y}_c} = \frac{\left(\tilde{c} - k_z\right)\sqrt{1 - \tilde{z}_c^2}}{\tilde{z}_c} \qquad (108)$$

V. Propagation Technique

5.1 Introduction

When an Electromagnetic (EM) wave travels from a source and arrives at a distant observation point, the medium through which it propagates will generally introduce amplitude, phase, and polarization variations. As stated in the *Background* section, all three variations are expected to occur as an EM wave propagates through a radome. *Surface Integration*" and "*Ray-Tracing*" techniques can be used to account for the variations. This research effort capitalized on existing propagation analysis and modeling techniques which were modified and extended to achieve specific research goals. In selecting a wave propagation technique two key factors had to be taken into consideration. First the propagation technique chosen for analysis and modeling had to provide flexibility, i.e., the technique had to allow for key system parameter variations while providing a response which was both realistic and technically sound. Second, responses to such variations had to occur in a timely manner, i.e., consideration had to be given to minimizing computational intensity while providing accurate results. In conjunction with the desire to limit propagation technique development, consideration of these key factors led to selection of the "*Ray-Tracing* (Geometric Optics) propagation technique for analysis and modeling purposes.

A parametric investigation of radome analysis methods [2] developed a general theory for radome analysis. The investigation determined relative accuracies and ranges of validity for three computer aided analysis methods - surface integration

76

ray-trace receive, and ray-trace transmit. The study concluded that the ray-trace receive method was the "most attractive" because of fast computation time and reasonably accurate results. Following this effort, Kozakoff [5] conducted an improved radome analysis methodology study which incorporated reflected E-Field contributions in the ray-trace receive analysis, achieving 'reasonably good" computational accuracy for most applications where antenna/radome dimensions exceeded 5 wavelengths. The ray-trace receive technique was later pursued by Klemer [6] who characterized BSE sensitivity behavior using multiple radome designs (various wall thicknesses and dielectric properties) and aperture characteristics (size element type, amplitude taper, etc.), establishing a 'consensus that the ray-trace receive formulation offers the best compromise between accuracy and computational effort for moderate to large-sized radomes, i.e., radomes with dimensions greater than ten wavelengths," typically the case for most aircraft radomes. Also, radomes of this type are generally characterized by *"fineness"* ratios, a ratio of radome length to radome base width, in the range of two to three. These two limitations ensure that *"locally-pla..ar"* conditions are met at typical radar frequencies

Considering an end goal of the research effort was to analyze and model monopulse radar tracking performance, the ray-trace receive propagation technique proved to be very useful. Monopulse tracking performance is typically characterized through BSE measurement procedures conducted on radar test ranges A typical test procedure for characterizing tracking performance begins by scanning the radar aperture, either electronically or mechanically, in a specified direction. This direction is designated as the system "tracking/pointing" direction The location of a far field

77

source is varied about the fixed "tracking" direction in a predetermined scan pattern until the monopulse error signal goes to zero, indicating the energy received by the aperture is arriving from a direction coinciding with the system "tracking" direction. The final source location causing this condition is designated as the "actual" source location. Optical instrumentation test data, obtained from sources/sensors located on the aperture and source, is used to calculate the angular difference between the radar "tracking" direction and "actual" source location. This difference represents the "system" BSE in the specified 'tracking" direction. This process is easily duplicated for analysis and modeling purposes using the ray-trace receive propagation technique.

The ray-trace receive propagation technique is applied to both 'direct" and "primary reflected" rays. As previously defined, *primary reflected*" rays are rays which experience at most one reflection prior to intercepting the aperture plane. Both direct and reflected rays experience the effects of propagation through the radome wall, i.e., amplitude, phase, and polarization distortion upon transmission. All "primary reflected" rays experience additional distortion upon reflecting from the inner radome surface. At each ray-radome intersection point, regardless which type of ray is being considered, a "locally-planar" approximation is made and a plane of incidence' is established. The 'locally-planar' condition is required for calculating complex transmission and reflection coefficient approximations. A plane used along with the established plane of incidence. These approximations determine characterize the effects the radome structure has upon the ray.

5.2 Local Plane of Incidence

The local *"plane of incidence"* is defined in the following manner. Given a point on a surface with normal vector $\hat{n}$ and an incident E-Field at that point propagating in direction $\hat{k}$, the *"plane of incidence"* is the plane containing both $\hat{n}$ and $\hat{k}$. The specific unit vector pair chosen for E-Field decomposition is dependent on particular analysis and modeling objectives, varying according to the propagation technique implemented

The definitions stated in Eqs (109) thru (111) and depicted in Figure 14 are the orthogonal unit vector pairs chosen to define the *"plane of incidence"* and the corresponding transmission and reflection unit vectors These particular vector pair combinations were primarily chosen for compatibility purposes. As developed by Munk [20] and later used in development of the PMM code [11], these definitions were arbitrarily chosen such that the reflection coefficient for the E-Field equals minus one for the case when the dielectric boundary is a perfect conductor These definitions and conventions are used throughout the remainder of the dissertation.

For the inciden

$$ \mu_{\perp} \quad \frac{}{} \quad u_{\perp} = k_{\perp} \times r \qquad 109 $$

For the transmitted ray,

$$\hat{u}_\perp^t = \frac{\hat{n} \times \hat{k}_t}{|\hat{n} \times \hat{k}_t|} \;\; ; \;\; \hat{u}_\parallel^t = \hat{u}_\perp^t \times \hat{k}_t \tag{110}$$

For the reflected ray,

$$\hat{u}_\perp^r = \frac{\hat{n} \times \hat{k}_r}{|\hat{n} \times \hat{k}_r|} \;\; ; \;\; \hat{u}_\parallel^r = - \hat{u}_\perp^r \times \hat{k}_r \tag{111}$$
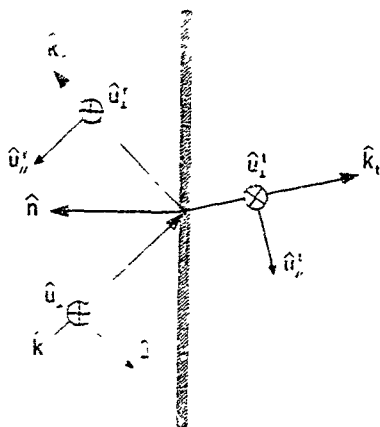

Figure 14 Plane of Incidence Unit Vectors

80
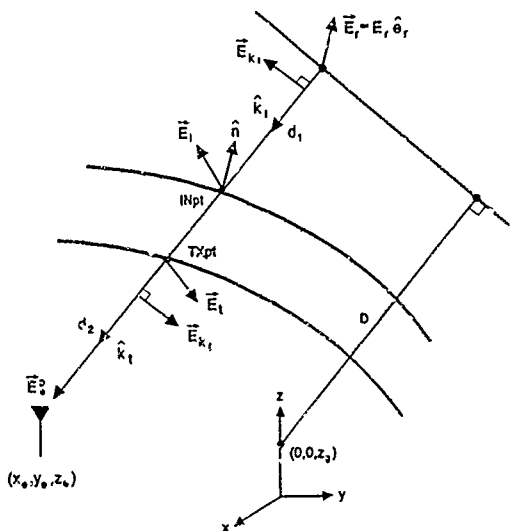
Figure 15. Direct Ray Incident E-Field Geometry

5 3 Direct Ray Propagation Path

The geometry established in Figure 15 is used in analyzing the propagation effects along a direct ray path For the geometry shown, the following definitions apply:

$\vec{E}_e^D$ = Incident E-Field on the element due to a direct path

$\vec{E}_r$ = Reference E-Field representing a uniform plane wave.

$\hat{e}_r$ = Complex unit polarization vector of reference E-Field.

$\vec{E}_r$ = Component of $\vec{E}_r$ responsible for propagation in $\hat{k}$ direction.

$\vec{E}_i$ = Incident E-Field on outer radome surface

$\vec{E}_t$ = Transmit E-Field on inner dome surface

INpt = Incident/outer surface ... point

TXpt = Transmit/inner surface transmit point.

$\hat{k}_i$ = Incident E-Field propagation direction

$\hat{k}_t$ = Transmit E-Field propagation ...

d_1 = Propagation path length from reference ... direct path ... point ... the outer radome surface.

d_2 = Propagation path length from ... inner radome surface to arbitrary aperture element coordinates

Given an arbitrary aperture element located ... rectangular coordinate ... and a reference E-Field located a distance D from the aperture ... point ... the incident E-Field $\vec{E}_e^D$ incident on the element due to propagation along a direct path needs to be determined. The final expression developed for $\vec{E}^D$ must account for two important analysis and modeling characteristics. First, because phase information is known to adversely affect monopulse tracking performance, all phase delays along the direct propagation path must be accurately accounted for. Second, since analysis involving arbitrarily polarized reference E-Field is desired, all final expressions must be general in nature reflecting a dependance on reference field polarization states.

The following equations summarize the results of using the ray-trace receive propagation technique to arrive at the final $\vec{E}_e^t$ expression. The vector component of $\vec{E}_r$ responsible for propagation in direction $\hat{k}$, first determined in accordance with Eq (112) and propagated to the outer radome surface to establish the incident

82

E-field $\vec{E}_r$, as shown in Eqs (113) and (114) a free-space phase delay corresponding distance d_1 been added to account for the propagation phase delay. The quantity the free-space phase constant and is equivalent to 2π divided by the free-space wavelength λ_o ($K_o = 2\pi/\lambda_o$).

$$\text{Given} \quad \vec{E}_r = E_r \hat{e}_r, \quad \text{then} \quad \vec{E}_{k_i} = E_r \left\{ \hat{e}_r - \left(\hat{e}_r \cdot \hat{k}_i \right) \hat{k}_i \right\} \tag{112}$$

$$\vec{E}_i = \vec{E}_{k_i} e^{-jK_o d_1} = E_r e^{-jK_o d_1} \left\{ \hat{e}_r - \left(\hat{e}_r \cdot \hat{k}_i \right) \hat{k}_i \right\} \tag{113}$$

$$\text{Defining} \quad E_i = E_r e^{-jK_o d_1} \quad \text{and} \quad \hat{e}_i = \hat{e}_r - \left(\hat{e}_r \cdot \hat{k}_i \right) \hat{k}_i$$
$$\rightarrow \vec{E}_i = E_i \hat{e}_i \tag{114}$$

Decomposing $\vec{E}_i$ into parallel ($\parallel$) and perpendicular ($\perp$) components as established by the local plane of incidence,

$$\vec{E}_i^{\parallel} = E_i \left(\hat{e}_i \cdot \hat{u}_{\parallel}^i \right) \hat{u}_{\parallel}^i = E_i^{\parallel} \hat{u}_{\parallel}^i \quad , \quad \vec{E}_i^\perp = E_i \left(\hat{e}_i \cdot \hat{u}_\perp^i \right) \hat{u}_\perp^i = E_i^\perp \hat{u}_\perp^i \tag{115}$$

Propagating parallel and perpendicular components through the radome and weighting the components by planar transmissivity approximations results in the expression given by Eq (116).

83

$$\vec{E}_t \times \vec{E}_t^{\parallel} + \vec{E}_t^{\perp} = T_{\parallel} E_t^{\parallel} \hat{u}_{\parallel}^t + T_{\perp} E_t^{\perp} \hat{u}_{\perp}^t$$

$$= E_{\cdot} \left\{ T_{\parallel} \left(\vec{e}_t \cdot \hat{u}_{\parallel}^t \right) \hat{u}_{\parallel}^t + T_{\perp} \left(\vec{e}_t \cdot \hat{u}_{\perp}^t \right) \hat{u}_{\perp}^t \right\} \qquad (116)$$

$$= E_t \vec{e}_t$$

Calculating the portion of $\vec{E}_t$ responsible for propagation in direction $\hat{k}_t$ and utilizing the definitions for the transmit ray plane of incidence unit vectors the following relationships hold. The propagating E-Field component is seen to be equivalent to $\vec{E}_t$ as shown in Eq (119).

$$\vec{E}_{k_t} = \vec{E}_t - \left(\vec{E}_t \cdot \hat{k}_t \right) \hat{k}_t = E_t \left\{ \vec{e}_t - \left(\vec{e}_t \cdot \hat{k}_t \right) \hat{k}_t \right\} \qquad (117)$$

$$\hat{u}_{\perp}^t \cdot \hat{k}_t = \frac{\hat{n} \times \hat{k}_t}{\left| \hat{n} \times \hat{k}_t \right|} \cdot \hat{k}_t = 0 \quad , \quad \hat{u}_{\parallel}^t \cdot \hat{k}_t = \left(\hat{u}_{\perp}^t \times \hat{k}_t \right) \cdot \hat{k}_t = 0 \qquad (118)$$

$$\vec{e}_t \cdot \hat{k}_t = \left\{ T_{\parallel} \left(\vec{e}_t \cdot \hat{u}_{\parallel}^t \right) \hat{u}_{\parallel}^t + T_{\perp} \left(\vec{e}_t \cdot \hat{u}_{\perp}^t \right) \hat{u}_{\perp}^t \right\} \cdot \hat{k}_t = 0 \quad \rightarrow \quad \vec{E}_{k_t} = \vec{E}_t \qquad (119)$$

The transmitted E-Field $\vec{E}_t$ is next propagated to the aperture element location as summarized in Eqs (120) thru (123) where the final expression for $\vec{E}_e^D$ is as given by Eq (123). The final expressions for both Eqs (121) and (122) are obtained by noting the the dot product of $\hat{k}_t$ with both incident plane unit vectors, parallel and perpendicular, identically equals to zero.

84

$$\vec{E}_e^D = \vec{E}_t e^{-jK_o d_2}$$

$$= \vec{E}_t e^{-jK_o(d_2 + d_i \sin\theta_i)} \left\{ T_\parallel \left(\vec{e}_i \cdot \hat{u}_\parallel^t \right) \hat{u}_\parallel^t + T_\perp \left(\vec{e}_i \cdot \hat{u}_\perp^t \right) \hat{u}_\perp^t \right\} \qquad (120)$$

$$\vec{e}_i \cdot \hat{u}_\parallel^t = \left\{ \hat{e}_r - \left(\hat{e}_r \cdot \hat{k}_i \right) \hat{k}_i \right\} \cdot \hat{u}_\parallel^t = \hat{e}_r \cdot \hat{u}_\parallel^t - \left(\hat{e}_r \cdot \hat{k}_i \right) \left(\hat{k}_i \cdot \hat{u}_\parallel^t \right)$$

$$= \hat{e}_r \cdot \hat{u}_\parallel^t \qquad (121)$$

$$\vec{e}_i \cdot \hat{u}_\perp^t = \left\{ \hat{e}_r - \left(\hat{e}_r \cdot \hat{k}_i \right) \hat{k}_i \right\} \cdot \hat{u}_\perp^t = \hat{e}_r \cdot \hat{u}_\perp^t - \left(\hat{e}_r \cdot \hat{k}_i \right) \left(\hat{k}_i \cdot \hat{u}_\perp^t \right)$$

$$= \hat{e}_r \cdot \hat{u}_\perp^t \qquad (122)$$

$$\vec{E}_e^D = E_e^D \, \vec{e}_e^D \quad where \quad \begin{cases} E_e^D = E_r e^{-jK_o(d_1 + d_2 + d_i \sin\theta_i)} \\[2ex] \vec{e}_e^D = T_\parallel \left(\hat{e}_r \cdot \hat{u}_\parallel^t \right) \hat{u}_\parallel^t + T_\perp \left(\hat{e}_r \cdot \hat{u}_\perp^t \right) \hat{u}_\perp^t \end{cases} \qquad (123)$$

The final $\vec{E}_e^D$ expression in Eq (123) reflects the two important characteristics previously discussed, polarization dependance and accurate phase tracking. An additional $d_i \sin\theta_i$ factor not appearing in Figure 15 is included in the total phase delay term of the complex $\vec{E}_e^D$ expression. Although this additional phase delay factor

is not evident in previous analysis and modeling efforts, its inclusion in this development is believed reasonable and justifiably correct since non-trivial tapers in radome thickness are considered. When considering various techniques for approximating complex planar transmission coefficients, i.e., PMM, Richmond's equations, etc., care must be taken to ensure that the phase of the calculated transmission coefficients is accurately interpreted. In most cases the calculated phase represents the total phase delay, often referred to as the "*Insertion Phase Delay*" (IPD), of the planar phase front as measured along the surface normal direction. Referring to Figure 16, this delay corresponds to the difference between the phase of the normal phase front phase ϕ_r and the incident phase front ϕ_i.

Given a specific set of incident (INpt) and transmit (TXpt) points as indicated in Figure 16 the actual IPD corresponds to the difference between the transmit phase front ϕ_t and incident phase front ϕ_i. As shown in Figure 16, ϕ_t can be obtained by adding an additional free-space phase delay corresponding to the distance x. Eqs (124) and (125) summarize the process for calculating ϕ_t where the following definitions are applied to the geometry established in Figure 16 :

d_n = Distance as measured along the surface normal direction.

d_p = Distance as measured along the propagation path.

d_t = Distance from normal transmit point to TXpt.

θ_i = Ray incidence angle.

86
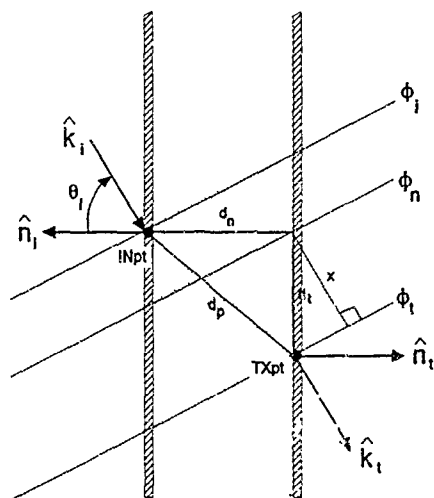
Figure 16. Additional Phase Delay Geometry

$$For \quad d_t = \sqrt{d_p^2 - d_n^2} \quad And \quad x = d_t \sin\theta_i \quad (124)$$

$$\phi_t = \phi_n - K_o d_t \sin\theta_t \quad (125)$$

5.4 Reflected Ray Propagation Path

For analyzing propagation effects along reflected ray paths the geometry established in Figure 17 is used. As with the direct ray propagation case, the E-Field $\vec{E}_c^R$ incident on the element due to a reflected ray path must be determined. Accurate phase tracking and reference E-Field polarization dependance are once

again important characteristics to be contained in the final expressions. Vector definitions/conventions for all components along the path from the reference E-Field plane to the radome reflection point RFpt are unchanged from those used in the direct ray propagation analysis.
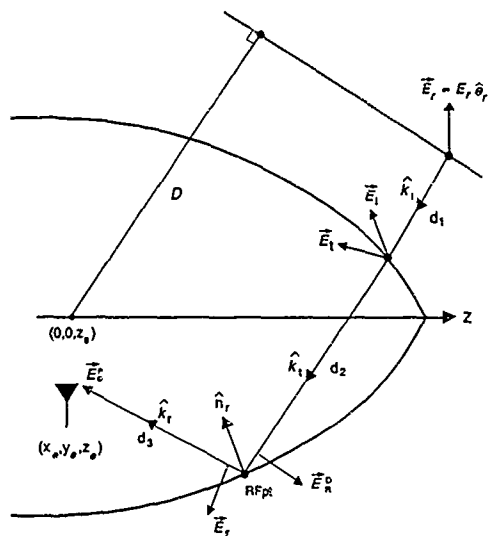

Figure 17. Reflected Ray Incident E-Field Geometry

For components not previously defined the following definitions are made as illustrated in Figure 17:

$\vec{E}_e^R$ = Incident E-Field at the element due to reflected path

$\vec{E}_R^D$ = Incident E-Field at the reflection point due to direct path.

$\vec{E}_r$ = Reflected E-Field on inner radome surface.

RFpt = Reflected/inner surface reflection point.

$\hat{k}_r$ = Reflected E-Field propagation direction.

$\hat{n}_r$ = Surface normal vector at RFpt.

Results of the direct path analysis are applied directly to Figure 17 for obtaining the incident E-Field $\vec{E}_R^D$ at RFpt. Since the aperture element location was arbitrarily chosen for the direct path development, the direct path results are applicable for any point located within the radome structure, including points not located on the aperture plane. Reflection point RFpt satisfies this condition and Eq (123) may be used to express $\vec{E}_R^D$ as shown in Eq (126)

$$\vec{E}_R^D = E_R^D \, \vec{e}_R^D \quad where \quad \begin{cases} E_R^D = E_r \, e^{-jK_o\left(d_1 + d_2 + d_i\sin\theta_i\right)} \\ \\ \vec{e}_R^D = T_{\parallel}\left(\hat{e}_r \cdot \hat{u}_{\parallel}^t\right)\hat{u}_{\parallel}^t + T_{\perp}\left(\hat{e}_r \cdot \hat{u}_{\perp}^t\right)\hat{u}_{\perp}^t \end{cases} \tag{126}$$

At the reflection point a "*locally-planar*" assumption is made and a "*plane of incidence*" established in accordance with Figure 14 definitions. Consistent with definitions given by Eqs (109) thru (111), Eqs (127) and (128) define the orthogonal unit vectors used for decomposing $\vec{E}_R^D$ at RFpt. The unit vector designations have been changed from $\hat{u}$ to $\hat{v}$ to avoid confusion between the transmission point and reflection point plane of incidence vectors.

89

$$\hat{v}'_\perp = \frac{\hat{n}_r \times \hat{k}_t}{|\hat{n}_r \times \hat{k}_t|} \quad ; \quad \hat{v}^i_\parallel = \hat{v}^i_\perp \times \hat{k}_t \tag{127}$$

$$\hat{v}^r_\perp = \frac{\hat{n}_r \times \hat{k}_r}{|\hat{n}_r \times \hat{k}_r|} \quad ; \quad \hat{v}^r_\parallel = -\hat{v}^r_\perp \times \hat{k}_r \tag{128}$$

Using these definitions the incident E-Field $\vec{E}^D_R$ is decomposed in to parallel and perpendicular components at the inner radome surface. After decomposition each component is weighted by its respective reflectivity coefficient resulting in the reflected E-Field $\vec{E}_r$ expression as given by Eq (129).

$$\vec{E}_r = \vec{E}^\parallel_r + \vec{E}^\iota_r = \Gamma_\parallel E^{D\parallel}_R \hat{v}^r_\parallel + \Gamma_\perp E^{D\perp}_R \hat{v}^r_\perp$$
$$= E^D_R \left\{ \Gamma_\parallel \left(\vec{e}^D_R \bullet \hat{v}^i_\parallel \right) \hat{v}^r_\parallel + \Gamma_\perp \left(\vec{e}^D_R \bullet \hat{v}^i_\perp \right) \hat{v}^r_\perp \right\} \tag{129}$$

The reflected E-Field $\vec{E}_r$ is then propagated to the aperture element accounting for a path length phase delay corresponding to distance d_3, resulting in the final expression for $\vec{E}^R_e$ as given Eqs (130) thru (132). The final expression for $\vec{e}^R_e$ given by Eq (132) is obtained after the dot product operations indicated in Eq (131) are carried out.

90

$$\vec{E}_e^R = \vec{E}_r e^{-jK_e d_3} = E_D^R \left\{ T_{\parallel} \left(\vec{e}_R^D \cdot \hat{v}_{\parallel}^i \right) \hat{v}_{\parallel}^r + T_{\perp} \left(\vec{e}_R^D \cdot \hat{v}_{\perp}^i \right) \hat{v}_{\perp}^r \right\} \qquad (130)$$

$$\vec{E}_e^R = E_e^R \vec{e}_e^R \quad where \quad \begin{cases} E_e^R = E_r e^{-jK_e \left(d_1 + d_2 + d_3 + d_4 \sin \theta_i \right)} \\ \\ \vec{e}_e^R = \Gamma_{\parallel} \left(\vec{e}_R^D \cdot \hat{v}_{\parallel}^i \right) \hat{v}_{\parallel}^r + \Gamma_{\perp} \left(\vec{e}_R^D \cdot \hat{v}_{\perp}^i \right) \hat{v}_{\perp}^r \end{cases} \qquad (131)$$

$$\begin{aligned} \vec{e}_e^R &= \Gamma_{\parallel} \hat{v}_{\parallel}^r \left\{ T_{\parallel} \left(\hat{e}_r \cdot \hat{u}_{\parallel}^i \right) \left(\hat{u}_{\parallel}^i \cdot \hat{v}_{\parallel}^i \right) + T_{\perp} \left(\hat{e}_r \cdot \hat{u}_{\perp}^i \right) \left(\hat{u}_{\perp}^i \cdot \hat{v}_{\parallel}^i \right) \right\} \\ &+ \Gamma_{\perp} \hat{v}_{\perp}^r \left\{ T_{\parallel} \left(\hat{e}_r \cdot \hat{u}_{\parallel}^i \right) \left(\hat{u}_{\parallel}^i \cdot \hat{v}_{\perp}^i \right) + T_{\perp} \left(\hat{e}_r \cdot \hat{u}_{\perp}^i \right) \left(\hat{u}_{\perp}^i \cdot \hat{v}_{\perp}^i \right) \right\} \end{aligned} \qquad (132)$$

5.5 Refractive Effects

Typical ray-tracing propagation techniques neglect the effects of refraction in propagating a wave through the radome structure. Such effects are generally assumed to be negligible, thereby simplifying the analysis and modeling development. The simplified analysis and modeling procedures are unable to accurately characterize the second-order effects of net ray deflection on overall boresight error [6]. The following development summarizes the process by which refractive effects are analyzed, modeled and characterized under the research effort. Refractive effects are incorporated into the propagation model at two different levels. For the first level of development refractive effects are included only within the radome structure. At

91

this level, the transmit point (TXpt) is calculated from a given incident point (INpt) and incident propagation direction $\hat{k}_i$, accounting for total refractive effects between radome layers. Locally-planar approximations are enforced such that the output propagation direction $\hat{k}_t$ remains unchanged from the input propagation direction. The second level of development accounts for "overall" refractive effects along ray propagation paths, including a transmit propagation direction $\hat{k}_t$, which differs from $\hat{k}_i$, and is dependant on radome electrical properties and geometry.

Two key factors are required to accurately account for refractive effects within the radome structure. First, refractive effects across boundaries with discontinuous electrical and magnetic properties must be accounted for. These effects are well established and are obtained through Snell's Law of Refraction. For non-conductive materials Snell's Law of Refraction can be expressed as given by Eq (133) [8].

$$\sqrt{\mu_i \epsilon_i} \sin\theta_i = \sqrt{\mu_t \epsilon_t} \sin\theta_t$$

$$\rightarrow \quad \theta_t = \sin^{-1}\left\{\sqrt{\frac{\mu_i \epsilon_i}{\mu_t \epsilon_t}} \sin\theta_i\right\}$$

(133)

In Eq (133) both the incident angle θ_i and transmit angle θ_t are measured relative to the surface normal vector at the incident point. The complex permittivity ϵ_t and complex permeability μ_t characterize the electrical and magnetic properties of the two media. Generally θ_t is a complex transmission angle which becomes purely real when lossless media are involved. For typical radome materials, dielectrics with very low loss-tangents ($\delta_t << 1$), the magnitudes of ϵ_t and μ_t are used in Eq (133) for

92

approximating the transmission angle. Other cases involving materials with appreciable loss may be handled by computing an "equivalent" real transmission angle [8].

The second key factor is that each surface of the radome structure be accurately defined. Surface equations and gradient components from the multi-layer radome development of *Chapter III* satisfy this requirement. Each layer of the radome being analyzed is uniquely defined, including a surface normal vector at any arbitrary point on a specified radome surface. With each surface specified and both INpt and $\hat{k}_i$ given, Eq (133) is repeatedly applied to the radome structure until TXpt is determined. Under locally-planar assumptions surface normal vector directions at each surface intercepted between INpt and TXpt equal the normal vector direction at INpt. Under these conditions the ray propagation direction remains unchanged in passing through the radome, i.e., $\hat{k}_i = \hat{k}_r$. Therefore, the first level of development accounts only for refraction within the radome structure and not along the entire propagation path.

The second level of development accounts for "overall" refractive effects along the propagation path Locally-planar approximations are employed only as a means for approximating transmission and reflection properties of the radome They are not used to approximate surface normal vector components along ray propagation paths Rather, normal vector components are calculated at distinct ray/surface intercept points using the multi-layer surface equations developed in *Chapter III*. Therefore, repeated application of Snell's Law of Refraction to a ray incident on the radome's outer surface results in 1) a transmit point (TXpt) on the inner surface which is

93

displaced from the transmit point resulting from a ray passing straight through the radome, and 2) a transmit propagation direction $\hat{k}_t$ which differs from the incident propagation direction $\hat{k}_n$, $\hat{k}_t$ and $\hat{k}_t$ may in fact lie in separate planes.
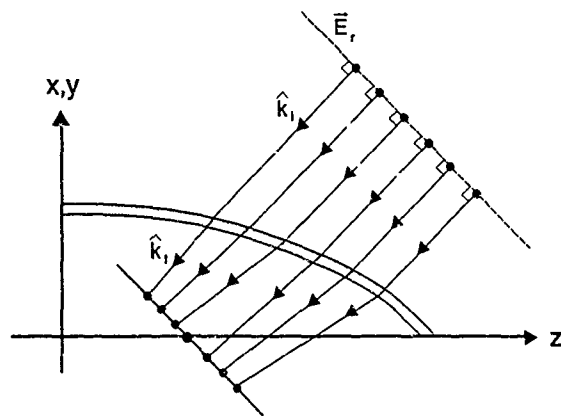

Figure 18. Uniformly Spaced Incident Rays

The geometry of Figure 18 shows how ray refractive effects are incorporated in ray-trace receive analysis. The reference E-Field $\vec{E}_r$ represents a Uniform Plane Wave (UPW) incident from a distant source. A ray is traced from the reference E-Field location in direction $\hat{k}_t$ to the incident point INpt on the radome's outer surface. Snell's Law of Refraction is repeatedly applied to the radome structure until the transmit point TXpt is established on the inner surface. At TXpt a final application of Snell's Law determines the transmit propagation direction $\hat{k}_t$. The ray is propagated from TXpt to the point where it intersects the aperture plane. This

94

process is continued for each ray emanating from the reference E-Field plane. Because refractive effects have been included, a uniformly spaced bundle of rays emanating from the reference plane intercept the aperture plane at non-uniformly spaced intercept points/element locations. This requires aperture integration to be performed on a non-uniform grid of sample points.
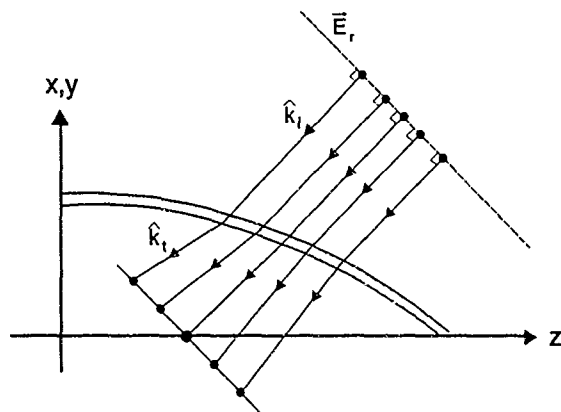
Figure 19. Non-Uniformly Spaced Incident Rays

Since aperture integration is required over uniformly spaced or known element locations, consistent with the overall system analysis and modeling approach, an alternate propagation technique must be established. Given $\vec{E}_r$ is a Uniform Plane Wave (UPW), all rays emanating from the reference plane are initially weighted by equivalent amplitude and phase terms regardless of their initial location on the plane. Figure 19 represents an equivalent method for incorporating refractive effects into

95

the overall propagation model. A non-uniformly spaced bundle of rays is propagated from the reference plane which in turn intercept the aperture plane at uniformly spaced points. By invoking reciprocity, these propagation paths are easily calculated from known aperture element coordinates. The multi-layer surface equations of *Chapter III* in conjunction with Snell's Law of Refraction facilitate the use of an iterative Newton's method for calculating the ray paths via ray transmission techniques.

For calculating INpt and TXpt by a transmit technique a specific element location and desired propagation direction $\hat{k}_i$ are given. An estimate of $-\hat{k}_i$ is determined and Newton's method is used in conjunction with the inner radome surface equation to calculate a candidate TXpt. The ray is then propagated from TXpt to INpt by repeated application of Snell's Law resulting in an estimate of $-\hat{k}_i$. This estimate is compared to $\hat{k}_i$ by a simple dot product operation to determine its relative "closeness". If not within established limits the $-\hat{k}_i$ estimate is updated and the process is repeated. This iterative procedure is continued until the calculated estimate of $-\hat{k}_i$ satisfies established equality limits. Once equality limits are satisfied the corresponding INpt and TXpt points are used for ray-trace receive calculations.

VI. Reference E-Field Development

6.1 Introduction

The Reference E-Field $\vec{E}_r$ is a key element used in analyzing and modeling the overall radome, radar, and monopulse processing "system". Accurate tracking of wavefront polarization along propagation paths is essential to analyzing and understanding depolarization effects of various system components. Specifically, radome depolarization effects must be isolated from antenna element polarization sensitivity effects. Development of the incident E-Field expressions in *Chapter V* is indicative of the level of effort required to maintain polarization "purity", i.e., no loss of generality in regard to E-Field polarization states. Reference E-Field analysis and modeling must account for two important considerations. First, location flexibility must exist, i.e., $\vec{E}_r$ must be arbitrarily located anywhere within the system's field of view. Variable $\vec{E}_r$ locations are required for aperture far field pattern generation and monopulse tracking error characterization. Second, $\vec{E}_r$ must possess arbitrary polarization states. This requirement allows for radome depolarization and system polarization sensitivity effects to be fully characterized.

6.2 Reference E-Field Location

Two separate coordinate systems are considered in developing expressions for an arbitrarily located reference E-Field. Aperture far-field radiation patterns and monopulse tracking error characteristics are generally established/characterized in a coordinate system relative to the aperture scan direction. Reference E-Field locations used for analysis and modeling must vary in accordance with this same

97

relative coordinate system. Given that an overall "system" is analyzed and modeled an absolute coordinate system is used. Therefore, final expressions for reference E-Field location are developed such that 1) they reflect a dependance on the aperture scan direction angles and 2) are referenced to the absolute coordinate system being used.
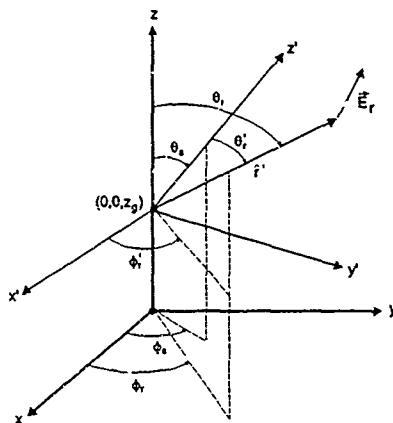
Figure 20. Primed and Unprimed Reference E-Field Coordinate Systems

The absolute coordinate system used for developing E-Field location expressions is unchanged from previous developments and is represented as the unprimed rectangular coordinate system shown in Figure 20. The radome orientation remains fixed with its base located in the x-y plane and its tip on the z-axis. Prior to gimballing and scanning the radar aperture is in the x-y plane. Given aperture scan angles θ_s and ϕ_s and gimbal point coordinates $(0,0,z_g)$, the primed/relative coordinate

system shown in Figure 20 is established. The location of $\tilde{E}_r$ is varied relative to the scanned aperture with location angles specified by θ_r' and ϕ_r' in the primed coordinate system. Location vector $\hat{r}'$ for $\tilde{E}_r$ may be expressed as shown in Eq (134) where unit vectors $\hat{x}'$, $\hat{y}'$, and $\hat{z}'$ define the primed coordinate axis. These unit vectors are converted to unprimed/absolute coordinate system components by application of the rectangular coordinate rotation equations of Eq (B.1), resulting in the equations summarized in Eq (135).

$$
\begin{aligned}
\hat{r}' &= x'\,\hat{x}' + y'\,\hat{y}' + z'\,\hat{z}' \\
&= \sin(\theta_r')\cos(\phi_r')\,\hat{x}' + \sin(\theta_r')\sin(\phi_r')\,\hat{y}' + \cos(\theta_r')\,\hat{z}'
\end{aligned}
\tag{134}
$$

Converting to Unprimed Coordinates

$$
\hat{x}' = (\cos^2\phi_s\cos\theta_s + \sin^2\phi_s)\,\hat{x} - \cos\phi_s\sin\phi_s(1-\cos\theta_s)\,\hat{y} - \cos\phi_s\sin\theta_s\,\hat{z}
\tag{135}
$$
$$
\hat{y}' = -\cos\phi_s\sin\phi_s(1-\cos\theta_s)\,\hat{x} + (\sin^2\phi_s\cos\theta_s + \cos^2\phi_s)\,\hat{y} - \sin\phi_s\sin\theta_s\,\hat{z}
$$
$$
\hat{z}' = -\cos\phi_s\sin\theta_s\,\hat{x} - \sin\phi_s\sin\theta_s\,\hat{y} + \cos\theta_s\,\hat{z}
$$

Given aperture scan angles θ_s/ϕ_s and relative E-Field location angles θ_r'/ϕ_r', vector expressions of Eq (135) may be substituted directly into Eq (134) to obtain the final location of $\tilde{E}_r$ in unprimed rectangular coordinates. The final expression obtained reflects the desired dependance on primed reference field location angles and unprimed aperture scan angles.

6.3 Reference E-Field Polarization

For defining an arbitrary polarization state of $\vec{E}_r$ the concept of a complex unit polarization vector is introduced. Utilizing a complex polarization vector allows for an unlimited number of polarizations states to be uniquely specified, including linear, elliptical and circular. A polarization ellipse is used to establish the various polarization states. For the polarization ellipse shown in Figure 21 the Axial Ratio (AR) and tilt angle τ are used to completely describe the polarization states of $\vec{E}_r$ [13]. For Figure 21 the following definitions apply:

OA = Semi-major ellipse axis

OB = Semi-minor ellipse axis

τ = Ellipse tilt angle, $0 \leq \tau \leq \pi$

AR = Ellipse axial ratio, $1 \leq AR = OA/OB \leq \infty$
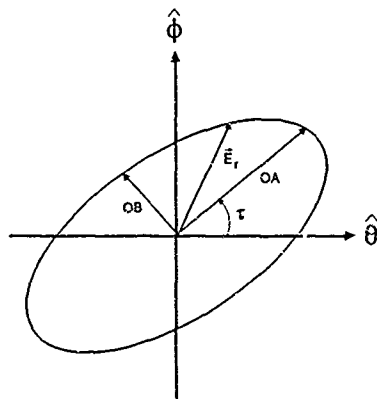
Figure 21. Reference E-Field Polarization Ellipse

100

For the following development the wave propagation direction is defined as $\hat{r}$ where $\hat{r} = \hat{\theta} \times \hat{\phi}$ in Figure 21. The orientation and rotational behavior of $\vec{E}_r$ defines the polarization state. Given that AR and τ are specified, Eqs (136) and (137) completely define the complex unit polarization vector $\hat{e}$. The phase term δ in the final $\hat{e}$ expression determines the complex nature of all possible polarization states. For all elliptical polarization states, including the special case of circular polarization, the rotation direction of $\vec{E}_r$ is determined by sign of AR. As viewed in the propagation direction, an AR > 0 produces left-hand (counter-clockwise) rotation and an AR < 0 produces right-hand (clockwise) rotation.

$$\hat{e} = \cos\gamma\,\hat{\theta} + e^{j\delta}\sin\gamma\,\hat{\phi} \tag{136}$$

$$\varepsilon = \cot^{-1}(AR) = \tan^{-1}\left(\frac{1}{AR}\right)$$

$$\gamma = \frac{1}{2}\cos^{-1}(\cos2\varepsilon\cos2\tau) \tag{137}$$

$$\delta = \tan^{-1}\left(\frac{\tan2\varepsilon}{\sin2\tau}\right)$$

Linear polarization states are achieved by letting AR approach infinity in the limit with τ being used to control the relative orientation of $\vec{E}_r$. For an AR approaching infinity the definitions in Eq (137) can be used to show that δ approaches zero while γ approaches the value of τ. Substituting these conditions into Eq (136) results

101

in the $\hat{e}$ expression of Eq (138). This final expression represents a time independent position vector in the $\hat{\theta}$-$\hat{\phi}$ plane with vector component magnitudes determined by the value of τ.

$$\hat{e} = \cos\tau \, \hat{\theta} + \sin\tau \, \hat{\phi} \tag{138}$$

For the ray-trace receive formulation being implemented two reference E-Field polarization variations are considered. For the first case the reference E-Field polarization vector $\hat{e}_r$ remains constant with respect to the absolute coordinate system regardless of the reference E-Field location. This case accounts for realistic flight conditions where the relative polarization of a fixed source remains unchanged for changes is aircraft elevation and azimuth. The second case allows the polarization vector $\hat{e}_r$ to vary as a function of the reference E-Field location. This case duplicates typical test range conditions where source and observer locations are varied in a circular arc with respect to each other.

For both polarization variations the reference E-Field polarization vector $\hat{e}_r$ is initially defined in the x-y plane with a $-\hat{z}$ propagation direction. Under these conditions, the complex polarization vector definition of Eq (136) may be applied to obtain the initial polarization vector expression for $\hat{e}_r$ as given by Eq (139) where $\hat{x}$ and $\hat{y}$ are unit vectors in the defined absolute coordinate system. For the constant polarization case Eq (139) represents the final $\hat{e}_r$ expression used for analysis and modeling validation. For the varying polarization case, unprimed reference E-Field coordinates and location angles θ_r/ϕ_r (calculated in accordance with *Section 6.2*) are

102

used in conjunction with the rectangular coordinate rotation expressions of Eq (B.1) to spatially rotate polarization vector components e_x^r and e_y^r to obtain the final $\hat{e}_r$ reference E-Field polarization vector.

$$\hat{e}_r = e^{j\delta} \sin\gamma \, \hat{x} + \cos\gamma \, \hat{y}$$
$$= e_x^r \, \hat{x} + e_y^r \, \hat{y} \qquad (139)$$

7.1 Introduction

This chapter presents a method for analyzing monopulse boresight errors. The development begins by considering the E-Fields incident on each element of the phased array and using the expressions developed in *Chapter V* to determine Co-Polarized (CP) and Cross-Polarized (XP) incident field components relative to both the reference E-Field and aperture element polarizations. Each polarization component is independently processed and analyzed such that radome depolarization effects are distinguishable from antenna element polarization sensitivity effects. Boresight error estimates in two orthogonal scan planes are generated from complex monopulse ratios. Dual plane boresight error analysis is accomplished in both principal and diagonal scan planes.

7.2 Co/Cross-Polarized E-Field Components

Co/Cross-Polarized field components are determined relative to a reference polarization direction. For analysis purposes two specific reference polarization directions are considered, the reference E-Field polarization direction $\hat{e}_r$ and the aperture element polarization direction $\hat{e}_A$. Depolarization effects due solely to propagation through the radome are determined by $\hat{e}_r$. The degree of radome depolarization is obtained by comparing $\hat{e}_r$ with the polarization of the E-Field incident on an array element.

The total incident E-Field $\bar{E}^T(m)$ on the mth array element is given by Eq (140) below where $\bar{E}_e^D(m)$ and $\bar{E}_e^R(m)$ are the incident E-Fields calculated in *Chapter V* for

104

"*Direct*" and "*Reflected*" ray paths, respectively. Summation of the n reflected E-Field terms accounts for multiple primary reflected ray paths for the mth element.

$$\vec{E}^T(m) = \vec{E}_e^D(m) + \sum_{j=1}^{n} \vec{E}_e^R(m,j)$$

$$= E^T(m)\, \hat{e}^T(m)$$

(140)

$$\vec{E}^T(m) = E^T(m)\left\{\hat{e}^T(m) \cdot \hat{e}_r + \hat{e}^T(m) \cdot \hat{h}_r\right\}$$

$$= \left\{\vec{E}_e^D(m) \cdot \hat{e}_r + \sum_{j=1}^{n} \vec{E}_e^R(m,j) \cdot \hat{e}_r\right\}\hat{e}_r$$

$$+ \left\{\vec{E}_e^D(m) \cdot \hat{h}_r + \sum_{j=1}^{n} \vec{E}_e^R(m,j) \cdot \hat{h}_r\right\}\hat{h}_r$$

(141)

$$= E_{CP}^T(m)\, \hat{e}_r + E_{XP}^T(m)\, \hat{h}_r$$

Given $\hat{e}_r$ and propagation direction $\hat{k}_i$, an orthogonal polarization vector $\hat{h}_r$ may be defined as $\hat{h}_r = \hat{k}_i \times \hat{e}_r$. Unit vectors $\hat{e}_r$ and $\hat{h}_r$ are used to decompose the total incident E-Field of Eq (140) into CP and XP components by a simple dot product operation. The incident E-Field is decomposed into orthogonal components as shown in Eq (141). Radome depolarization will manifest itself by introducing an XP response as indicated.

The primary goal is to characterize radome depolarization effects on the overall system, specifically the effects on boresight error. For this development the element polarization direction $\hat{e}_A$ is the primary vector used for CP/XP field decomposition

where it is assumed that $\hat{e}_A$ represents the polarization of a "typical" array element, neglecting any polarization differences due to the element's location within the array. Typical planar array elements include dipoles, open ended waveguides, slotted waveguides, and horns [1]. For planar arrays constructed with these elements the orthogonal polarization vector $\hat{h}_A$ is defined as $\hat{h}_A = \hat{n}_A \times \hat{e}_A$ where $\hat{n}_A$ is the aperture plane (i.e., plane containing array elements) surface normal vector. Aperture polarization vectors $\hat{e}_A$ and $\hat{h}_A$ are used to decompose the incident E-Field expression of Eq (140) into CP and XP components as shown below.

$$
\begin{aligned}
\vec{E}^T(m) &= E^T(m)\left\{\hat{e}^T(m) \cdot \hat{e}_A + \hat{e}^T(m) \cdot \hat{h}_A\right\} \\
&= \left\{\vec{E}_e^D(m) \cdot \hat{e}_A + \sum_{j=1}^{n} \vec{E}_e^R(m,j) \cdot \hat{e}_A\right\}\hat{e}_A \\
&\quad + \left\{\vec{E}_e^L(m) \cdot \hat{h}_A + \sum_{j=1}^{n} \vec{E}_e^R(m,j) \cdot \hat{h}_A\right\}\hat{h}_A \\
&= E_{CP}^T(m)\,\hat{e}_A + E_{XP}^T(m)\,\hat{h}_A
\end{aligned}
\tag{142}
$$

7.3 Element Voltages

By decomposing the incident E-Field into the CP and XP components identified in Eq (142) element polarization effects may be accounted for in determining element voltage responses. Figure 22 represents the basic element model used for deriving voltage expressions for the mth array element.

106
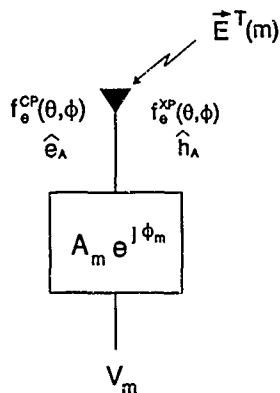
Figure 22. Aperture Element Model

The A_m and ϕ_m terms in Figure 22 represent the amplitude and phase weights used for controlling the shape and main beam pointing direction. Assuming mutual coupling effects are identical for all elements, regardless of their location within the array, the CP element pattern $f_e^{CP}(\theta,\phi)$, XP element pattern $f_e^{XP}(\theta,\phi)$, and element polarization directions $\hat{e}_A/\hat{h}_A$ are identical. This is a reasonable assumption for analyzing densely populated arrays which utilized amplitude tapers for pattern control. Array elements near the aperture edges exhibit atypical mutual coupling effects which are offset by amplitude weights which are significantly less than elements located near the center. Independent CP and XP element patterns allow for varying polarization responses to be analyzed depending on the specific element being used. For a typical element as shown in Figure 22 the total voltage response

107

V_m can be expressed as shown in Eq (143) where $E_{CP}^T(m)$ and $E_{XP}^T(m)$ are as given in Eq (142).

$$V_m = A_m \, e^{j\phi_m} \left\{ f_e^{CP}(\theta,\phi) \, E_{CP}^T(m) + f_e^{XP}(\theta,\phi) \, E_{XP}^T(m) \right\}$$
$$= V_{CP}(m) + V_{XP}(m)$$

(143)

7.4 Monopulse Error Signal

Monopulse sum and difference voltages are derived by applying the principle of superposition. The aperture's far-field radiation patterns are obtained by coherently combining the individual element responses as given by Eq (143). As identified in *Section 2.3*, a "*simple*" method for obtaining monopulse operation is implemented as shown in Figure 5 [1]. The system depicted in Figure 5 is for single plane monopulse processing, i.e., target/source location estimated with regard to a single scan plane. For this system the monopulse sum voltage V_{SUM} may be expressed as given in Eq (144) where the sum voltage is calculated by directly summing the individual element responses from all elements within the array. The monopulse difference voltage V_{DEL} is obtained by dividing the aperture into two symmetrical half-planes for which the element responses within each half-plane are summed. The half-plane sum voltages are then phase weighted and summed such that a 180° phase change occurs in V_{DEL} upon crossing from one half-plane to the other. Half-plane locations are arbitrary provided elements are symmetrically located on either side of the dividing line.

108

$$V_{SUM} = \sum_{m=1}^{I} \left(V_{CP}(m) + V_{XP}(m) \right)$$

$$= \sum_{m=1}^{I} \left[A_m \, e^{j\phi_m} \left\{ f_e^{CP}(\theta,\phi) \, E_{CP}^T(m) + f_e^{XP}(\theta,\phi) \, E_{XP}^T(m) \right\} \right]$$

(144)

A dual plane/four quadrant monopulse system is used for analysis and modeling purposes. Typical systems employ monopulse operation in two orthogonal planes, i.e., azimuth and elevation or equivalently, yaw and pitch. For these systems the aperture is divided into symmetrical quadrants and a monopulse difference voltage V_{DEL} is generated for each "plane" of monopulse operation. Element voltages within each aperture quadrant are summed to produce quadrant sum voltages. Quadrant sums are then combined to produce a single monopulse sum voltage and two independent difference voltages, one for each monopulse plane of operation. Sum and difference voltage expressions for analysis and modeling are derived by assuming the aperture is initially located in the x-y plane. As shown in Figure 23 the aperture is divided into four symmetrical quadrants A, B, C, and D. Element voltages of the form given by Eq (143) are summed within each quadrant to produce element quadrant voltages V_A, V_B, V_C, and V_D. For element coordinates given by $[x_e(m), y_e(m), 0]$ the resulting quadrant voltages may be expressed as given by Eq (145)

From the quadrant voltages of Eq (145) monopulse sum and difference voltages may be expressed as given by Eq (146) where the x-z and y-z planes correspond to the azimuth (AZ) and elevation (EL) planes, respectively. The 180° difference pattern phase shift required across the aperture is determined by the phase

109
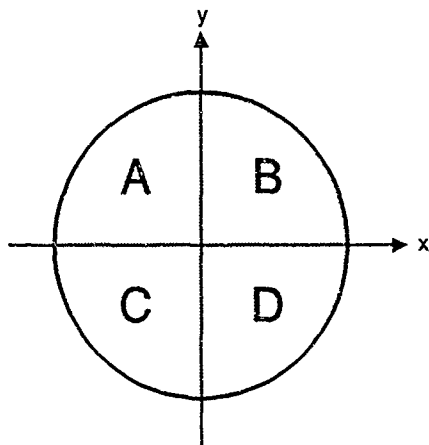
Figure 23. Four Quadrant Monopulse Geometry

$$V_A = \sum_m \left\{ V_{CP}(m) + V_{XP}(m) \right\} \quad for \quad x_e(m) < 0 \quad and \quad y_e(m) > 0$$

$$V_B = \sum_m \left\{ V_{CP}(m) + V_{XP}(m) \right\} \quad for \quad x_e(m) > 0 \quad and \quad y_e(m) > 0$$

$$\tag{145}$$

$$V_C = \sum_m \left\{ V_{CP}(m) + V_{XP}(m) \right\} \quad for \quad x_e(m) < 0 \quad and \quad y_e(m) < 0$$

$$V_D = \sum_m \left\{ V_{CP}(m) + V_{XP}(m) \right\} \quad for \quad x_e(m) > 0 \quad and \quad y_e(m) < 0$$

$$V_{SUM} = V_A + V_B + V_C + V_D$$

$$V_{DEL}^{AZ} = \left(V_A + V_C\right)e^{j\alpha} + \left(V_B + V_D\right)e^{-j\beta} \qquad (146)$$

$$V_{DEL}^{EL} = \left(V_A + V_B\right)e^{j\alpha} + \left(V_C + V_D\right)e^{-j\beta}$$

terms α and β. The values of α and β selected determine the "nominal" value of the relative phase difference between V_{SUM} and V_{DEL}. The "nominal" phase difference value represents an ideal system and is typically either 0° or 90°. The nominal relative phase difference is achieved under ideal conditions with plane wave illumination and no noise, clutter, or other multi-path effects present. Since it is generally impossible to predict specific deviations of the relative phase from its nominal value, radars are typically designed for one of the two nominal relative values [1]. For this development a nominal relative phase value of 0° is established by setting $\alpha = \beta = \pi/2$.

For generating the monopulse boresight error signal $E_{mp}(\gamma,\nu)$ from the complex monopulse voltage ratio V_{DEL}/V_{SUM} an "exact" monopulse processor is implemented. An "exact" monopulse processor is arbitrarily defined as a processor capable of producing the real part of the complex V_{DEL}/V_{SUM} ratio perfectly for each angle coordinate. For a nominal relative phase value of 0° the usual practice is to process only the real part of the complex ratio "The rationale is that the target contributes only to the real part while noise, interference, and clutter contribute equally to the real and imaginary parts" [1]. The "exact" monopulse processor boresight error $E_{mp}(\gamma,\nu)$ may be expressed as given by Eq (147) where the error is defined over

111

the angular range of γ at a frequency of ν. The monopulse sensitivity K is determined by the slope of the normalized difference pattern and has units of (v/v)/Rad [2].

$$E_{mp}(\gamma, \upsilon) = Re\left[\frac{V_{DEL}/V_{SUM}}{K}\right] = K^{-1}\frac{|V_{DEL}|}{|V_{SUM}|}\cos(\phi_D - \phi_S) \quad (Radians) \quad (147)$$

$$\text{where} \quad \phi_D = \text{Phase of } V_{DEL} \quad \text{and} \quad \phi_S = \text{Phase of } V_{SUM}$$

The expression in Eq (147) is referred to as an "error signal" because it represents the angular off-set of a source/target relative to the monopulse boresight axis. Under ideal conditions a far-field source located on the monopulse boresight axis produces a difference pattern voltage of zero and a maximum sum pattern voltage, resulting in $E_{mp}(\gamma, \nu)$ going to zero. A source/target not located on boresight produces a bipolar error signal with magnitude indicating the amount and sign indicating the direction of error.

7.5 System Boresight Error

The monopulse boresight error $E_{mp}(\gamma, \nu)$ is used to establish and characterize the boresight error for the overall radome, radar, and monopulse processing "system". In this context, "system" boresight error (BSE) is defined as the angle indicated by Eq (147) when the aperture has no pointing error, i.e., the aperture scan direction equals the source location. This is equivalent to fixing the aperture scan direction

112

while repositioning the source until Eq (147) equals zero. The angular difference between the scan direction and source location is the system BSE. As defined, the system BSE is the key metric used in characterizing monopulse tracking errors in the presence of radome depolarization and phase front distortion. For a given aperture scan direction the system BSE may be expressed as in Eq (148) where $\hat{n}_s$ is a unit vector in the aperture scan direction and unit vector $\hat{n}_{mp}$ represents the direction of the source location such that $E_{mp}(\gamma,\nu) = 0$. Hence, one has

$$\theta_{BSE} = \cos^{-1}\left(\hat{n}_s \cdot \hat{n}_{mp}\right) \tag{148}$$

8.1 Introduction

This chapter presents the procedures for validating results of *Chapters III* thru *VII*. An overview of the Fortran computer model is presented to summarize approximately 10,000 lines of computer code written to support the validation process. A model flow diagram, input parameters, and output data format are presented.

Modeled results are validated using limiting case data, published empirical and experimental data, and production "system" boresight error (BSE) acceptance test data. Limiting cases (zero BSE) considered include: air radomes, hemispheric radomes (over limited scan ranges), and radome boresight scanning. Published empirical and experimental data for a hemispheric radome with a displaced aperture is considered for initial model validation with measured BSE data. Measured BSE data from multiple production "system" acceptance tests is then used for final model validation. The validated production "system" model is used to characterize overall refractive effects on BSE prediction. Effects of refraction are characterized in both principal and diagonal scan planes.

8.2 Model Development

This section provides an overview of the model developed for validating analysis results obtained in *Chapters III* thru *VII*. Detailed coding procedures are not presented, rather basic model control and functional flow are considered. The developed model predicts the entire "front-to-back" performance of the overall

114

"system". Program control and flow is dictated by the key "system" component parameters identified in previous chapters. The model was developed on the VAX 8650 processing system and is comprised of one main program and approximately 40 subroutines, all written in a standard Fortran computer language. With the exception of two IMSL math/library subroutines used for solving reflection point equations of *Chapter IV*, the model is self-supporting.

Figure 24 is a functional flow diagram for the overall model. Model input data is provided in three separate data files, one data file per "system" component. The RADOME.IN data file provides ogive reference surface parameters and radome layer electrical parameters. In conjunction with a taper function subroutine, this data file completely describes the radome structure. The RADAR.IN data file provides control variables required to completely establish aperture and monopulse processing characteristics. Parameters controlled by the RADAR.IN data file include: mechanical/electrical scanning, element field pattern and polarization, element location, aperture amplitude taper, gimbal arm length and pivot point location, azimuth/elevation monopulse plane, and co/cross-polarized system Boresight Error (BSE) calculation. Operation of the overall "system" is controlled by variables contained in the SYSTEM.IN data file. This data file controls propagation characteristics and aperture scan angles. Propagation characteristics are controlled such that the model generates output data with or without a radome present, with or without reflection points included, and with or without overall refractive effects. Aperture scan angle control variables allow for three aperture scan patterns to be implemented, including: 1) a "diagonal" scan through the origin in an arbitrary

115
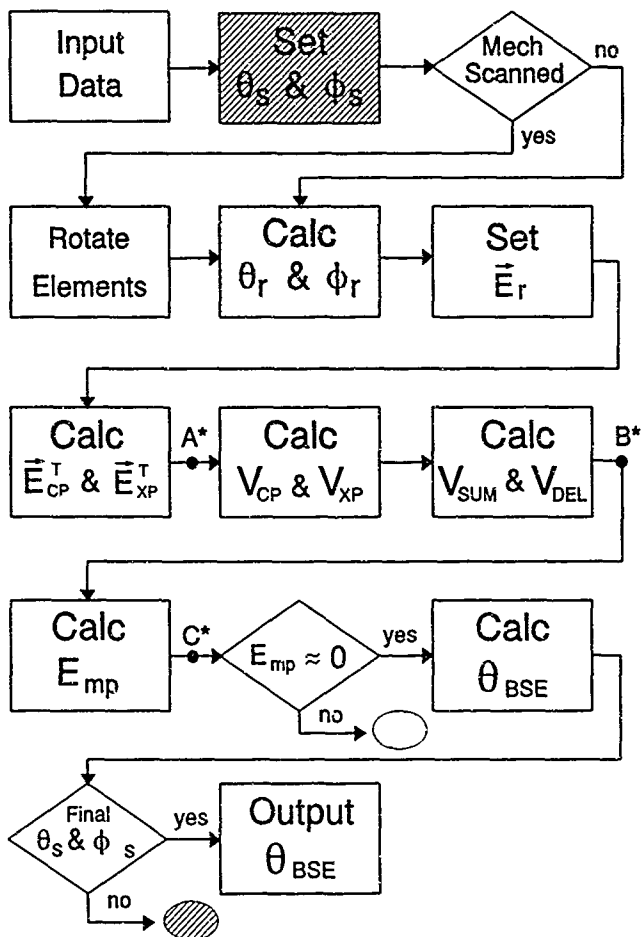
Figure 24. Model Flow Diagram

116

ϕ_s = constant plane, 2) an "azimuth" scan where θ_s and ϕ_s are varied to produce a constant elevation angle, and 3) an "elevation" scan where θ_s and ϕ_s are varied to produce a constant azimuth angle. The reference E-Field is also established and characterized by variables and parameters contained in the SYSTEM.IN data file. Reference E-Field location, axial ratio, tilt, magnitude, phase, and frequency are all determined in accordance with specified input data.

The flow diagram of Figure 24 indicates the final output of the model is BSE data. As defined in *Chapter VII*, system BSE is the key metric for characterizing the monopulse tracking error of the "system". An output BSE estimate/prediction is provided for each combination of θ_s and ϕ_s generated by the model. Aperture scan angles θ_s and ϕ_s are varied within the model according to the flow diagram Upon completing all θ_s/ϕ_s combinations, as dictated by the input data, a table of scan angles and corresponding BSE estimates is output.

User selectable intermediate outputs are available from the model at various points along the processing path. These outputs allow for "system" component responses to be independently analyzed and are identified as the A*, B*, and C* points in Figure 24. At A* co/cross-polarized incident E-Field components are available. This output contains phase front distortion and depolarization effects due solely to propagation through the radome. The level of radome depolarization may be ascertained by comparing the incident E-Fields at this point with an established polarization reference. Voltage outputs at B* are used primarily for characterizing the "system's" far-field radiation patterns and monopulse tracking sensitivity. Radar

117

performance (half-power beamwidth, first sidelobe level, etc.) is characterized at this point by generating model results with no radome present. The final intermediate output point C* allows for the monopulse error signal $E_{mp}(\gamma, \nu)$ to be analyzed under varying conditions presented by the radome and radar. This output corresponds to the monopulse "S-curve" used for pointing error corrections in monopulse tracking systems.

A series of comparative analysis data is presented to characterize and validate the model's performance. Limiting cases for which BSE = 0° are first considered as a means for establishing bounds on numerical processing and modeling errors. Empirically derived and published experimental results are used for limiting case data validations. Finally, measured BSE data from a radome production facility is used to complete the validation process. Refraction effects for specified radome structures are also investigated.

8.3 Limiting Case Validation

The "system" analysis results and computer model predictions are first validated by comparison with limiting case data, i e , special test cases for which system BSE is known to be zero. Three specific such cases were considered under the research effort. First, an arbitrarily thick single layer radome with both the relative permittivity ϵ_r and relative permeability μ_r set to unity will result in a system BSE of zero. This condition effectively places an "*air*" radome into the propagation path while introducing no depolarization or phase front distortion effects. The second limiting case considered is a hemispheric radome. Regardless of the number of

118

radome layers, layer thicknesses, and layer electrical properties, a "hemispheric radome will have zero boresight error if the receiving aperture is located at the sphere center" [6]. Regardless of where the aperture is scanned within the hemisphere, the symmetrically distorted phase front incident on the aperture produces zero BSE. This is also true for arbitrarily shaped radomes when the aperture is "looking"/scanned through the radome's boresight axis (tip) if the radome is circularly symmetric which is the case for all cases considered in this effort. All limiting case BSE data is generated using a mechanically scanned 32-element 5-wavelength diameter aperture with dimensions as shown below.


$$\triangle x = \triangle y = .8 \lambda$$
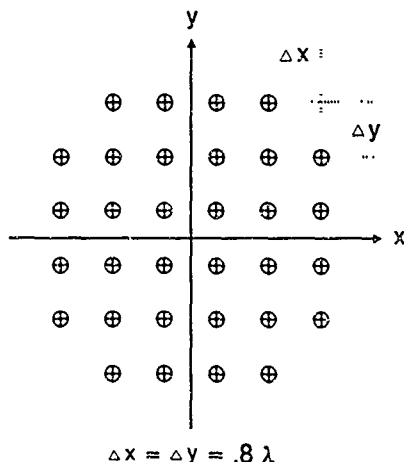
Figure 25. 32-Element Quadrant Symmetric Aperture

119

The aperture in Figure 25 is quadrant symmetric with uniform amplitude weights applied to the elements. This particular aperture configuration is of interest because 1) limiting case BSE conditions are independent of aperture and monopulse processing characteristics and 2) experimental data for this configuration is available. Radar parameters were input into the model and the model run for the case with no radome present. The normalized sum and difference patterns of Figures 26 and 27 were returned from the model. Data plotted in Figure 26 reveals a Half-Power Beamwidth (HPBW) of approximately .2027 Rads and a First Sidelobe-Level (FSLL) of approximately -15.0 dB for both the co-polarized and cross-polarized field pattern responses. The cross-polarized response is obtained by setting the reference E-Field polarization orthogonal to the element polarization without changing the reference E-Field scan plane. The decreased cross-polarized response at higher scan angles results from polarization mismatch conditions. The HPBW and FSLLs generated by the model compare very well with experimental and empirical data. From Figure 25 it is observed that the 32-element aperture is neither truly rectangular nor truly circular. A 5-wavelength rectangular aperture with uniform amplitude illumination will exhibit a HPBW and FSLL on the order of .1766 Rads and -13.26 dB, respectively. An equivalent circular aperture has a HPBW and FSLL on the order of .2038 Rads and -17.6 dB, respectively [15]. The .2027 Rad HPBW and -15 dB FSLL obtained from the model fall well within these limits and are acceptable for validating the model for cases with a radome present.
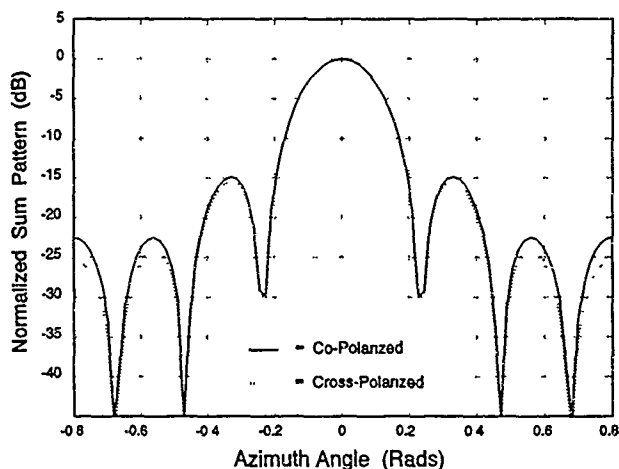
Figure 26. Co/Cross-Polarized Normalized Sum Patterns

The normalized difference pattern plotted in Figure 27 characterizes the sensitivity of the monopulse system and represents both the co-polarized and cross-polarized responses which are identical for the case considered. The monopulse sensitivity K of the system is defined as the slope of the normalized difference pattern near boresight, i.e., at an azimuth angle of zero. From the data used to plot Figure 27 a value of $K = .1158$ (v/v)/Deg was obtained. This compares very favorably with a published sensitivity value of $K = .11$ (v/v)/Deg [2]. With radar far-field patterns and monopulse sensitivity accurately characterized, model validation using limiting case BSE conditions is next considered.

121
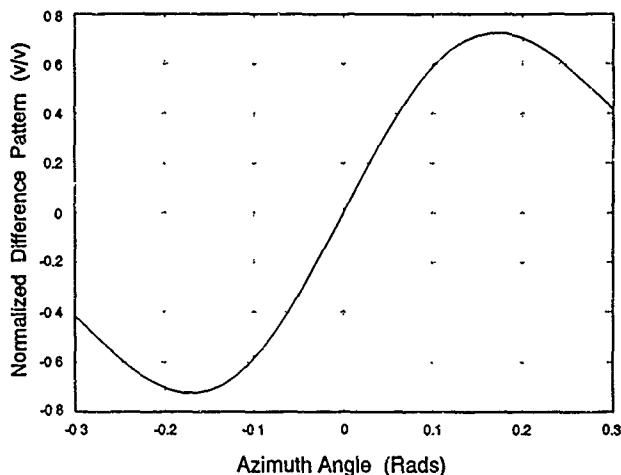
Figure 27. 32-Element Aperture Normalized Difference Pattern

8.3.1 Air Radomes. Various combinations of air radome parameters were input into the model using the 32-element radar and monopulse processing previously validated. Figures 28 and 29 represent typical BSE data returned from the model. Figure 28 represents data obtained for the "TE" polarization case using a constant thickness radome with three different fineness ratios. Figure 29 is equivalent data for the "TM" polarization case. The "TE" and "TM" polarization designations are determined by the orientation of the element polarization vector $\hat{e}_e$ and reference E-Field polarization vector $\hat{e}_r$ relative to the aperture scan plane. The designation "TE" is used when both $\hat{e}_e$ and $\hat{e}_r$ are perpendicular to the aperture scan plane.

122

Likewise, the "TM" designation is used when both $\hat{e}_c$ and $\hat{e}_r$ are parallel to the aperture scan plane (this convention is used throughout the remainder of the dissertation).
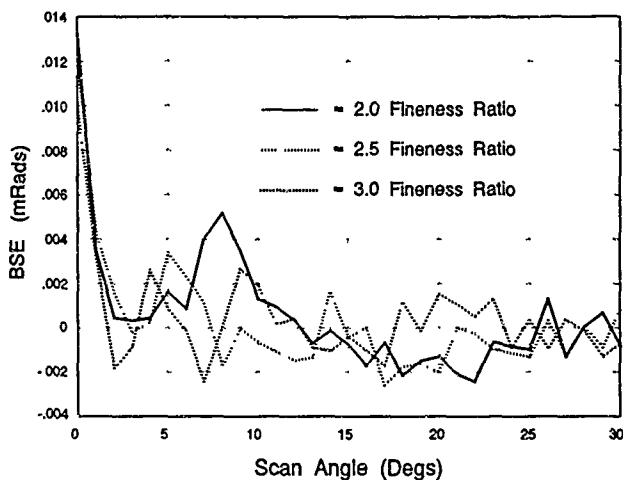
Figure 28. Limiting Case BSE, Air Radome TE Polarization

For the six cases shown in Figures 28 and 29 the predicted BSE is less than .014 mRads over the 30 degree scan range when compared to a theoretical value of zero degrees. Approximately twelve additional test cases were run for varying radome structures, including multi-layer tapered designs with as many as four layers. For all cases considered the predicted BSE never exceeded the .014 mRad. The .014 mRad numerical/modeling error is approximately two orders of magnitude

123

below expected measured BSE values. Typical radome BSE maximum values fall in the range of 2 to 8 mRads. Hence, the .014 mRad modeling error is within acceptable limits.
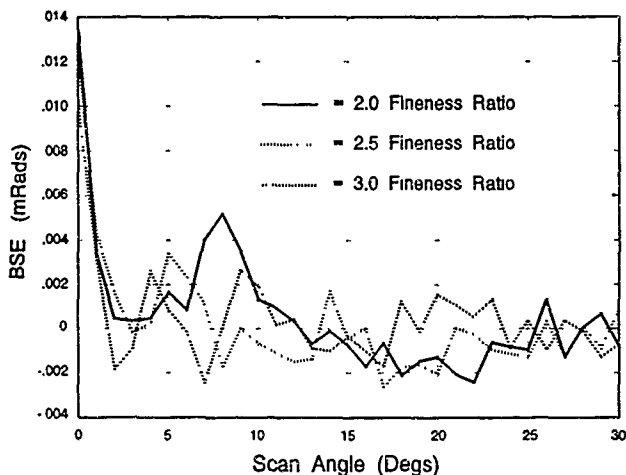
Figure 29. Limiting Case BSE, Air Radome TM Polarization

8.3 2 Hemispheric Radomes. A hemispheric radome induces symmetrical phase front distortions on an incident plane wave and as noted previously, a receiving aperture located at the sphere center will indicate zero BSE. Figures 30 and 31 represent BSE data satisfying this condition. The data presented is for a specific radome design of a half-wave constant thickness hemispheric radome smoothly terminated in a cylindrical section.

124
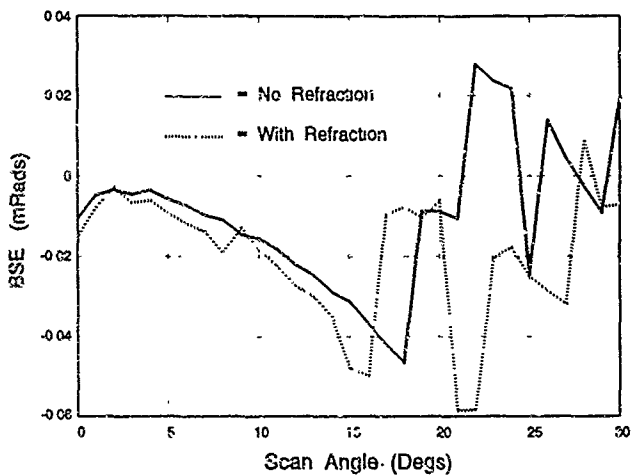
Figure 30. Limiting Case, Hemispheric Radome TE Polarization

The data was generated using ogive reference parameters of $R = 3.4\lambda$, $W = 6.8\lambda$, and a dielectric constant of $\epsilon_r = 5.3$. For both the TE and TM polarization cases, a curve showing overall refractive effects is also included. As shown, refractive effects do influence system BSE but do not significantly impact BSE magnitude. Equivalent BSE results were obtained for both single layer and multi-layer hemispheric radomes with dielectric constants varying between 4.8 and 9 3. For all hemispheric test cases considered, the limiting case BSE magnitude was less than .06 mRads for all scan angles. The erratic behavior/fluctuation in BSE estimates beyond a 10° scan angle is attributable to an interaction between radar sidelobes and

125

the cylinder section termination. Although these effects tend to increase the average limiting case BSE, the .06 mRad upper limit BSE estimate is acceptable for all practical purposes.
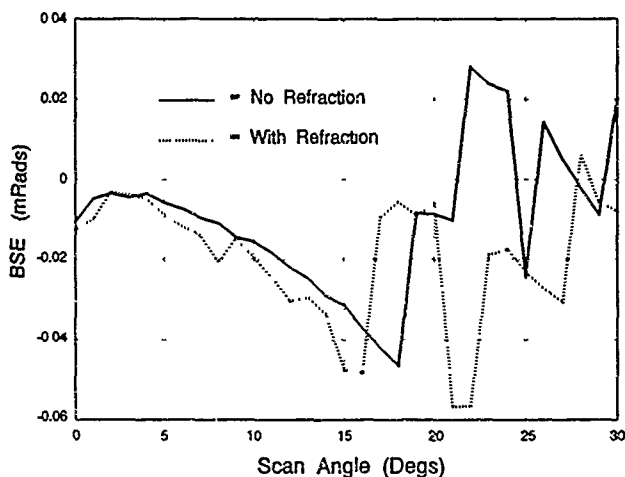
Figure 31. Limiting Case, Hemispheric Radome TM Polarization

8.3.3 Radome Boresight Scanning. Circularly symmetric radome structures induce symmetrical phase front distortions on incident plane waves upon propagating through the radome along the boresight axis, i.e., through the tip. This limiting case condition parallels the preceding hemispheric radome case and occurs regardless of the actual radome design, i.e., is independent of the number of radome layers and electrical properties. Radome designs used for generating data in Figures 28 and 29

were used to establish a worst case BSE error estimate for an azimuth scan angle of 0°. Multi-layer and single layer radome designs with fineness ratios in the range of 2 to 3 were considered. Radome design frequency, number of layers, and electrical properties were varied for both the TE and TM polarization cases. Given a specific number of radome layers, corresponding taper functions (including constant thickness), and a specified fineness ratio, the system BSE at 0° remained virtually constant for all variations of radome electrical properties, E-Field polarizations, and refractive effect combinations. The maximum limiting case BSE obtained was primarily dependent on radome geometrical properties and varied between .01 and .02 mRads for all test cases considered. As with previous limiting case BSE bounds, this error limit is acceptable and finalizes the analysis and modeling validation under limiting case conditions.

8.4 *Hemispheric Radome Validation: Displaced Aperture*

Initial validation of analysis and modeling results with experimentally measured data is accomplished using a "system" comprised of the 32-element quadrant symmetric aperture and the uniform half-wave hemispheric radome of *Section 8.3.2* with $R = 3.4\lambda$, $W = 6.8\lambda$, and $\epsilon_r = 5.3$. The aperture center of rotation/pivot point is displaced one wavelength behind the radome center of curvature, intentionally introducing a small measurable amount of system BSE. Model results are validated by comparison with published experimental and predicted BSE data. The data plotted in Figures 32 and 33 represents measured (∗) and numerically predicted (o) results for 'system" BSE [2].
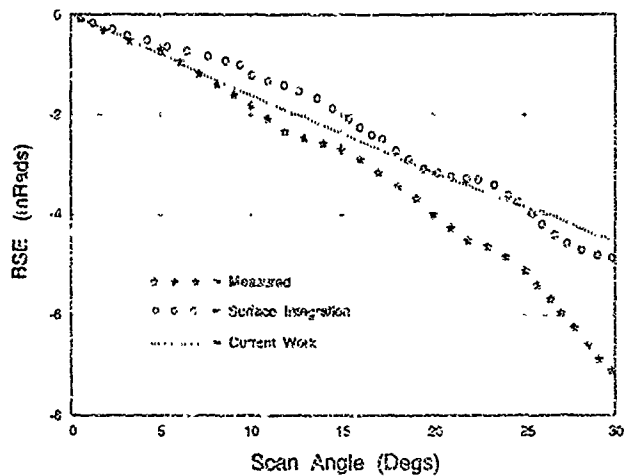
Figure 32. Hemispheric Radome, Displaced Aperture TE Polarization
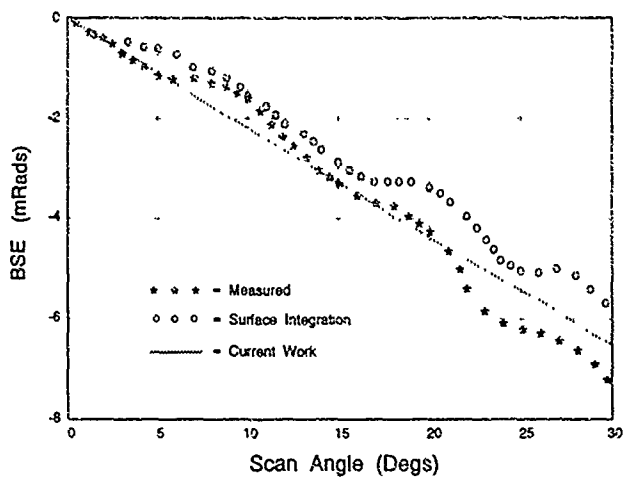
Figure 33. Hemispheric Radome, Displaced Aperture TM Polarization

128

The dashed line represents model results and clearly indicates a good first-order approximation to plotted curves. Because of restrictions placed on the reflected E-Field contributions during model development, i.e., reflected E-Field equations of *Chapter IV* are valid only for radomes with fineness ratios greater than two, the first-order approximation of the model does not possess the higher-order variations present on the measured and numerically predicted data (by definition all hemispheric radomes have a fineness ratio of one). Numerically predicted estimates of the published data were obtained via a computationally intense surface integration technique. Current model results, obtained from a geometric optics technique which ranks much lower in computational intensity, compares very well with the surface integration results. In fact, data presented in Figures 32 and 33 indicates the current technique provides a superior estimate of first-order BSE characteristics (considering the average slope of the data presented).

Consistent with previous modeling efforts, the correlation between measured and predicted data is better for the TM polarization case than it is for the TE polarization case. These differences are generally "associated with the planar slab approximation for TE and TM modes in the highly curved radome tip region" [2, 21]. Locally planar approximations are less valid in this region resulting in poorer transmission coefficient estimates. Although there is no "highly" curved tip region for the hemispheric radome under consideration, the radius of curvature in the perpendicular (TE) plane of incidence is smaller than the radius of curvature in the parallel (TM) plane of incidence for a given azimuth scan angle. Considering the terminated hemisphere geometry and displaced aperture location, the radius of

129

curvature decreases for TE polarization and increases for TM polarization as the azimuth scan angle is increased. This condition accounts for poorer BSE correlation at higher scan angles for the TE polarization test case.

8.5 Production System Validation

8.5.1 Introduction. A production radome. radar, and monopulse processing "system" is considered for final analysis and modeling validation. The production "system" is used for model validation for several reasons. First, measured electrical and mechanical data is available on each component of the "system". Given measured component data, intermediate model outputs may be used to validate individual component responses prior to validating the overall model response. Second, acceptance test/quality control data from several production units is available. Validated analysis and modeling results are obtained by comparison with average data from multiple test cases, eliminating the possibility of validating against an 'isolated" test case which "happens" to match model results. Third, acceptance test results on production units are well documented and accomplished under tightly controlled test conditions. Therefore, model inputs may be established such that modeled conditions accurately match conditions used in taking measured data. Lastly, measured system BSE data is available on the overall integrated "system". A final acceptance test accomplished by radome production facilities involves characterizing the system's far-field radiation patterns and BSE response. A complete radome. radar, and monopulse processing system is utilized for these tests.

130

Final analysis and modeling validation is accomplished by comparing model results with the final system BSE measurements.

The following sections describe the validation process used. As with previous validation cases, the radar aperture and monopulse processing portions of the model are completely characterized and validated prior to including a radome in the system. All component specifications and measured data used in the following validation process were provided by a radome production facility. The "system" used is comprised of a mechanically scanned 1368-element aperture corporately fed to produce dual-plane monopulse processing and a single layer tapered radome.

8.5.2 Modeled Radar Aperture. A mechanically scanned 1368-element planar array is used for validating the radar and monopulse processing portion of the model. The aperture is approximately 28-wavelengths in diameter with array elements oriented in a triangular lattice grid pattern. The elements are slotted waveguides possessing negligible cross-polarized responses. A corporate RF feed structure is used to simultaneously produce a single sum pattern output and independent azimuth (x-z plane) and elevation (y-z plane) difference pattern outputs. The measured (*) data plotted in Figure 34 represents the normalized radial amplitude taper applied across the aperture. By comparing the raised cosine and $cosine^2$ amplitude tapers with the measured taper, it is evident that the measured taper approximately equals the cosine taper for radial distances less than one-third. Beyond this point, the measured taper is approximately the average value of the cosine and $cosine^2$ tapers

131

These conditions define the amplitude taper used for model validation and are summarized by Eq (149) where x is the normalized radial distance from the aperture center [22]. Equation (149) is plotted in Figure 35 for comparison with the measured taper using a pedestal height of $h = .185$. Taper values calculated in accordance with Eq (149) closely approximate the measured taper and are acceptable for modeling purposes.
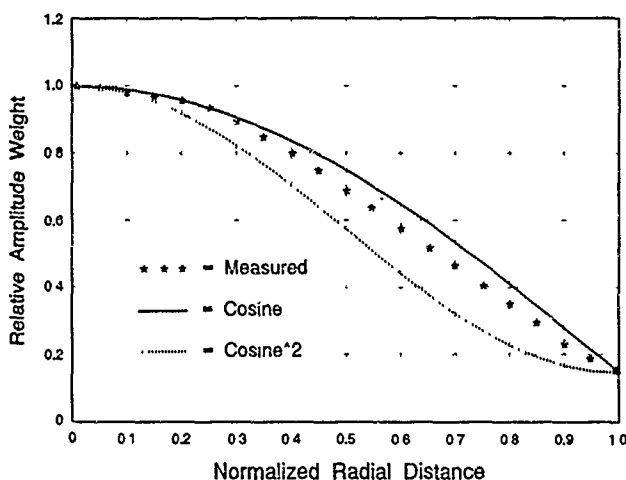
Figure 34. Amplitude Taper, Measured vs. Cosine/Cosine^2

$$A(x) = \begin{cases} h + (1-h)\cos\left(\dfrac{\pi x}{2}\right) & 0 \le x \le .3 \\[4mm] h + \dfrac{1}{2}(1-h)\cos\left(\dfrac{\pi x}{2}\right)\left\{1 + \cos\left(\dfrac{\pi x}{2}\right)\right\} & .3 < x \le 1 \end{cases} \qquad (149)$$

132
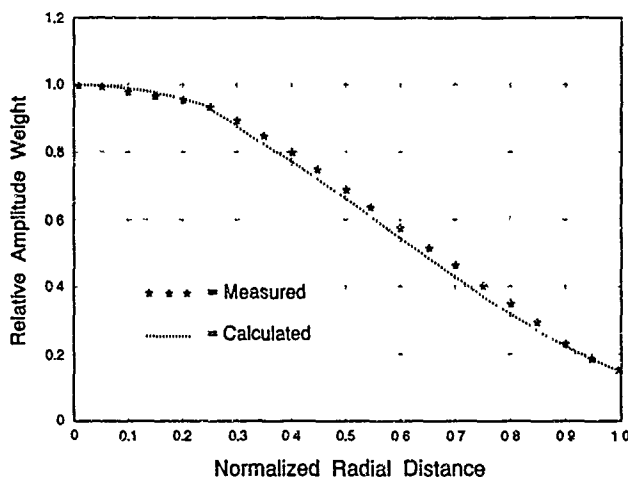
Figure 35. Amplitude Taper, Measured vs. Calculated

The modeled amplitude taper of Eq (149) is used in conjunction with given array element locations to characterize and validate the radar far-field pattern characteristics and monopulse processing sensitivity. Figures 36 and 37 show the co-polarized normalized sum and difference pattern responses of the modeled radar system. A HPBW of 2.488° and FSLL of -30.07 dB were calculated from model results of Figure 36. These radiation parameters compare extremely well with specified/measured HPBW and FSLL values of 2.5° and -30 dB, respectively, validating the modeled radar geometry and amplitude taper function.

133
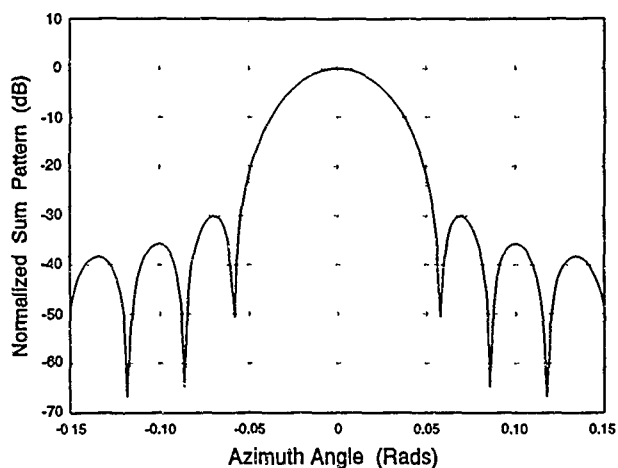
Figure 36. Production System, Normalized Sum Pattern
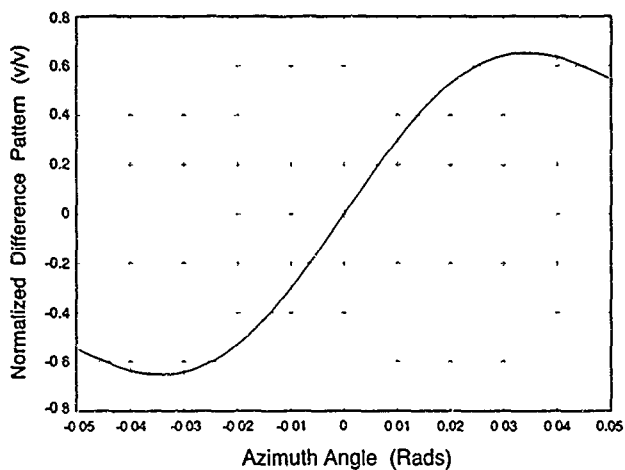
Figure 37. Production System, Normalized Difference Pattern

134

The co-polarized normalized difference pattern of Figure 37 is used to characterize the radar system's monopulse sensitivity. From the slope of the normalized difference pattern at an azimuth angle of 0°, a calculated monopulse sensitivity of $K = 31.0$ (v/v)/Rad is obtained. This model value identically matches the measured sensitivity value provided by the radome production facility. The near perfect pattern characteristics and monopulse sensitivity value clearly validate the model's radar response for the production system.
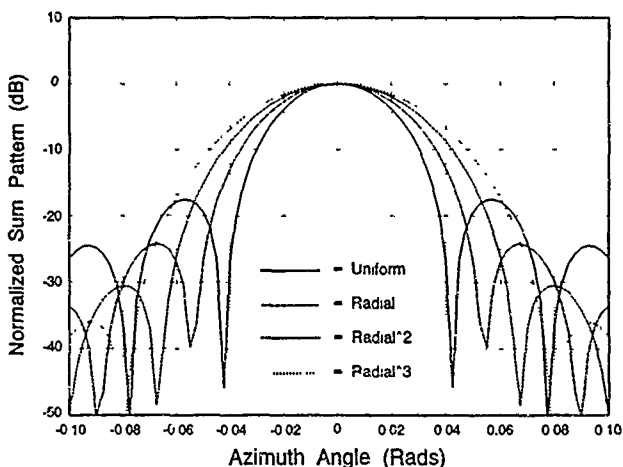
Figure 38. Production Aperture, Uniform/Radial Taper Comparison

The modeled production system radar is used to validate the model response for various amplitude tapers Far-field patterns using the 1368-element 28-wavelength diameter aperture were generated for various amplitude tapers provided by the

135

model. Specifically, uniform and radial (approximate cosine) amplitude tapers were characterized. Figure 38 is a plot of calculated sum patterns comparing a uniform amplitude taper response with three different radial tapers. Table 1 provides comparison data for calculated HPBW and FSLL values from data of Figure 38 and published theoretical data for circular apertures [17]. Calculated HPBW and FSLL values compare very well with corresponding theoretical values, validating model results for the tapers considered.

Table 1. Taper Comparison, Calculated/Theoretical HPBWs and FSLLs

TAPER	Uniform	Radial	Radial[2]	Radial[3]
HPBW (Deg)	2.08 / 2.02	2.44 / 2 52	2.75 / 2.91	3.15 / 3.34
FSLL (-dB)	17.53 / 17.60	24.19 / 24.50	30.48 / 30.50	35.95 / 35.80

(Calculated / Theoretical)

8 5.3 Modeled Production Radome   The production radome considered for validation purposes is a single layer tapered radome. The specific design selected satisfies the circularly symmetric requirement and falls within the moderate-to-large sized class of radomes (exceeds the 5 to 10-wavelength dimensional requirement)

136

The radome is produced on an inner contour mandrel by building up a layer of dielectric material exceeding the desired Outer Mold Line (OML) thickness specifications. Once properly cured, the radome OML is ground to specifications such that the desired radome taper is achieved. Radome production specifications and acceptance test data packages were obtained on three identical radome units from an unidentified production facility. Acceptance test data packages for the three radomes were randomly selected from approximately 40 available production units. Measured "system" BSE data used in the following validation process is "average" data, representing averaged BSE values from the three selected production units.

The first step in validating model results with the production radome was to determine/define the reference ogive surface parameters R and W. Mandrel data supplied with the radome specifications was plotted and compared with several ogive surfaces generated by varying ogive parameters R and W. Comparisons revealed that the production radome inner surface could be very closely fitted to a truncated tangent ogive surface, i.e., a non-tangent ogive surface generated by displacing the tangent ogive base plane toward the ogive tip. By using a tangent ogive reference surface with a compensated aperture gimbal point location, an accurate inner radome surface equation was generated using values of $R = 234.472\lambda$ and $W = 36.136\lambda$, resulting in an overall radome length of $L = 90.26\lambda$ The specified aperture gimbal point location of $z_g = 15.933\lambda$ was re-established as $z_g = 28.991\lambda$ for the modeled radome. The specified gimbal arm length of 3.983λ remained unchanged for modeling purposes.

137

The OML grind specifications were used in conjunction with established ogive reference surface parameters to determine the layer taper function $t(\theta)$. A list of radome station locations (distances from the radome tip) and corresponding grind thicknesses were provided with the radome production data. The thicknesses provided were determined on the original radome development effort by empirical methods using countless "build and test" iterations. As such, no analytical procedures were applied to determine/establish a "function" to accurately describe the radome taper. Since the grind thicknesses were measured along the surface normal direction at given radome station locations, the procedure developed in *Section 3.4.2* for generating "*ideal*" taper functions, Eqs (50) thru (55), was applied to convert normal thickness grind specifications into corresponding taper function values. Specifically, grind thickness values were used in place of the d_n values calculated by Eq (52).

The normalized taper function profile obtained from the procedure using the grind specifications is provided in Figure 39 as "actual" taper values. The lack of "smoothness" at scan angles around 5° is attributable to constant normal thickness grind specifications in the radome tip region. The actual radome taper as a function of surface normal direction begins at about 9.5λ from the radome tip. The "*ideal*" Gaussian taper function of Eq (56), as established using identical ogive surface parameters and dielectric constant for a half-wave wall design, is also plotted in Figure 39. The shape of the two curves is nearly identical with a difference of less than $.05\lambda$ in normalized taper value over the 30° scan range. In fact, a shift in scan angles of approximately 5° for either of the two curves results in a near perfect match. Given that the original radome taper design was empirically "tuned" for

138

optimum transmission and BSE performance, the near perfect fit of "actual" and "*ideal*" curves in Figure 39 represents an important step in validating the "*ideal*" taper function concept developed in *Section 3.4.2.*
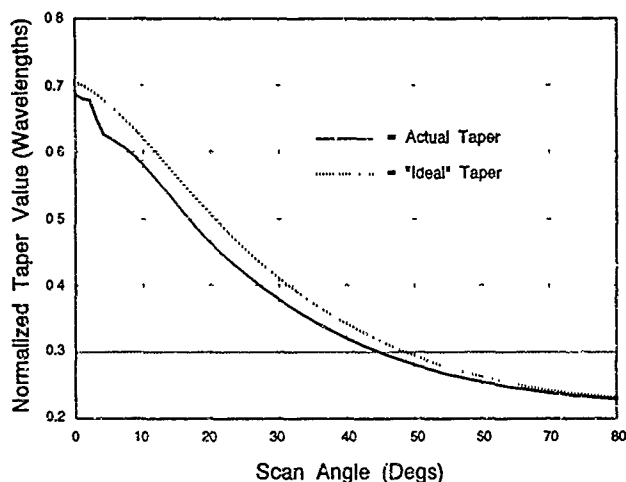
Figure 39. Production Radome, Actual vs. "Ideal" Taper

8.5.4 Final BSE Validation. The actual and "*ideal*" taper functions are both used in the final BSE validation procedure Acceptance test BSE data was provided at two distinct test frequencies. The measured (*) data points in Figures 40 and 41 represent averaged BSE values at frequencies of F_D and F_H, respectively. These frequencies represent the radome design frequency (F_D) and the upper edge limit of an 8.5% bandwidth (F_H). The data was obtained using linearly polarized array

139

elements ($\hat{e}_e = \hat{x}$) and a variably polarized reference E-Field ($\hat{e}_r = \hat{x}$). A nominal dielectric constant value of $\epsilon_r = 4.8$ with a loss-tangent of .014 was assumed for the tapered layer. The aperture was scanned in the monopulse azimuth plane (x-z plane) and corresponding in-plane BSE estimates were computed. The solid and dashed curves represent model results using the actual and "*ideal*" tapers, respectively. Modeled production "system" results required approximately 20 minutes of computer processing time to calculate and output 31 discrete scan angle and BSE estimates, approximately 40 seconds per θ_s/ϕ_s combination. This equates to a processing time of approximately 30 mSec/element/scan angle for the 1368-element aperture being modeled. Considering the goal to limit computational intensity, this is an acceptable processing rate for developmental system design efforts.

Comparison of measured BSE data with modeled results using the actual taper reveals a BSE prediction error of approximately .5 mRads or less for both frequencies considered, extremely good prediction results considering the geometric optics propagation technique being implemented. For a moderate decrease in the nominal dielectric constant value (approximately 6%) a near perfect match between actual taper and measured BSE data could be achieved. Radome production tolerances and variations in dielectric material electrical properties could easily account for a .5 mRad prediction error. Given that these results were obtained for 1) an arbitrarily selected radome design satisfying dimensional and symmetry requirements, 2) multiple randomly selected production radome units, and 3) multiple frequency BSE measurements, they clearly validate the overall analysis and modeling approach developed in *Chapters III* thru *VII* for the production "system" considered.
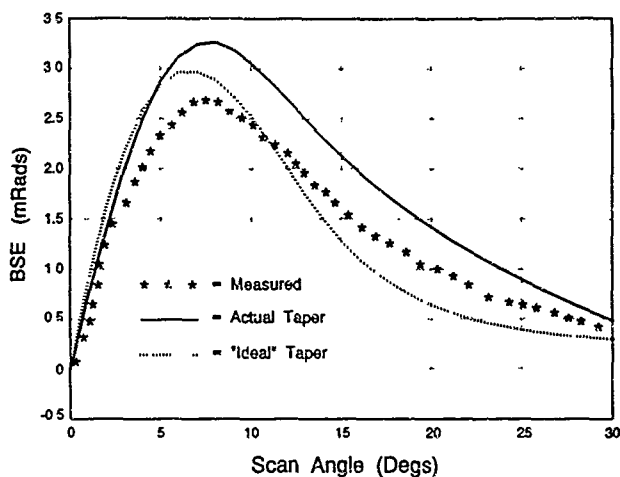
Figure 40. Production Radome BSE Comparison at F_D
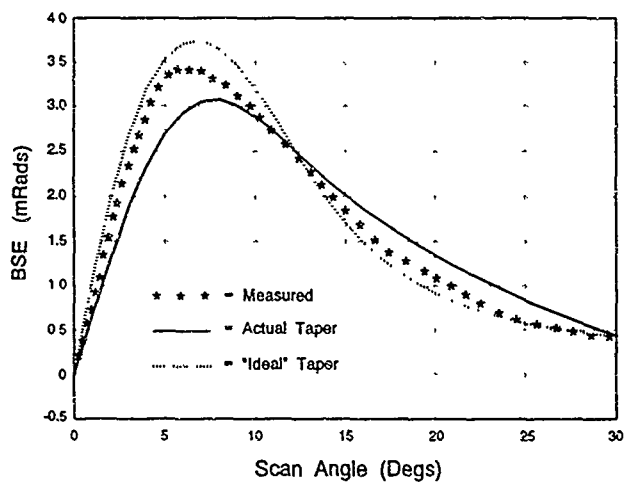
Figure 41. Production Radome BSE Comparison at F_H

141

"*Ideal*" taper model results plotted in Figures 40 and 41 compare favorably with actual taper and measured BSE data. At F_D "*ideal*" BSE predictions are consistently lower than actual taper results. Assuming predicted BSE results are consistently higher than measured BSE values, as indicated in Figure 40 by comparison of actual taper and measured BSE values, the lower "*ideal*" BSE predictions suggest that implementation of the "*ideal*" taper function in an actual radome structure may improve measured BSE performance. Data presented in Figures 39 thru 41 relating actual taper and "*ideal*" taper characteristics strongly suggest that the "*ideal*" taper function development process produces a candidate taper function which 1) closely approximates empirically "tuned" tapers, potentially resulting in fewer "build-and-test" iterations during radome design/development, and 2) yields modeled BSE predictions which are consistent with both measured and empirically tuned results.

8.6 Refractive Effects on BSE Prediction

Refractive propagation effects on BSE prediction are characterized using the validated production "system" model. Refractive effects are incorporated into the model in accordance with procedures developed in *Section 5.5* and are characterized in both principal and diagonal scan planes at several test frequencies.

The azimuth monopulse processing plane (x-z plane) is used for principal scan plane characterization. Figures 42 and 43 are modeled results obtained for frequencies of F_D and F_H, respectively. A marginal reduction in predicted BSE is indicated over the 30° scan range, corresponding to a marginal improvement in BSE prediction when compared with data in Figures 40 and 41.
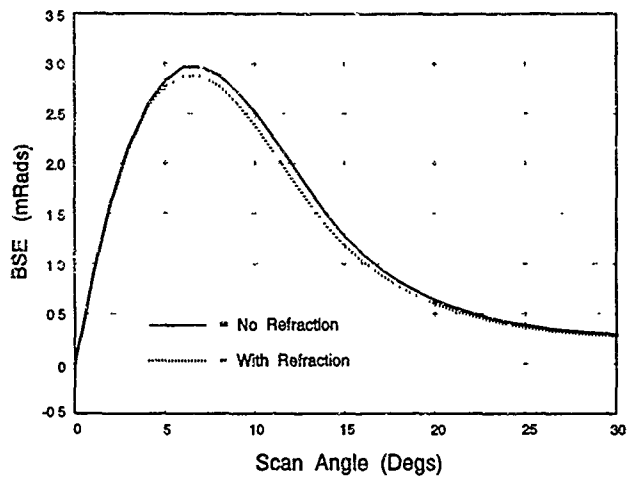
Figure 42. Principal Plane Refractive Effects at F_D
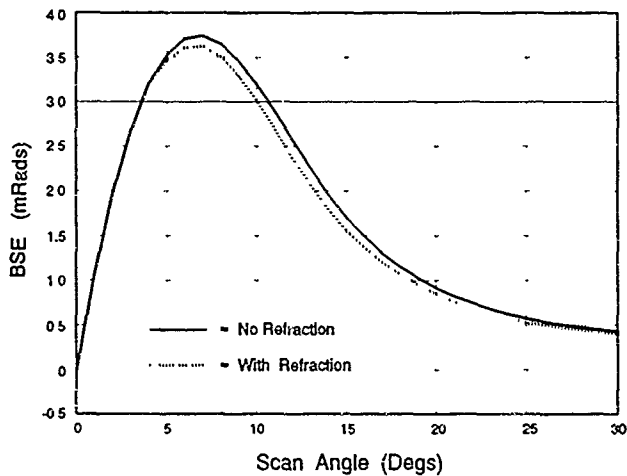
Figure 43. Principal Plane Refractive Effects at F_H

143

The marginal improvement in BSE prediction is achieved at the expense of computational efficiency. Additional convergence requirements and overhead calculations are required when overall refractive effects are included in model calculations. Refractive effect calculations increase computer processing time by approximately 80%, from 20 to 36 minutes for 31 discrete data point calculations. A severe processing penalty is incurred if second-order refractive effects are included in BSE calculations when considering the marginal "improvement" in predicted BSE values.

Diagonal scan plane characterization is included for completeness. Field pattern anomalies in the diagonal scan plane generally result in poorer measured "system" BSE performance for given "system" designs. Cross-polarized field components and asymmetrical phase front distortions are introduced along diagonal scan planes, producing "system" BSE in both the azimuth and elevation monopulse processing planes. Data presented in Figures 44 thru 46 represents modeled BSE results for a diagonally scanned aperture and is "typical" of data obtained for both monopulse processing planes. The aperture was scanned from the origin in a constant $\phi_s = \pi/4$ Rad scan plane. Data presented is for three distinct frequencies representing the design frequency F_D and lower/upper band edges of a 6.5% bandwidth, F_L and F_H respectively. The figures clearly indicated marginal difference between refractive and non-refractive test cases. As with the production "system" refractive results, a marginal improvement in BSE prediction is obtained for a substantial sacrifice in computational efficiency.

144
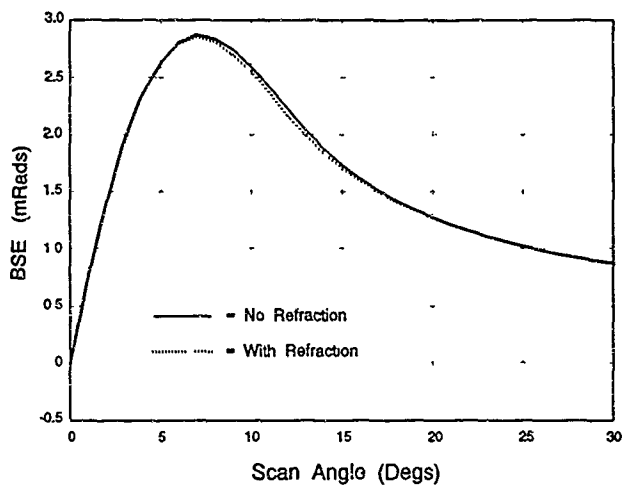
Figure 46. Diagonal Scan Refractive Effects at F_H

Figure 46. Diagonal Scan Refractive Effects at F_H

146
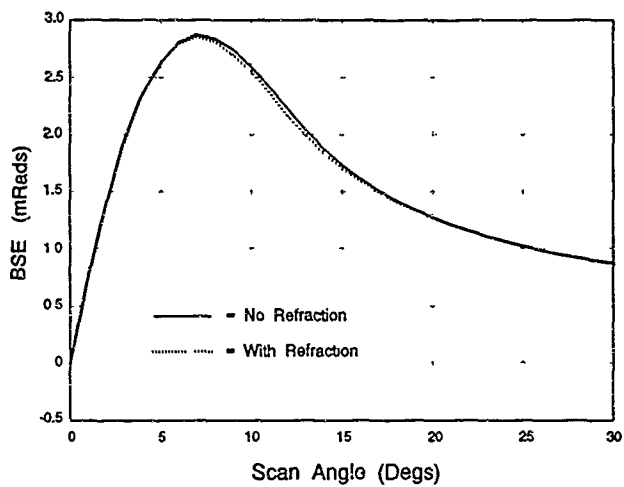
IX. Conclusions and Recommendations

9.1 Conclusions

A unique analysis and modeling approach was developed to determine radome depolarization and phase front distortion effects on monopulse receiver tracking performance. Previously developed ray-trace receive propagation techniques were modified to include ray refractive effects in analyzing moderate- to large-sized radar/radome systems. A novel multi-layer tapered radome model was developed to analyze arbitrarily shaped radomes using a tangent ogive reference surface. The radome model development included a unique "*ideal*" taper function concept based on maintaining constant electrical thickness for arbitrary aperture scan angles. Reflected E-Field contributions were incorporated into the analysis using calculated reflection points, equations developed for an arbitrary reflecting surface were used to determine specular (primary) reflection point coordinates. Analysis results were implemented in a Fortran computer model which predicts the "front-to-back" boresight error (BSE) performance for an integrated "system." Model results were validated using empirical limiting case data, published experimental data, and production "system" acceptance test data Predicted BSE values from the model were consistently within ± 1 mRad of published surface integration results for hemispheric radome data and within ± .5 mRad of measured production system acceptance data, "excellent" results by previously established standards.

147

9.2 Recommendations

Four areas are recommended for extending the current work into future analysis and modeling efforts including, 1) using the developed multi-layer tapered radome model and calculated reflection results with a surface integration propagation technique, 2) a polarization sensitivity study to characterize BSE performance under varying polarization conditions, 3) validation of the "*ideal*" taper function concept with additional measured data, and 4) using the current analysis and modeling procedure to predict image lobe level and location. Each of these recommendations are addressed in the following paragraphs.

Hemispheric data presented in Figures 22 and 23 indicates a significant improvement in BSE estimation may be realized if current analysis and modeling procedures are implemented using surface integration propagation techniques. However, full implementation of such a technique will increase required processing time, possibly to an unacceptable level for developmental system analysis. A "hybrid" propagation technique should be considered to reduce the processing burden. From Figures 22 and 23 it is evident that the current ray-tracing development accurately predicts first-order BSE characteristics. Reflected E-Field components generally contribute to the higher-order "variations" present on predicted and measured BSE curves, "variations" which are most accurately predicted by surface integration techniques. Future studies should consider using a "hybrid" propagation technique to combine first-order ray-tracing and higher-order surface integration results into a composite BSE estimate, i.e., superimpose surface integration variations on ray-trace receive data. Excellent BSE prediction results are obtained if this procedure is

applied to data in Figures 22 and 23, indicating that a "hybrid" propagation technique may provide improved BSE estimates at processing speeds ranging between ray-tracing and surface integration processing rates. A theoretical basis for "hybrid" analysis and modeling should be established and validated if appropriate.

Polarization "purity" was maintained throughout analysis and model development of the current research effort, i.e., E-Field polarization responses were accurately accounted for along propagation paths. As a result, current results are well suited for polarization sensitivity analysis for varying polarization conditions. Arbitrarily polarized reference E-Fields, arbitrarily polarized aperture elements, independent co/cross-polarized processing channels, and accurate radome characterization are essential elements for accurately characterizing radome depolarization and BSE performance under varying polarization conditions. Previous polarization studies indicated that modulation of the reference E-Field polarization (vary the axial ratio or tilt angle) generally results in improved/degraded BSE performance depending on the specific "system" design. Results of such analyses would provide the radar and electronic countermeasure technical communities valuable insight into enhanced/degraded "system" performance. A polarization sensitivity study would also provide information on the level/amount of radome depolarization, as opposed to the "effects' of depolarization. The "effects" of radome depolarization on various system parameters have been extensively analyzed with few research efforts attempting to characterize the depolarization itself, i.e., establish the level/amount of polarization "difference" between incident and transmitted E-Fields. The analysis and modeling technique developed under this research effort provides intermediate results for

149

predicting/establishing radome depolarization levels. Improved range measurement techniques are required to provide reliable measured depolarization data. When available, a comparative analysis between predicted and measured data should be accomplished.

The "*ideal*" taper function concept developed in *Section 3.4.2* and implemented in *Section 8.5.3* required additional validation against measured BSE data. Specifically, an empirically "tuned" production radome design should be modified and built to include an "*ideal*" taper. Measured data from the two radome designs should then be analyzed and compared to determine the validity of the "*ideal*" taper function concept. Data presented in Figures 39 thru 41 suggests the "*ideal*" taper function approach may reduce the number of developmental "built-and-test" iterations required to obtain "near" optimum radome performance, potentially reducing radome development time and cost.

As depicted in Figure 4, reflected rays generally form an image lobe(s) anytime a significant amount of energy is reflected from the radome's inner surface. The relative level and location of the image lobe(s) provides an indication of "how well" the radome is performing. High image lobe levels indicated poor transmission qualities and image lobe location provides an estimate of where taper improvement is required. Accurate prediction of image lobe level and location would greatly aid in radome development efforts. Considering the ability to accurately calculate specular reflection points (*Chapter IV*) and far-field radiation patterns, the current modeling technique is ideally suited for future image lobe analysis. The current analysis and modeling technique should be extended to allow the reference E-Field

150

location to vary beyond the aperture field-of-view, allowing far-field radiation patterns to oe generated within ± 180° of the aperture scan direction. Modeled results would then be compared with measured image lobe data to validate the image lobe analysis procedure.

This appendix is provided to augment material presented in *Chapter IV, Radome Reflection Points*. It provides the detailed derivation procedures used in calculating special case critical points. Eqs (A.1) thru (A 8) are similar to expressions found in *Chapter IV* and are repeated here for completeness and clarity reasons. Eqs (A.1) and (A.2) represent the scaling process used for generating dimensionless distance and velocity quantities where R is the radome generating radius and v_m is the velocity of propagation in the medium.

$$\text{Defining}: \quad \bar{x}(\bar{t}) = \frac{x\left(\dfrac{v_m t}{R}\right)}{R} \ , \ \ \bar{y}(\bar{t}) = \frac{y\left(\dfrac{v_m t}{R}\right)}{R} \ , \ \ \bar{z}(\bar{t}) = \frac{z\left(\dfrac{v_m t}{R}\right)}{R} \tag{A.1}$$

$$\text{and} \quad \bar{a} = \frac{a}{v_m} \ , \ \ \bar{b} = \frac{b}{v_m} \ , \ \ \bar{c} = \frac{c}{v_m} \ . \ \ \bar{t} = \frac{v_m t}{R}$$

$$\textit{From \quad Boundary \quad Conditions}:$$

$$\bar{x}_1(\bar{t}) = \left(\frac{a}{v_m}\right)\left(\frac{v_m t}{R}\right) + \frac{x_r}{R} = \bar{a}\bar{t} + \bar{x}_r$$

$$\bar{y}_1(\bar{t}) = \left(\frac{b}{v_m}\right)\left(\frac{v_m t}{R}\right) + \frac{y_r}{R} = \quad + \bar{y}_r \tag{A.2}$$

$$\bar{z}_1(\bar{t}) = \left(\frac{c}{v_m}\right)\left(\frac{v_m t}{R}\right) + \frac{z_r}{R} = \bar{c}\bar{t} + \bar{z}_r$$

For the tangent ogive surface under consideration, Eq (A.3) provides the expression for the surface equations and scaled gradient components at the critical point. The scaled surface expression of Eq (A.3) and the three equations in Eq (A.4), in conjunction with the change of variable expressions of Eq (A.5), represent a system of four equations and four unknowns, the unknowns to be solved for are α, β, $\bar{\tau}_c$, and λ.

Scaled Surface Equation:

$$\frac{g(x,y,z)}{R} = 0 \quad \rightarrow \quad \sqrt{1 - \bar{z}^2} - \sqrt{\bar{x}^2 + \bar{y}^2} + \bar{K} = 0$$

$$where \quad \bar{K} = \frac{W}{2R} - 1 \tag{A.3}$$

$$\rightarrow \quad \bar{g}_{\bar{x}}\bigg|_{\bar{t}_c} = \frac{-\bar{x}_c}{\sqrt{\bar{x}_c^2 + \bar{y}_c^2}} \quad , \quad \bar{g}_{\bar{y}}\bigg|_{\bar{t}_c} = \frac{-\bar{y}_c}{\sqrt{\bar{x}_c^2 + \bar{y}_c^2}} \quad , \quad \bar{g}_{\bar{z}}\bigg|_{\bar{t}_c} = \frac{-\bar{z}_c}{\sqrt{1 - \bar{z}_c^2}}$$

From Velocity Conditions:

$$\left(\bar{a} - k_x\right) = \lambda \, \bar{g}_{\bar{x}}\left(\bar{x}_c, \bar{y}_c, \bar{z}_c\right)$$

$$\left(\bar{b} - k_y\right) = \lambda \, \bar{g}_{\bar{y}}\left(\bar{x}_c, \bar{y}_c, \bar{z}_c\right) \tag{A.4}$$

$$\left(\bar{c} - k_z\right) = \lambda \, \bar{g}_{\bar{z}}\left(\bar{x}_c, \bar{y}_c, \bar{z}_c\right)$$

$$\bar{a} = \sin\alpha\,\cos\beta \qquad where \quad 0 < \beta < 2\pi$$

$$\bar{b} = \sin\alpha\,\sin\beta \qquad and \quad 0 < \alpha < \frac{\pi}{2} \tag{A.5}$$

$$\bar{c} = \cos\alpha$$

As presented in *Chapter IV*, Eqs (A.6) and (A.7) are used for deriving critical point solutions for Case I where it is assumed that both $\widetilde{x}_c$ and $\widetilde{y}_c$ are non-zero. Two subcases emerged with Eq (A.8) representing the $\widetilde{\tau}_c$ solution for Case I.A, as derived in *Chapter IV*. The second sub-case, Case I.B, is further sub-divided into a series of cases, all of which cause the $\widetilde{\tau}_c$ expression of Eq (A.8) to be invalid, i.e., cause division by zero

$$For \quad Case \quad 1, \quad \tilde{x}_c \neq 0 \quad and \quad \tilde{y}_c \neq 0$$

$$\lambda = \frac{\left(\bar{a} - k_x\right)\sqrt{\tilde{x}_c^2 + \tilde{y}_c^2}}{\tilde{x}_c} = \frac{\left(\bar{b} - k_y\right)\sqrt{\tilde{x}_c^2 + \tilde{y}_c^2}}{\tilde{y}_c} = \frac{\left(\bar{c} - k_z\right)\sqrt{1 - \tilde{z}_c^2}}{\tilde{z}_c} \tag{A.6}$$

$$\frac{\bar{a} - k_x}{\tilde{x}_c} = \frac{\bar{b} - k_y}{\tilde{y}_c} \quad \rightarrow \quad \left(\bar{a} - k_x\right)\tilde{y}_c = \left(\bar{b} - k_y\right)\tilde{x}_c$$

$$where \quad \tilde{x}\left(\tilde{t}_c\right) = \bar{a}\tilde{t}_c + \tilde{x}_r \quad and \quad \tilde{y}\left(\tilde{t}_c\right) = \bar{b}\tilde{t}_c + \tilde{y}_r \tag{A.7}$$

$$\rightarrow \quad \tilde{t}_c\sin\alpha\left(k_y\cos\beta - k_x\sin\beta\right) = \tilde{x}_r\left(\sin\alpha\cos\beta - k_y\right) - \tilde{y}_r\left(\sin\alpha\cos\beta - k_x\right)$$

154

$$\textit{For Case I.A}: \quad \sin\alpha\left(k_y\cos\beta - k_x\sin\beta\right) \neq 0$$

$$\tilde{t}_c = \frac{\tilde{x}_r\left(\sin\alpha\,\sin\beta - k_y\right) - \tilde{y}_r\left(\sin\alpha\,\cos\beta - k_x\right)}{\sin\alpha\left(k_y\cos\beta - k_x\sin\beta\right)} \tag{A.8}$$

For Case I.B.1, it is assumed that $\sin(\alpha) = 0$. Eqs (A.9) thru (A.13) summarize the results of making this assumption. The goal is to establish a set of conditions, which when satisfied, result in $\sin(\alpha) = 0$ and provide an alternate solution to Case I.A. Eqs (A.10) thru (A.12) form such a set of conditions, which when satisfied, result in the critical point coordinates as given by Eq (A.9).

$$\textit{Case I.B 1: Suppose } \sin\alpha = 0$$

$$\textit{Then} \quad \tilde{a} = \sin\alpha\,\cos\beta = 0 \;\rightarrow\; \tilde{a} = 0 \;\rightarrow\; \tilde{x}_c = \tilde{x}_r \neq 0$$

$$\textit{and} \quad \tilde{b} = \sin\alpha\,\sin\beta = 0 \;\rightarrow\; \tilde{b} = 0 \;\rightarrow\; \tilde{y}_c = \tilde{y}_r \neq 0 \tag{A.9}$$

$$\tilde{a} = 0 \;\&\; \tilde{b} = 0 \;\rightarrow\; \tilde{c} = 1 \;\rightarrow\; \tilde{z}_c = \tilde{t}_c + \tilde{z}_r$$

$$\textit{From Equation A.6}: \quad \textit{"Condition \#1"}$$

$$\lambda = \frac{k_x\sqrt{\tilde{x}_r^2 + \tilde{y}_r^2}}{\tilde{x}_r} = \frac{k_y\sqrt{\tilde{x}_r^2 + \tilde{y}_r^2}}{\tilde{y}_r} < 0 \;\rightarrow\; \frac{k_x}{\tilde{x}_r} = \frac{k_y}{\tilde{y}_r} < 0 \tag{A.10}$$

From Eqns A.3 and A.4 : "Condition #2"

$$z_c^2 = \frac{\left(\bar{c} - k_z\right)^2}{\lambda^2 + \left(\bar{c} - k_z\right)^2} = \frac{1 - k_z}{2} = \left(\bar{t}_c + \bar{z}_r\right)^2 \quad \rightarrow \quad 0 < \bar{t}_c = \sqrt{\frac{1 - k_z}{2}} - \bar{z}_r < \bar{t}_{c(max)} \tag{A.11}$$

From Eqn A.3 with $\bar{x}_c = \bar{x}_r$ and $\bar{y}_c = \bar{y}_r$: "Condition #3"

$$z_c^2 = 1 - \left(\sqrt{\bar{x}_r^2 + \bar{y}_r^2} - \bar{K}\right)^2 = \frac{1 - k_z}{2} \quad \rightarrow \quad k_z = 2\left(\sqrt{\bar{x}_r^2 + \bar{y}_r^2} - \bar{K}\right)^2 - 1 \tag{A.12}$$

$$For \ \ \bar{t}_c = \frac{v_m t_c}{R} \ , \ \ l_{(max)} = L + \frac{W}{2} \ , \ \ and \ \ L = \sqrt{R^2 - \left(R - \frac{W}{2}\right)^2}$$

$$\bar{t}_{c(max)} = \frac{v_m}{R} t_{c(max)} = \frac{v_m}{R}\left(\frac{l_{max}}{v_m}\right) = \frac{L}{R} + \frac{W}{2R} \tag{A.13}$$

$$\rightarrow \quad 0 < \bar{t}_c < \bar{t}_{c(max)} = \frac{\left(\dfrac{L}{W}\right) + \dfrac{1}{2}}{\left(\dfrac{L}{W}\right) + \dfrac{1}{4}} \ \ "For \ All \ Cases"$$

To verify the condition expressed in Eq (A.11), it is first necessary to establish a maximum scaled critical time. This maximum time is based on the longest distance between any given antenna element and the tip of the radome. Assuming a maximum antenna scan angle of $\pi/2$ Rads, a worst case condition used only for calculation purposes, the maximum distance between an element and the radome tip

will be given by $l_{max} = L + W/2$. Using this relationship, Eq (A.13) shows the development process and final expression for the maximum scaled critical time.

For Case I.B.2 it is assumed that $k_y \cos\beta = k_x \sin\beta$, thereby causing the numerator of Eq (A.8) to go to zero. From Eq (A.4) it can be shown that for λ to be non-zero, k_z cannot equal one. Since $\hat{k}$ is a unit vector, this implies that k_x and k_y may not simultaneously equal zero and is therefore an invalid solution to the assumed condition. Further, it can be shown from Eq (A.4) that neither the condition that $k_x = \cos\beta = 0$ nor the condition that $k_y = \sin\beta = 0$ are possible solutions since both would result in λ equalling zero. Therefore, a solution exists only if all four terms of the assumed equation are non-zero. This being the case, β may be explicitly solved for as shown in Eq (A.14) and three special cases are considered as a result of the arctangent function.

$$\textit{For Case I.B 2}: \quad k_y \cos\beta = k_x \sin\beta$$

$$k_x \neq 0 \ , \ k_y \neq 0 \ , \ \cos\beta \neq 0 \ , \ \sin\beta \neq 0 \quad \rightarrow \quad \beta = \tan^{-1}\left(\frac{k_y}{k_x}\right) \tag{A.14}$$

$$\textit{For Case I.B.2.i}: \quad k_x = k_y$$

$$\rightarrow \quad \beta = \frac{\pi}{4} \ or \ \frac{-3\pi}{4} \quad \rightarrow \quad \bar{a} = \bar{b} \tag{A.15}$$

$$\therefore \ \frac{\bar{a} - k_x}{\bar{x}_c} = \frac{\bar{b} - k_y}{\bar{y}_c} \quad \rightarrow \quad \bar{x}_c = \bar{y}_c \quad \rightarrow \quad \bar{x}_r = \bar{y}_r$$

157

For Case I.B.2.i, k_x and k_y are assumed to be equal and Eq (A.6) is used to show that $\tilde{x}_r$ must equal $\tilde{y}_r$ as shown in Eq (A.15). For Case I.B.2.ii, k_x is assumed to be equal to $-k_y$ and Eq (A.6) is again used to show that this assumption results in $\tilde{x}_r$ being equal to $-\tilde{y}_r$ as indicated in Eq (A.16). For both of these cases, λ is solved for and equated to the right hand expression of Eq (A.6). The expression formed, which when combined with the surface constraint expression of Eq (A.3), forms the system of two equations and two unknowns ($\tilde{\tau}_c$ and α) shown in Eq (A.17). As for Case I.A, the system generated is composed of transcendental non-linear expressions requiring numerical solution techniques

$$\textit{For Case I.B.2.ii:} \quad k_x = -k_y$$

$$\rightarrow \quad \beta = -\frac{\pi}{4} \ or \ \frac{3\pi}{4} \tag{A.16}$$

$$\therefore \frac{\bar{a} - k_x}{\tilde{x}_c} = \frac{\bar{b} - k_y}{\tilde{y}_c} \quad \rightarrow \quad \tilde{x}_c = -\tilde{y}_c \quad \rightarrow \quad \tilde{x}_r = -\tilde{y}_r$$

$$\textit{Case I.B.2.i and Case I.B.2.ii Equations:}$$

$$\left(\cos\alpha \, \tilde{t}_c + \tilde{z}_r\right)^2 = \frac{\left(\cos\alpha - k_z\right)^2}{2\left[(\pm)\dfrac{\sin\alpha}{\sqrt{2}} - k_x\right]^2 + \left(\cos\alpha - \tilde{s}_z\right)^2}$$

$$\left(\cos\alpha \, \tilde{t}_c + \tilde{z}_r\right)^2 = 1 - \left[\sqrt{2}\left|(\pm)\dfrac{\sin\alpha}{\sqrt{2}} \, \tilde{t}_c - \tilde{x}_r\right| - \bar{K}\right]^2 \tag{A.17}$$

$$\textit{Take:} \quad (+) \ \textit{for} \ \beta = \pm\frac{\pi}{4} \quad , \quad (-) \ \textit{for} \ \beta = \pm\frac{3\pi}{4}$$

The final sub-case, Case I.B.2.iii, is for arbitrary values of k_x and k_y such that $k_x \neq +/- k_y$ and β is as given in Eq (A.14). For this value of β, the left-hand side of the final expression in Eq (A.7) identically equals zero. As such, the right-hand side equals zero and may be used to explicitly solve for α as given in Eq (A.18). With α and β both calculated, only $\tilde{T}_c$ remains unknown and may be determined using Eqs (A.2) and (A.3). Provided a $\tilde{T}_c$ value satisfying Eq (A.3) exists and satisfies the inequality specified in Eq (A.13), a critical point exists and its coordinates may be calculated via Eqs (A.2) and (A.5).

$$\text{For Case I.B 2.iii}: \quad k_x \neq k_y \ , \ \tilde{x}_r \neq 0 \ and \ \tilde{y}_r \neq 0$$

$$\alpha = \sin^{-1}\left\{\frac{\tilde{x}_r k_y - \tilde{y}_r k_x}{\tilde{x}_r \sin\beta - \tilde{y}_r \cos\beta}\right\} \quad for \quad 0 < \alpha < \cos^{-1}(k_z) \tag{A.18}$$

$$\text{For Case II}: \quad \tilde{x}_c = 0 \ \ and \ \ \tilde{y}_c \neq 0$$

$$\tilde{x}_c = 0 \ \ \rightarrow \ \ \tilde{g}_{\tilde{z}}\bigg|_{i_c} = \frac{-\tilde{x}_c}{\sqrt{\tilde{x}_c^2 + \tilde{y}_c^2}} = 0 \tag{A.19}$$

$$\therefore \ \tilde{a} - k_x = \lambda \tilde{g}_x\bigg|_{\tilde{r}_c} = 0 \ \ \rightarrow \ \ \tilde{a} = k_x \ \ \rightarrow \ \ \tilde{x}_c = k_x \tilde{t}_c + \tilde{x}_r = 0$$

For the second major case, Case II, it is assumed that $\tilde{x}_c = 0$ and $\tilde{y}_c \neq 0$. For $\tilde{x}_c = 0$ the partial derivative of the reflecting surface $g(x,y,z)$ with respect to x identically equals zero. As a result, only equality of the last two expressions of

159

Eq (A.6) remains valid and the velocity expression relating $\tilde{a}$ and k_x is used to establish the relationship shown in Eq (A.19). Two sub-cases are considered as a result of this relationship, Case II A for k_x equal zero and Case II.B for k_x not equal zero.

For Case II.A.1: $k_x = 0$ *and* $\sin\alpha = 0$

$$k_x = 0 \;\;\rightarrow\;\; \tilde{x}_r = 0 \quad \text{"Condition \#1"}$$

$$\sin\alpha = 0 \;\;\rightarrow\;\; \begin{cases} \tilde{b} = 0 \;\;\rightarrow\;\; \tilde{y}_c = \tilde{y}_r \\[2mm] \alpha = k\pi \;\;, \;\; k = 0, \pm 1, \pm 2, \ldots \end{cases} \quad\quad (A.20)$$

$$\therefore \; \tilde{c} = \cos\alpha = \pm 1 \quad but \quad \tilde{c} > k_z > 0 \;\;\rightarrow\;\; \tilde{c} = 1$$

From the Velocity Equations

$$\tilde{b} - k_y = \lambda \tilde{g}_{\tilde{y}}\Big|_{i_c} \;\;\rightarrow\;\; k_y = \lambda \frac{\tilde{y}_c}{\sqrt{\tilde{y}_c^2}} = \lambda\, sign\!\left(\tilde{y}_r\right) \quad\quad (A.21)$$

$$\lambda < 0 \;\;\rightarrow\;\; \begin{cases} k_y < 0 \;\; and \;\; \tilde{y}_r > 0 \\ or \\ k_y > 0 \;\; and \;\; \tilde{y}_r < 0 \end{cases} \quad \text{"Condition \#2"}$$

For $\tilde{a} = \sin\alpha\cos\beta = k_x = 0$, Case II.A is further subdivided into two special cases. Case II.A 1 provides solutions based on the assumption that either $\sin\alpha = 0$ or $\sin\alpha = \cos\beta = 0$ and Case II A 2 provides solutions based on $\cos\beta = 0$ only. Eqs (A.20) thru (A.22) summarize the results for Case II.A.1. The three conditions

$$For \quad \lambda = sign(\tilde{y}_r)k_y$$

$$\bar{c} - k_z = \lambda \tilde{g}_z \Big|_{\tilde{i}_c} \quad \rightarrow \quad \tilde{z}_c = \sqrt{\frac{1-k_z}{2}} \tag{A.22}$$

Into the Scaled Surface Equation

$$\rightarrow \quad \sqrt{\frac{1+k_z}{2}} - |\tilde{y}_r| + \bar{K} = 0 \quad \text{"Condition \#3"}$$

are derived by considering both the velocity equations and surface constraints as shown. Given all three conditions are satisfied, a critical point exists with coordinates $\tilde{x}_c = 0$, $\tilde{y}_c = \tilde{y}_r$, and $\tilde{z}_c$ as given by Eq (A.22).

For Case II.A.2 results are not as easily obtained as outlined in Eqs (A.23) thru (A.25). As with the previous case, the condition that $\tilde{x}_r = 0$ must again be satisfied. Under the assumption that $\cos\beta = 0$ and given the range of β values specified in Eq (A.5), only two β values are possible, $\pi/2$ and $3\pi/2$, as indicated in Eq (A.23). Solving for λ from the velocity equations allows for $\tilde{\tau}_c$ to be explicitly solved for as a function of α as indicated in Eq (A.24).

$$For \quad Case \ II.A.2: \quad k_x = 0 \quad and \quad \cos\beta = 0$$

$$k_x = 0 \quad \rightarrow \quad \tilde{x}_r = 0 \quad \text{"Condition \#1"}$$

$$\cos\beta = 0 \quad \rightarrow \quad \sin\beta = (\pm)1 \quad \rightarrow \quad \beta = \pm\frac{\pi}{2} \tag{A.23}$$

$$\rightarrow \quad \tilde{b} = \sin\alpha \sin\beta = (\pm)\sin\alpha$$

Introducing the function f(α), the $\tilde{\tau}_c$ expression is substituted into the scaled surface equation resulting in the final expression shown in Eq (A.25), a single expression of one variable α. Provided an α exists which satisfies this expression, $\tilde{\tau}_c$ can be calculated from Eq (A.24) and the critical point coordinates determined via Eq (A.2).

From Velocity Equations

$$\tilde{b} - k_y = \lambda \tilde{g}_{\tilde{y}}\Big|_{\tilde{t}_c} \quad \leftrightarrow \quad \lambda = sign(\tilde{y}_c)\big[k_y \mp \sin\alpha\big]$$

$$\tilde{c} - k_z = \lambda \tilde{g}_{\tilde{t}}\Big|_{\tilde{t}_c} \rightarrow \tilde{z}_c^2 = \frac{\big(k_z - \cos\alpha\big)^2}{\big[k_y(\mp)\sin\alpha\big]^2 + \big(k_z - \cos\alpha\big)^2} = \big(\cos\alpha\,\tilde{t}_c + \tilde{z}_r\big)^2 \quad \text{(A.24)}$$

$$\rightarrow \quad 0 < \tilde{t}_c = \frac{1}{\cos\alpha}\left\{ \frac{\big(k_z - \cos\alpha\big)}{\sqrt{\big(k_y \mp \sin\alpha\big)^2 + \big(k_z - \cos\alpha\big)^2}} - \tilde{z}_r \right\} < \tilde{t}_{c(max)}$$

From Scaled Surface Equation:

$$Letting. \quad f(\alpha) = \frac{\big(k_z - \cos\alpha\big)}{\sqrt{\big(k_y \mp \sin\alpha\big)^2 + \big(k_z - \cos\alpha\big)^2}}$$

$$then \quad \tilde{t}_c = \frac{1}{\cos\alpha}\big[f(\alpha) - \tilde{z}_r\big] \quad and \quad \tilde{z}_c^2 = f^2(\alpha) \quad \text{(A.25)}$$

$$\rightarrow \quad \sqrt{1 - f^2(\alpha)} - \big|(\pm)\tan\alpha\big[f(\alpha) - \tilde{z}_r\big] + \tilde{y}_r\big| + \tilde{K} = 0$$

$$For \quad 0 < \alpha < \cos^{-1}\big(k_z\big)$$

For Case II.B k_x is assumed to be non-zero. As a result, the final expression of Eq (A.19) is used to explicitly solve for $\tilde{\tau}_c$, leading to test Condition #1 shown in Eq (A.26). Also, $\tilde{a} = k_x$ implies that β can be explicitly solved for and the range of possible α values restricted as shown in Eq (A.27)

$$For\ \ Case\ \ II.B: \quad \tilde{x}_c = 0 \ , \ \tilde{y}_c \neq 0 \quad and \quad k_x \neq 0$$

$$k_x \tilde{t}_c + \tilde{x}_r = 0 \quad \rightarrow \quad \tilde{t}_c = \frac{-\tilde{x}_r}{k_x} \tag{A.26}$$

$$where \quad 0 < \tilde{t}_c < \tilde{t}_{c(max)} \quad \rightarrow \quad \frac{-\tilde{x}_r}{k_x} > 0 \quad \text{"Condition #1"}$$

$$Since \quad \tilde{a} = k_x = \sin\alpha\cos\beta \neq 0$$

$$then \quad \beta = \cos^{-1}\left(\frac{k_x}{\sin\alpha}\right) \quad \rightarrow \quad \left|\frac{k_x}{\sin\alpha}\right| \leq 1 \tag{A.27}$$

$$for \quad 0 < \alpha < \cos^{-1}(k_z) \quad \rightarrow \quad \sin^{-1}(|k_x|) < \alpha < \cos^{-1}(k_z)$$

$$From:\ Scaled\ \ Surface\ \ Equation:$$

$$\sqrt{1 - \left(\frac{-\tilde{x}_r}{k_x}\cos\alpha + \tilde{z}_r\right)^2} - \left|\frac{-\tilde{x}_r}{k_x}\sin\alpha\sin\left\{\cos^{-1}\left(\frac{k_x}{\sin\alpha}\right)\right\} + \tilde{y}_r\right| + \bar{K} = 0 \tag{A.28}$$

The derived expressions for β and $\tilde{\tau}_c$ are next substituted into the scaled surface equation resulting in an expression involving only α as shown in Eq (A.28). Provided

163

an α value exists which satisfies this expression, two additional conditions must be satisfied before declaring the existence of a valid critical point. After calculating the critical point coordinates using the previously derived values of α, β, and $\tilde{\tau}_c$, a check must be made to ensure the velocity equations are satisfied. In doing so, λ is first calculated and checked to ensure it is negative. The right hand equality of Eq (A.6) is then used to ensure the velocity equations are satisfied for the calculated λ value. These checks, identified as Conditions #2 and #3 in Eq (A.29), if satisfied ensure the critical point coordinates calculated are valid.

$$Provided \quad \alpha \quad , \quad \beta \quad and \quad \bar{\tau}_c \quad exist:$$

$$\lambda = sign(\bar{y}_c)(k_y - \sin\alpha\sin\beta) < 0 \quad \text{"Condition #2"}$$

$$then \quad (\bar{b} - k_y)sign(\bar{y}_c) = \frac{(\bar{c} - k_z)\sqrt{1 - \bar{z}^2}}{\bar{z}_c} \qquad (A.29)$$

$$\rightarrow \quad \bar{z}_c^2 = \frac{(\cos\alpha - k_z)^2}{(k_y - \sin\alpha\sin\beta)^2 + (\cos\alpha - k_z)^2} \quad \text{"Condition #3"}$$

For the last major case to be considered, Case III, it is assumed that $\tilde{x}_c \neq 0$ and $\tilde{y}_c = 0$ and the derivation procedure parallels the process previously used for Case II. Since $\tilde{y}_c = 0$, the partial derivatives of $g(x,y,z)$ with respect to y vanishes. As such, only equality of the first and last expressions of Eq (A.6) is valid and the velocity expression involving $\bar{b}$ and k_y is used to establish the relationship shown in Eq (A.30).

Two subcases are considered as a result of this relationship, Case III.A for k_y equal to zero and Case III.B for k_y not equal to zero. For $\bar{b} = \sin\alpha\sin\beta = k_y = 0$, Case III.A is further subdivided into two special cases. Case III.A.1 provides solutions on $\sin\alpha = 0$ or both $\sin\alpha = 0$ and $\cos\beta = 0$, and Case III.A.2 provides solutions based on $\cos\beta = 0$ only. Eqs (A.31) thru (A.33) summarize the results for Case III.A.1. The three conditions shown are derived by considering both the velocity equations and surface constraint equation as shown. Given all three conditions are satisfied, a critical point exists at $\tilde{x}_c = \tilde{x}_r$, $\tilde{y}_c = 0$, and $\tilde{z}_c$ as given by Eq (A.33).

$$\textit{For Case III}: \quad \tilde{x}_c \neq 0 \quad \textit{and} \quad \tilde{y}_c = 0$$

$$\tilde{y}_c = 0 \;\rightarrow\; \bar{g}_{\tilde{y}}\Big|_{\tilde{t}_c} = \frac{-\tilde{y}_c}{\sqrt{\tilde{x}_c^2 + \tilde{y}_c^2}} = 0 \tag{A.30}$$

$$\therefore\; \bar{b} - k_y = \lambda \bar{g}_{\tilde{y}}\Big|_{\tilde{t}_c} = 0 \;\rightarrow\; \bar{b} = k_y \;\rightarrow\; \tilde{y}_c = k_y \tilde{t}_c + \tilde{y}_r = 0$$

$$\textit{For Case III.A.1}: \quad k_y = 0 \quad \textit{and} \quad \sin\alpha = 0$$

$$k_y = 0 \;\rightarrow\; \tilde{y}_r = 0 \quad \textit{"Condition \#1"}$$

$$\sin\alpha = 0 \;\rightarrow\; \begin{cases} \bar{a} = 0 \;\rightarrow\; \tilde{x}_c = \tilde{x}_r \\ \alpha = k\pi \quad, \quad k = 0, \pm 1, \pm 2, \ldots \end{cases} \tag{A.31}$$

$$\therefore\; \bar{c} = \cos\alpha = \pm 1 \quad \textit{but} \quad \bar{c} > k_z > 0 \;\rightarrow\; \bar{c} = 1$$

From The Velocity Equations:

$$\tilde{a} - k_x = \lambda \tilde{g}_{\tilde{x}}\bigg|_{i_c} \quad \rightarrow \quad k_x = \lambda \frac{\tilde{x}_c}{\sqrt{\tilde{x}_c^2}} - \lambda \, sign\left(\tilde{x}_r\right)$$

(A.32)

$$\lambda < 0 \quad \rightarrow \quad \begin{cases} k_x < 0 \;\; and \;\; \tilde{x}_r > 0 \\ \qquad\quad or \\ k_x > 0 \;\; and \;\; \tilde{x}_r < 0 \end{cases} \quad \text{"Condition \#2"}$$

For $\lambda = sign\left(\tilde{x}_r\right)k_x$

$$\tilde{c} - k_z = \lambda \tilde{g}_{\tilde{z}}\bigg|_{i_c} \quad \rightarrow \quad \tilde{z}_c = \sqrt{\frac{1-k_z}{2}}$$

(A.33)

Into the Scaled Surface Equation

$$\rightarrow \quad \sqrt{\frac{1+k_z}{2}} - \left|\tilde{x}_r\right| + \overline{K} = 0 \quad \text{"Condition \#3"}$$

For Case III A 2, a detailed development procedure which parallels the process used for Case II A.2 is required to obtain critical point solutions. Eqs (A.34) thru (A.36) summarize results of the development process. As with the previous case, the condition that $\tilde{y}_r = 0$ must again be satisfied. Under the assumption that $\sin\beta = 0$ and given the range of β values specified in Eq (A.5), only two β values are possible, 0 and π, as indicated in Eq (A 34). Solving for λ from the velocity equations allows for $\tilde{\tau}_c$ to be explicitly solved for as a function of α as indicated in Eq (A.35). Introducing the function $f(\alpha)$, the $\tilde{\tau}_c$ expression is substituted into the

scaled surface equation resulting in the final expression shown in Eq (A.36), a single expression of one variable α. Provided an α exists satisfying this expression, $\bar{t}_c$ can be calculated from Eq (A.35) and the critical point coordinates determined via Eq (A.2).

$$For \ Case \ III.A \ 2: \quad k_y = 0 \quad and \quad \sin\beta = 0$$

$$k_y = 0 \quad \rightarrow \quad \bar{y}_r = 0 \quad "Condition \ \#1"$$

$$\sin\beta = 0 \quad \rightarrow \quad \cos\beta = (\pm)1 \quad \rightarrow \quad \beta = 0 \ or \ \pi \tag{A.34}$$

$$\rightarrow \quad \bar{a} = \sin\alpha \cos\beta = (\pm)\sin\alpha$$

$$From \ Velocity \ Equations:$$

$$\bar{a} - k_x = \lambda \bar{g}_x \bigg|_{i_c} \quad \rightarrow \quad \lambda = sign(\bar{x}_c)\left[k_x \mp \sin\alpha\right]$$

$$\bar{c} - k_z = \lambda \bar{g}_z \bigg|_{i_c} \quad \rightarrow \quad \bar{z}_c^2 = \frac{\left(k_z - \cos\alpha\right)^2}{\left[k_x(\mp)\sin\alpha\right]^2 + \left(k_z - \cos\alpha\right)^2} = \left(\cos\alpha \, \bar{t}_c + \bar{z}_r\right)^2 \tag{A.35}$$

$$\rightarrow \quad 0 < \bar{t}_c = \frac{1}{\cos\alpha}\left\{-\frac{\left(k_z - \cos\alpha\right)}{\sqrt{\left(k_x \mp \sin\alpha\right)^2 + \left(k_z - \cos\alpha\right)^2}} - \bar{z}_r\right\} < \bar{t}_{c(max)}$$

For Case III.B k_y is assumed to be non-zero. As a result, the final expression of Eq (A.30) is used to explicitly solve for $\bar{t}_c$, leading to test Condition #1 shown in Eq (A.37) Also, $\bar{b} = k_y$ implies that β can be explicitly solved for and the range of possible α values restricted as shown in Eq (A.38).

167

From Scaled Surface Equation:

$$\text{Letting}. \quad f(\alpha) = \frac{\left(k_z - \cos\alpha\right)}{\sqrt{\left(k_x \mp \sin\alpha\right)^2 + \left(k_z - \cos\alpha\right)^2}}$$

$$\text{then} \quad \bar{t}_c = \frac{1}{\cos\alpha}\left[f(\alpha) - \bar{z}_r\right] \quad \text{and} \quad \bar{z}_c^2 = f^2(\alpha) \tag{A.36}$$

$$\rightarrow \quad \sqrt{1 - f^2(\alpha)} - \left|(\pm)\tan\alpha\left[f(\alpha) - \bar{z}_r\right] + \bar{x}_r\right| + \bar{K} = 0$$

$$\text{For} \quad 0 < \alpha < \cos^{-1}\left(k_z\right)$$

For Case III.B: $\quad \bar{x}_c \neq 0 \; , \; \bar{y}_c = 0 \; and \; k_y \neq 0$

$$k_y \bar{t}_c + \bar{y}_r = 0 \quad \rightarrow \quad \bar{t}_c = \frac{-\bar{y}_r}{k_y} \tag{A.37}$$

$$\text{where} \quad 0 < \bar{t}_c < \bar{t}_{c(\max)} \quad \rightarrow \quad \frac{-\bar{y}_r}{k_y} > 0 \quad \text{"Condition \#1"}$$

Since: $\quad \bar{y} = k_y = \sin\alpha \sin\beta \neq 0$

$$\text{then} \quad \beta = \sin^{-1}\left(\frac{k_y}{\sin\alpha}\right) \quad \rightarrow \quad \left|\frac{k_y}{\sin\alpha}\right| \leq 1 \tag{A.38}$$

$$\text{for} \quad 0 < \alpha < \cos^{-1}\left(k_z\right) \quad \rightarrow \quad \sin^{-1}\left(\left|k_y\right|\right) < \alpha < \cos^{-1}\left(k_z\right)$$

The derived expressions for β and $\bar{t}_c$ are next substituted into the scaled surface equation resulting in an expression involving only α as shown in Eq (A.39). Provided an α value exists which satisfies this expression, two additional conditions must be

satisfied before declaring the existence of a valid critical point. After calculating the critical point coordinates using the previously derived values of α, β, and $\tilde{\tau}_c$, a check must be made to ensure the velocity equations are satisfied. In doing so, λ is first calculated and checked to ensure it is negative. The left-hand and right-hand expressions of Eq (A.6) are equated and used to ensure the velocity equations are satisfied for the calculated λ value. These checks, identified as Conditions #2 and #3 in Eq (A.4), if satisfied ensure the critical point coordinates calculated are valid.

$$From \quad Scaled \quad Surface \quad Equation:$$

$$\sqrt{1 - \left(\frac{-\tilde{y}_r}{k_y} \cos\alpha + \tilde{z}_r \right)^2} - \left| \frac{-\tilde{y}_r}{k_y} \sin\alpha \cos\left\{ \sin^{-1}\left(\frac{k_y}{\sin\alpha} \right) \right\} + \tilde{x}_r \right| + \bar{K} = 0 \tag{A.39}$$

$$Provided \quad \alpha \quad, \quad \beta \quad and \quad \tilde{t}_c \quad exist:$$

$$\lambda = sign(\tilde{x}_c)(k_x - \sin\alpha\cos\beta) < 0 \quad \text{"Condition #2"}$$

$$then \quad (\tilde{a} - k_x)sign(\tilde{z}_c) = \frac{(\tilde{c} - k_z)\sqrt{1 - \tilde{z}^2}}{\tilde{z}_c} \tag{A.40}$$

$$\rightarrow \quad \tilde{z}_c^2 = \frac{(\cos\alpha - k_z)^2}{(k_x - \sin\alpha\cos\beta)^2 + (\cos\alpha - k_z)^2} \quad \text{"Condition #3"}$$

Mechanical scanning of a planar phased-array is considered in this appendix. Mechanical scanning is employed as a *"simple"* method for varying the main beam pointing direction while maintaining a relatively symmetrical radiation pattern; typically not the case for electronic beam steering via phase tapering across the elements. As such, mechanical steering may potentially reduce/isolate some monopulse boresight errors being considered during analysis. Given the desire to scan the antenna main beam to an arbitrary location, the task at hand is to determine the scanned location of all elements within the array relative to the spherical coordinate origin, the point about which the antenna array pivots. The goal is to derive simplified mathematical expressions for the rotated/scanned element coordinates in spherical form, negating the need to perform a more computationally intense rectangular coordinate rotation followed by a rectangular-to-spherical conversion, a process which would be required for each antenna element at each desired scan angle.

$$x_r = x\,(\cos^2\phi_0\cos\theta_0 + \sin^2\phi_0) - y\cos\phi_0\sin\phi_0\,(1 - \cos\theta_0)$$

$$y_r = -x\cos\phi_0\sin\phi_0\,(1 - \cos\theta_0) + y\,(\sin^2\phi_0\cos\theta_0 + \cos^2\phi_0) \qquad (B.1)$$

$$z_r = -x\cos\phi_0\sin\theta_0 - y\sin\phi_0\sin\theta_0$$

Previous mechanical scanning derivations typically generated and utilized rectangular coordinate rotation equations to arrive at expressions for the rotated

element locations. The rotated rectangular coordinates given by Eq (B.1) are an example of the type of expressions usually derived, where θ_o is the antenna scan angle from the z-axis in the ϕ_o direction as measured from the positive x-axis [12].

From Eq (B.1) it is readily apparent that use of these equations to determine the rotated element locations in spherical coordinates is computationally intense, requiring four trigonometric function calculations, two squaring operations, in excess of fifteen multiplications, additions, and/or subtractions, as well as, invocation of a rectangular-to-spherical conversion routine. The computational intensity is further compounded when considering two additional factors. First, the calculations may be required for antenna arrays which typically are composed of 100 or more antenna elements. Second, scanning the antenna array in one plane may itself require calculations to be carried out for a large number of discrete antenna scan angles, possibly requiring 100 or more to obtain accurate, reliable, and consistent output data. As such, minimizing the computational burden while increasing efficiency is the key motivating force behind the following discussion.

Detailed information is provided on the derivation process used in developing the final equations for determining the rotated antenna element locations in spherical coordinates. In developing the equations, the aperture is initially assumed to be located in the x-y plane. The aperture is rotated/scanned about the origin to an angle θ_o from the z-axis in a direction specified by ϕ_o from the positive x-axis (this convention is consistent with the convention used in establishing the expressions of Eq (B.1). For any given antenna element, initially located at the point $(r_c, \pi/2, \phi_c)$ in spherical coordinates, a final element location is required and will be specified by

171

the coordinates (r_r,θ_r,ϕ_r) after rotation/scanning. For the specified coordinate system, the following variable ranges are defined. $r_e > 0$, $0 \leq \theta_o \leq \pi/2$, $0 \leq \theta_e$, $\theta_r \leq \pi$, and $-\pi < \phi_e, \phi_r, \phi_o \leq \pi$. The restriction on the maximum scan angle of $\theta_o = \pi/2$ results from considering only scan angles such that rays emanating normal to the aperture surface intersect the radome surface under consideration.
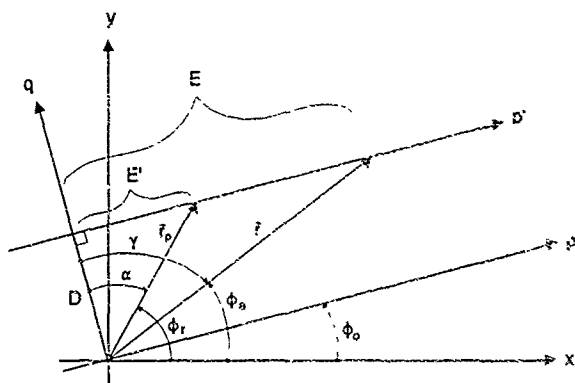
Figure B 1 Case I Scanning Geometry, $\phi_o < \phi_e < \phi_o + \pi$

The development process proceeds by considering two special cases which are distinguishable by the value of ϕ_e relative to ϕ_o for a given antenna element. Case I applies to all antenna elements where $\phi_o < \phi_e < \phi_o + \pi$ and Case II applies to all elements where $\phi_o - \pi < \phi_e < \phi_o$. The geometry established for considering each case is as illustrated in Figures B.1 and B 3 for Case I and Case II, respectively. For both of these figures, the following definitions are made.

172

p = axis perpendicular to the z-axis located ϕ_o from the x-axis

q = axis perpendicular to the z-axis and p-axis about which rotation by θ occurs

p' = axis parallel to p along which the tip of $\vec{r}_p$ follows as θ_o varies

$\vec{r}_p$ = vector "*projection*' of $\vec{r}$ in the x-y plane for a specified θ_o value

D = distance from the origin to p' as measured along the q-axis
(Note that $D = r_{p(min)}$ which occurs for $\theta_o = \pi/2$)

E = distance from the q-axis to the tip of $\vec{r}$ as measured along the p'-axis

E' = distance from the q-axis to the tip of $\vec{r}'_p$ as measured along the p'-axis

α = angle measured from q-axis to $\vec{r}_p$

γ = angle measured from q-axis to $\vec{r}$

The distance E' is established by observing that variation in θ_o from 0 to $\pi/2$ causes $\vec{r}$ to rotate about the q-axis in a clockwise direction as viewed in the $+q$ direction. In doing so, the tip of $\vec{r}$ traces out a quarter-circle in the z-p' plane as shown in Figure B.2. The quarter-circle generated will lie either in the "*lower-half*" of the z-p' plane, the case shown in Figure B.2 for $\phi_o - \pi/2 < \phi_e < \phi_o + \pi/2$, or in the "*upper-half*" of the z-p' plane which occurs when $\phi_o - \pi < \phi_e < \phi_o - \pi/2$ or $\phi_o + \pi < \phi_e < \phi_o + \pi/2$. In either case, the tip of "*projection*" $\vec{r}_p$ lies on the p'-axis at a distance of $E' = E\cos(\theta_o)$ from the q-axis. The "*upper-half*"/"*lower-half*" relationship of the quarter-circle will be taken into consideration later when developing an expression for θ_r. With all geometric relationships established and the quantities r_e, ϕ_e, ϕ_o, and θ_o given, the derivation process for computing ϕ_r for Case I proceeds as follows.

173
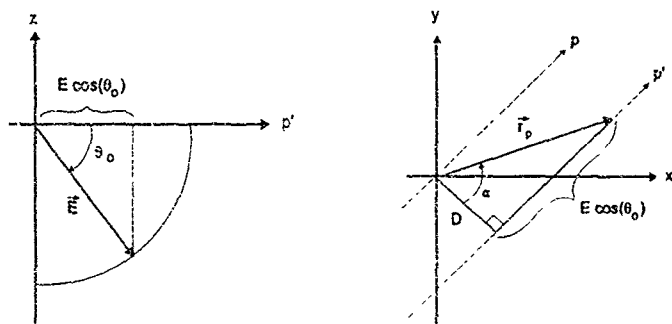
Figure B.2 Geometry For Establishing $E_o \cos(\theta_o)$ Quantity

For Case I Eqs (B.2) thru (B.4) were developed by considering the geometry established in Figure B.1. With the quantities γ, D, and E determined an expression for α is calculated by considering the geometry presented in Figure B.2. The α expression, given by Eq (B.5), is used in conjunction with the geometry established in Figure B.2 to obtain the rotated scanned ω, expression as given by Eq (B.6)

$$ \gamma = -\frac{\pi}{2} \quad \Psi_e - \Phi \tag{B.2} $$

$$ D = -\cos(\quad)\sin(\quad -\Phi \tag{B.3} $$

$$E = |\bar{r}_e| \sin(\gamma) = -|\bar{r}_e| \cos(\phi_e - \phi_o) \qquad \text{(B.4)}$$

$$\alpha = \tan^{-1}\left(\frac{E'}{D}\right) = \tan^{-1}\left(\frac{E\cos(\theta_0)}{D}\right) = \tan^{-1}\left\{\frac{-\cos(\phi_e - \phi_o)\cos(\theta_o)}{\sin(\phi_e - \phi_o)}\right\} \qquad \text{(B.5)}$$

$$\phi_r = \phi_o + \frac{\pi}{2} + \alpha = \phi_0 + \frac{\pi}{2} + \tan^{-1}\left\{\frac{-\cos(\phi_e - \phi_o)\cos(\theta_o)}{\sin(\phi_e - \phi_o)}\right\} \qquad \text{(B.6)}$$

$$For \quad \phi_o < \phi_e < \phi_o + \pi$$

The process used in deriving the ϕ_r expression for Case I is next applied for Case II, $\phi_o - \pi < \phi_e < \phi_o$, with geometrical relationships as established in Figure B.3 Eqs (B.7) thru (B.10) summarize the results of applying the procedure over this region with the final ϕ_r expression given by Eq (B.11). The observation is made that Eqs (B.6) and (B.1.. ary only in the + - sign preceding the $\pi/2$ quantity, and the minus sign or either the numerator or denominator of the arctangent argument. Applying the arctangent property given in Eq (B.12) to Eq B.1.., it can be shown th Eqs (B.6) a ... are actual identical expressions. Therefore regardless of the relationship betw. . n the ϕ_r ... her equation can be used to calculate the final ϕ_r for the antenna element under consideration

$$\frac{\tilde{}}{2} \quad \alpha \quad \circ_o \qquad \qquad \text{B.}$$

$$D = |\vec{r}_e| \sin(\gamma) = -|\vec{r}_e| \cos(\phi_e - \phi_o) \qquad (B.8)$$

$$E = |\vec{r}_e| \sin(\gamma) = |\vec{r}_e| \cos(\phi_e - \phi_o) \qquad (B.9)$$

$$\alpha = \tan^{-1}\left(\frac{E'}{D}\right) = \tan^{-1}\left(\frac{E\cos(\theta_o)}{D}\right) = \tan^{-1}\left\{\frac{\cos(\phi_e - \phi_o)\cos(\theta_o)}{-\sin(\phi_e - \phi_o)}\right\} \qquad (B.10)$$
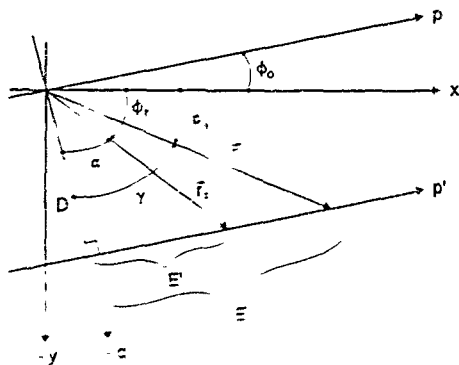

Figure B.5 Case II Scanning Geometry $-\pi < \phi_e < \phi_o$

$$\phi_r = \phi_o - \frac{\pi}{2} + \alpha = \phi_c - \frac{\pi}{2} + \tan^{-1}\left\{\frac{\cos(\phi_e - \phi_o)\cos(\theta_o)}{-\sin(\phi_e - \phi_o)}\right\} \qquad \text{(B.11)}$$

$$\text{For} \quad \phi_o - \pi < \phi_e < \phi_o$$

$$\tan^{-1}\left(\frac{+A}{-B}\right) = \tan^{-1}\left(\frac{-A}{+B}\right) + \pi \qquad \text{(B.12)}$$

$$\begin{aligned}
|\vec{r}_p| &= \sqrt{D^2 + E^2\cos^2(\theta_o)} \\
&= \sqrt{|\vec{r}_e|\sin^2(\phi_e - \phi_o) + |\vec{r}_e|\cos^2(\phi_e - \phi_o)\cos^2(\theta_o)} \qquad \text{(B.13)} \\
&= |\vec{r}_e|\sqrt{1 - \cos^2(\phi_e - \phi_o)\sin^2(\theta_o)}
\end{aligned}$$

The next task is to calculate θ_r, the rotated/scanned θ value of the antenna element being considered. The first step in determining θ_r is to calculate the magnitude of $\vec{r}_p$. Referring to Figure B 2, the magnitude of $\vec{r}_p$ is obtained by applying Pythagorean's Theorem to the triangle shown, resulting in the final expression as given by Eq (B.13). This magnitude expression is valid for each of the two cases previously considered, regardless of the relationship between ϕ_e and ϕ_c.

Using this magnitude expression, the plane containing $\vec{r}_p$ and $\vec{r}$ is considered to calculate $\Delta\theta_e$, the change in the antenna element's θ component resulting from rotation by θ_o about the ζ-axis. Considering this plane, the expression for $\Delta\theta_e$ is obtained as given by Eq (B.14) This equation is based on the fact that the

magnitude of $\vec{r}$ remains unchanged throughout the rotation/scanning process i.e. $|\vec{r}_p| = |\vec{r}|$, since the aperture pivots about the origin

$$\cos(\Delta\theta_e) = \frac{|\vec{r}_p|}{\vec{r}_e}$$

$$\Rightarrow \quad \Delta\theta_e = \cos^{-1}\left(\frac{|\vec{r}_p|}{|\vec{r}_e|}\right) = \cos^{-1}\left(\right.$$
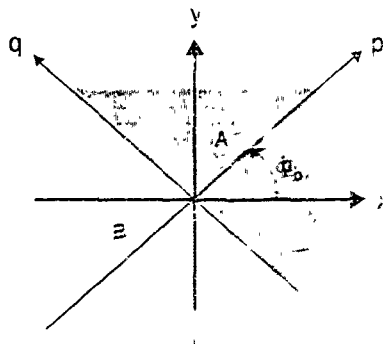
Figure B.4 Regions For Determining Addition/Subtraction of Angle

As mentioned previously, the rotation of $\vec{r}$ about the q-axis as θ_o varies from 0 to $\pi/2$ produces a quarter-circle which lies either in the "upper-half" or "lower-half" of the z-p' plane. This "upper-half"/"lower-half" relationship determines whether the value of $\Delta\theta_e$ given by Eq (B 14) is to be subtracted from or added to the initial θ_e value. Since all antenna elements are in the xy-plane prior to rotation, their initial θ_e component is equal to $\pi/2$. Therefore, an element's rotated value is simply

$-\pi/2 \pm \Delta\theta_e$. The question is, "When should $\Delta\theta_e$ be added or subtracted?". To answer this question consider the diagram shown in Figure B.4. Three separate cases exist as determined by the antenna element's initial ϕ_e value relative to ϕ_o.

For antenna elements located in Region A, including the positive p-axis, the tip of $\vec{r}$ traces out a quarter-circle lying in the "*lower-half*" of the z-p' plane; for this region $\theta_r = \pi/2 + \Delta\theta_e$. For antenna elements located in Region B, including the negative p-axis, the tip of $\vec{r}$ traces out a quarter-circle lying in the "*upper-half*" of the z-p' plane, for this region $\theta_r = \pi/2 - \Delta\theta_e$. Lastly, points located on the q-axis do not experience any change in θ value, in this case $\theta_r = \theta_e = \pi/2$. Considering these cases, a final expression for θ_r is obtained and may be summarized as given by Eq. B.15.

$$\theta_r = \frac{\pi}{2} \begin{matrix} (+) \\ (-) \end{matrix} \cos^{-1}\left\{ \sqrt{1 - \overline{\cos^2(\phi_e - \phi_o)\sin^2(\theta_o)}} \right\}$$

(B.15)

$$Take \begin{cases} (+) & for \quad 0 \le |\phi_e - \phi_o| \le \frac{\pi}{2} \\ (-) & for \quad \frac{\pi}{2} \le |\phi_e - \phi_o| \le \pi \end{cases} \quad where \quad -\pi < \phi_e - \phi_c \le \pi$$

179

Electronic scanning of a planar phased array is considered in this appendix. A phased array aperture is an antenna whose main beam maximum direction or pattern shape is primarily controlled by the relative phase of the element excitation currents on the array [13]. Assuming the elements and array feed network form a passive reciprocal structure, the phased array will exhibit identical far-field patterns both transmission and receptions modes [14]. The following development is based on a receive formulation, consistent with monopulse receiver tracking requirements.
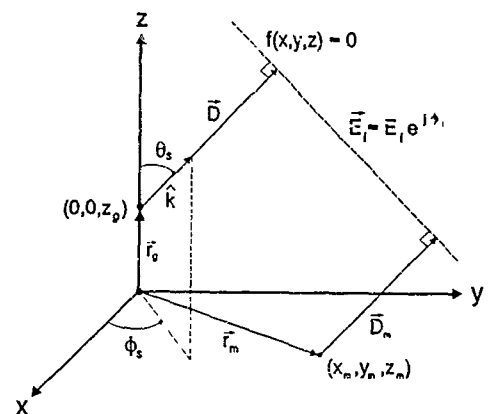

Figure C.1 Aperture Electrical Scanning Geometry

In developing expressions for the phase weight $\phi_w(m)$ of an arbitrary array element located at (x_m, y_m, z_m), far-field conditions are assumed As such, the E-Field incident on the array is considered to be a Uniform Plane Wave (UPW) As

established in Figure C.1, the UPW surface is given by $f(x,y,z) = 0$ with the plane wave itself being specified by $\vec{E}_i$. Additional vector quantities identified in Figure C.1 are defined as follows:

$\vec{E}_o$ = Incident E-Field at gimbal point $(0,0,z_g)$

$\vec{E}_m$ = Incident E-Field at m^{th} element location (x_m, y_m, z_m)

$\vec{D}$ = Vector from gimbal point to reference plane

$\vec{D}_m$ = Vector from element location to reference plane

$\vec{r}_g$ = Vector from coordinate origin to gimbal point

$\vec{r}_m$ = Vector from coordinate origin to m^{th} array element

Letting θ_s and ϕ_s represent the spherical coordinate angles which define the desired aperture scan direction, unit direction vector $\hat{k}$ is formed as indicated in Eq (C.1). Since $\hat{k}$ represents the direction from which the aperture response is desired to be a maximum, a UPW incident from this direction is considered. This condition dictates that $\nabla f(x,y,z) = \hat{k}$ for all (x_f, y_f, z_f) on the reference surface. The resulting expression for the reference surface is as given by Eq (C.2).

$$\text{Given} \quad \theta_s \quad \text{and} \quad \phi_s,$$
$$\hat{k} = k_x \hat{x} + k_y \hat{y} + k_z \hat{z} = \sin\theta_s \cos\phi_s \hat{x} + \sin\theta_s \sin\phi_s \hat{y} + \cos\theta_s \hat{z} \tag{C.1}$$

$$\text{For} \quad \nabla f(x,y,z) = \hat{k}$$
$$f(x,y,z) \quad k_x x + k_y y + k_z z + C \tag{C.2}$$

The unknown C in Eq (C.2) is solved for by noting that the vector sum of $\vec{r}_g$

181

and $\vec{D}$ must lie on the reference surface. This constraint allows for the value of C to be solved for as specified in Eq (C.3), which when substituted into Eq (C.2) results in the final expression for $f(x,y,z)$ as given by Eq (C.4). This equation completely describes the reference surface for given scan angles and specified gimbal point location.

$$\text{Given} \quad \vec{r}_g + \vec{D} \quad \text{satisfies} \quad f(x,y,z) = 0$$

$$f[Dk_x, Dk_y, z_g + Dk_z)] = D(k_x^2 + k_y^2 + k_z^2) + z_g k_z + C = 0 \qquad (C.3)$$

$$\rightarrow \quad C = -(D + z_g k_z)$$

$$f(x,y,z) = k_x x + k_y y + k_z(z - z_g) - D = 0 \qquad (C.4)$$

$$\text{Given} \quad \vec{r}_m + \vec{D}_m \quad \text{satisfies} \quad f(x,y,z) = 0$$

$$f[(x_m + D_m k_x), (y_m + D_m k_y), (z_m + D_m k_z)] = 0 \qquad (C.5)$$

$$\rightarrow \quad (x_m k_x + y_m k_y + z_m k_z) + D_m(k_x^2 + k_y^2 + k_z^2) - (D + z_g k_z) = 0$$

$$\rightarrow \quad (D_m - D) = -\{x_m k_x + y_m k_y + (z_m - z_g) k_z\}$$

For a pattern maximum to occur at given scan direction $\hat{k}$, responses from all elements within the array must coherently sum. Since a far-field assumption is made, all rays emanating from the UPW reference surface which are incident on the aperture elements are approximately parallel. Therefore, an arbitrary array element

182

may be chosen for developing the final expression for $\phi_w(m)$. Given arbitrary element location (x_m, y_m, z_m) as indicated in Figure C.1, the vector sum of $\vec{r}_m$ and $\vec{D}_m$ is constrained to lie on the reference surface and must satisfy Eq (C.4). Enforcing this constraint results in the final expression relating D_m and D as given by Eq (C.5). The difference between D_m and D corresponds to phase delay variances experience along the two propagation paths.

$$Given \quad \vec{E}_i = E_i \, e^{j\phi_i}$$

$$\vec{E}_o = E_i \, e^{j\phi_i} \, e^{j\phi_w(o)} \, e^{-jK_o D} = E_i \, e^{-j\{K_o D - \phi_i - \phi_w(o)\}} \qquad (C.6)$$

$$\vec{E}_m = E_i \, e^{j\phi_i} \, e^{j\phi_w(m)} \, e^{-jK_o D_m} = E_i \, e^{-j\{K_o D_m - \phi_i - \phi_w(m)\}}$$

$$For \quad Coherent \quad Summation$$

$$K_o D - \phi_i - \phi_w(o) = K_O D_m - \phi_i - \phi_w(m) \qquad (C.7)$$

$$\Rightarrow \quad \phi_w(m) = K_o(D_m - D) + \phi_w(o) = K_o(D_m - D)$$

Given the incident E-Field $\vec{E}_i$, expressions for the E-Fields incident at the gimbal point and element location may be expressed as given in Eq (C.6). Free-space propagation constant K_c is introduced to convert distance variations into appropriate radian phase variations. For coherent summation to occur, the final phase terms of the two incident E-Fields in Eq (C.6) must be equivalent. Eq (C.7) shows the result of equating the two phase terms. In simplifying the final expression, the phase reference for all aperture elements was arbitrarily chosen to be the aperture center

183

at $(0,0,z_g)$, eliminating $\phi_w(0)$ from the final expression. Results of Eq (C.5) and definitions established in Eq (C.1) are substituted into Eq (C.7) to arrive at the final phase weight expression given by Eq (C.8). Given arbitrary element locations and a desired scan direction, this expression is used to determine phase weights for all elements within the phased array aperture.

$$
\begin{aligned}
\phi_w(m) &= -K_o \left\{ x_m k_x + y_m k_y + \left(z_m - z_g \right) k_z \right\} \\
&= \frac{-2\pi}{\lambda_o} \left\{ \sin\theta_s \left(x_m \cos\phi_s + y_m \sin\phi_s \right) + \cos\theta_s \left(z_m - z_g \right) \right\}
\end{aligned}
\tag{C.8}
$$

Bibliography

1. Sherman, Samuel M., *Monopulse Principles and Techniques*. Massachusetts: Artech House, 1984.

2. Siwiak, K., T.B. Dowling and L.R. Lewis, "Boresight Errors Induced by Missile Radomes," IEEE Trans. Antennas Propagat., AP-27, Nov '79, pp. 832-841.

3. Huddleston, G.K., H.L. Bassett, and J.M. Newton "Parametric Investigation of Radome Analysis Results: Salient Results", Vol I of IV, Technical Report, AFOSR-77-3469, Bolling AFB, 1981.

4. Burks, D.G., E.R. Graf, and M.D. Fahey, "A High-Frequency Analysis of Radome-Induced Radar Pointing Error," IEEE Trans. Antennas Propagat., AP-30, Sep '82, pp 947-955.

5. Kozakoff, D.J. "Improved Radome Analysis Methodology", Conference Notes, MICOM Workshop on EM Windows and Domes, Redstone Arsenal, 1981.

6. Klemer, D.P. "Effects of Refraction by an Ogive Radome on Radome Boresight Error", Technical Report #675, Lincoln Laboratory, Massachusetts Institute of Technology, 1984.

7. Huddleston, G.K. and H.L. Bassett, "Radomes," in *Antenna Engineering Handbook*. R. Johnson and H. Jasik, Eds., New York: McGraw-Hill, 1984.

8. Balanis, C.A., *Advanced Engineering Electromagnetics*. New York: John Wiley & Sons, 1989.

9. Ruck, G.T., D.E. Barrick, W.D. Stuart, and C.K. Krichbaum, *Radar Cross Section Handbook, Volume 2*. New York: Plenum Press, 1970.

10. Richmond, J.H. "Efficient Recursive Solutions for Plane and Cylindrical Multilayers", Technical Report #1968-1, Contract #NOW 65-0329-d, The Ohio State University Research Foundation, 1968.

11. Henderson, L.W. "Introduction to PMM", Technical Report, WRDC-TR-89-9007, Wright-Patterson AFB, 1989.

12. McGrath, D.T., "Analysis of Radome Induced Cross Polarization". Technical Manual, WL-TM-92-700-XPN, Wright-Patterson AFB, 1992.

13. Stutzman, W.L., G.A Thiele, *Antenna Theory and Design*. New York: John Wiley & Sons, 1981.

14. Stark, L., "Microwave Theory of Phased-Array Antennas, A Review," Proc. of the IEEE, Vol. 62, Dec 1974.

15.　Balanis, C.A., *Antenna Theory: Analysis and Design*. New York: John Wiley & Sons, 1982.

16.　Leonov A.I. and K.I. Fomichev (Translated by William F. Barton), *Monopulse Radar*. Massachusetts: Artech House, 1986.

17.　Barton, D.K. and H.R. Ward "Handbook of Radar Measurement', New Jersey: Prentice Hall, Inc., 1969.

18.　Young, D.M. and R.T. Gregory, *A Survey of Numerical Mathematics*, Vol I of II, New York: Dover Publications, Inc.

19.　Gelfand, I.M. and S.V. Fomin, *Calculus of Variations*, New Jersey: Prentice-Hall, 1963.

20.　Munk, B.A., G.A. Burrell, and T.W. Kornbau, "General Theory of Periodic Surfaces in a Stratified Dielectric Medium," Technical Report, AFAL-TR-77-219, The Ohio State University, 1977.

21.　Tricoles, G., "Radiation Patterns and Boresight Error of a Microwave Antenna Enclosed in an Axially Symmetric Dielectric Shell," Journal Article, Optical Society of America, Vol. 54, No. 9, pp. 1094-1101, Sep. 1964.

22.　Tang, R. and R.W. Burns, "Phased Arrays," in *Antenna Engineering Handbook*, R. Johnson and H. Jasik, Eds., New York: McGraw-Hill, 1984.

23.　Hirsch, Herbert L. and Douglas C. Grove, *Practical Simulation of Radar Antennas and Radomes*. Massachusetts: Artech House, 1978.

24.　Moeschlin, L. and F. Ehrensvard, "Computer Analysis of Radome Influence on Antenna Radiation Patterns by Surface Integration Technique." Proc. of The Twelfth Symposium on Electromagnetic Windows, Jun '74, pp. 8-11.

25.　Orta, R., R. Tascone, and R. Zich, "Performance Degradation of Dielectric Radome Covered Antennas," IEEE Trans. Antennas Propagation, AP-36, Dec 1988, pp. 1707-1713.

26.　Rhodes, D.R., *Introduction to Monopulse*. New York: McGraw-Hill, 1959.

REPORT DOCUMENTATION PAGE

Public reporting burden for this collection of information is estimated to average 1 hour per response, including the time for reviewing instructions, searching existing data sources, gathering and maintaining the data needed, and completing and reviewing the collection of information. Send comments regarding this burden estimate or any other aspect of this collection of information, including suggestions for reducing this burden, to Washington Headquarters Services, Directorate for Information Operations and Reports, 1215 Jefferson Davis Highway, Suite 1204, Arlington, VA 22202-4302, and to the Office of Management and Budget, Paperwork Reduction Project (0704-0188), Washington, DC 20503.

1 AGENCY USE ONLY (Leave blank)	2 REPORT DATE	3 REPORT TYPE AND DATES COVERED
	June 93	Dissertation

4 TITLE AND SUBTITLE	5 FUNDING NUMBERS
RADOME DEPOLARIZATION EFFECTS ON MONOPULSE RECEIVER TRACKING PERFORMANCE	

6 AUTHOR(S)

Michael A. Temple, Capt, USAF

7 PERFORMING ORGANIZATION NAME(S) AND ADDRESS(ES)	8 PERFORMING ORGANIZATION REPORT NUMBER
Air Force Institute of Technology, WPAFB, OH 45433-6583	AFIT/DS/ENG/93-03

9 SPONSORING/MONITORING AGENCY NAME(S) AND ADDRESS(ES)	10 SPONSORING/MONITORING AGENCY REPORT NUMBER
David A. Hime Wright Laboratory, AAWD WPAFB, OH 45433-6534	

11. SUPPLEMENTARY NOTES

12a DISTRIBUTION/AVAILABILITY STATEMENT	12b DISTRIBUTION CODE
Approved for public release; distribution unlimited	

13. ABSTRACT (Maximum 200 words)

Boresight Error (BSE), defined as the angular deviation between the true position and the apparent position of a target as indicated by a radar, is an important figure of merit for a tracking radar. A significant contributor to system BSE is the protective radome. This research effort employed a GO technique to investigate the effects of a radome on BSE, expanding previous ray-trace receive techniques to include: 1) a uniquely defined/developed mathematical description for each surface within arbitrary multi-layer tapered radomes, 2) an "ideal" taper function concept for obtaining optimum BSE prediction performance, 3) a generalized technique for calculating specular reflection points within the radome, and 4) the total refractive effects along ray propagation paths. Computer model results were compared with limiting case data (BSE = 0°), published experimental data, and production system acceptance test data. For all limiting cases, "system" modeling error was less than .06 mRad. "Excellent" (BSE within ±1 mRad) results were obtained using a hemispheric radome with a displaced aperture gimbal point, predicted BSE values were within ±1 mRad of published experimental data. Likewise, BSE predictions for the production system were within ±0.5 mRad of measured data over a 30° scan range. Ray refractive effects on BSE prediction were characterized using the validated model.

14 SUBJECT TERMS	15 NUMBER OF PAGES
Radome Depolarization, Boresight Error Prediction, Monopulse Radar, Radome Modeling, Multi-Layer Radomes, Tapered Radomes	198
	16 PRICE CODE

17. SECURITY CLASSIFICATION OF REPORT	18 SECURITY CLASSIFICATION OF THIS PAGE	19 SECURITY CLASSIFICATION OF ABSTRACT	20 LIMITATION OF ABSTRACT
UNCLASSIFIED	UNCLASSIFIED	UNCLASSIFIED	UL